Study of the microstructure and texture evolution during extrusion and their effect on the mechanical properties of Mg-Zn based alloys modified with Ca or Nd

vorgelegt von
Guadalupe Cano-Castillo, MSc

von der Fakultät III – Prozesswissenschaften
der Technischen Universität Berlin
zur Erlangung des akademischen Grades

Doktor der Ingenieurwissenschaften
- Dr.-Ing. –

genehmigte Dissertation

Promotionsauschuss:

Vorsitzender: PD Dr. Sören Müller

Gutachterin: Prof. Dr.-Ing. Claudia Fleck

Gutachter: Prof. Dr.-Ing. Karl Ulrich Kainer

Tag der wissenschaftlichen Aussprache: 5. Januar 2022

Berlin, 2022

Abstract

Magnesium based alloys are attractive materials to be used in the fabrication of structural and non-structural components of automobiles and casings for electronics. They are also becoming increasingly attractive for the aerospace industry. This is due to their combined low density with excellent specific properties. However, wrought magnesium alloys must be improved due to their often-strong crystallographic textures during processing which can result in low mechanical properties. This is mainly caused by the hexagonal closed packed crystal (HCP) structure and the lack of sufficient independent slip systems. The improvement of the mechanical properties can be achieved by the activation of different deformation modes, for this reason, special attention must be given to the understanding of their activity.
The present work has been carried out to study the extrusion processing of the Mg-Zn, Mg-Zn-Ca and Mg-Zn-Nd alloys. A focus was given to the influence of the Neodymium (Nd) and Calcium (Ca) additions on the microstructural evolution, texture development and recrystallization behavior of the Mg-Zn based alloy. In that regard, the crystallographic texture formed in the wrought Mg alloys depends on the active deformation mechanisms during the thermomechanical processing but also during recrystallization. Mostly, two different recrystallization processes influence the microstructure and crystallographic texture, i.e. dynamic (DRX) and static recrystallization (SRX). DRX process takes place during the thermomechanical processing while SRX after processing. Both recrystallization processes were investigated in this work. Furthermore, a detailed analysis on deformation mechanisms has been carried out by applying a crystal plasticity model, i.e. the viscoplastic self-consistent (VPSC) model and by following the slip trace methodology combined with electron backscatter diffraction (EBSD) measurements in deformed tensile/compression samples.

During processing, the binary Mg-Zn alloy showed a homogenous, coarse and completely recrystallized microstructure, whereas the ternary Ca containing alloy also exhibited a completely recrystallized but finer microstructure. Contrarily, the ternary Nd containing alloy displayed a partly recrystallized microstructure at some extrusion conditions. At the completion of the recrystallization process, a fine microstructure was formed which was finer than that observed in the Ca containing alloy. This result indicates that the Ca and Nd additions not only induce a delay in the DRX process but also in grain coarsening. In addition, the Mg-Zn alloy exhibited in general a basal crystallographic texture $< 11\bar{2}0 >$-$< 10\bar{1}0 >$, whereas in the Ca containing alloy the main texture component is the $< 10\bar{1}1 >$ pole. Finally, in the Nd containing alloy, the $< 11\bar{2}1 >$ pole dominates the texture. In contrast, if partly recrystallized microstructures are annealed, it was found that this distinctive behavior could be changed. The non-basal texture observed after the DRX process evolved to a basal texture after the SRX process. This leads to an increase of the importance of SRX and a different resulting texture while maintaining a similar grain structure.

Uni-axial tensile and compression tests of the extruded alloys showed that the addition of Nd and Ca results in a significant increase ductility at room temperature. Additionally, there is a remarkable reduction of the tension-compression yield asymmetry. These properties are due to non-basal crystallographic textures and the activity of non-basal deformation modes.
The VPSC simulations demonstrated that basal <a> slip and prismatic <a> dominate the tension deformation of the Mg-Zn alloy, whereas extension twining and basal <a> slip control the deformation in compression. In Mg-Zn-Ca and Mg-Zn-Nd alloys, additionally to basal <a> and prismatic <a> modes, evidence of pyramidal <a> was observed in tension. Although basal <a> slip and extension twinning accommodated the deformation in compression, pyramidal <a>, pyramidal I <c+a> and pyramidal II <c+a> played an important role during the deformation. The deformation modes activity observed during the slip trace analysis is comparable with the obtained during the VPSC simulations.

Kurzfassung

Magnesiumlegierungen sind attraktive Werkstoffe für die Herstellung von nicht-strukturellen Automobilbauteilen und Gehäusen für Elektronik. Auch für die Luft- und Raumfahrtindustrie werden sie immer interessanter. Dies liegt an der Kombination aus geringer Dichte und hervorragenden spezifischen Eigenschaften. Knetlegierungen aus Magnesium müssen jedoch verbessert werden, da sie bei der Herstellung oft starke kristallografische Texturen aufweisen, die zu schlechten mechanischen Eigenschaften führen können. Dies ist vor allem auf die hexagonale Kristallstruktur (HCP) und das Fehlen von ausreichend unabhängigen Gleitsystemen zurückzuführen. Die Verbesserung der mechanischen Eigenschaften kann durch die Aktivierung verschiedener Verformungsmechanismen erreicht werden, deshalb muss dem Verständnis ihrer Aktivität besondere Aufmerksamkeit geschenkt werden.

Die vorliegende Arbeit wurde durchgeführt, um die Strangpressbarkeit der Legierungen Mg-Zn, Mg-Zn-Ca und Mg-Zn-Nd zu untersuchen. Ein Schwerpunkt wurde auf den Einfluss von Neodym- (Nd) und Calcium- (Ca) auf die mikrostrukturelle Entwicklung, die Texturentwicklung und dass Rekristallisationsverhalten der Mg-Zn-Basislegierung gesetzt. Dabei hängt die kristallographische Textur, die sich in den Mg-Knetlegierungen ausbildet, von den aktiven Verformungsmechanismen während der thermomechanischen Verarbeitung, aber auch während der Rekristallisation ab. Meistens beeinflussen zwei verschiedene Rekristallisationsprozesse das Mikrostruktur und die kristallographische Textur, nämlich die dynamische (DRX) und die statische Rekristallisation (SRX). Der DRX-Prozess findet während der thermomechanischen Verarbeitung statt, während SRX nach dem Prozess erfolgt. Beide Rekristallisationsprozesse wurden in dieser Arbeit untersucht. Darüber hinaus wurde eine detaillierte Analyse der Verformungsmechanismen durch Anwendung eines Kristallplastizitätsmodells, d. h. des viscoplastic self-consistent (VPSC) model, und durch die Anwendung der slip trace Methode in Kombination mit electron backscatter diffraction (EBSD) Messungen an verformten Zug-/Druckproben durchgeführt.

Während der Verarbeitung zeigte die Mg-Zn-Legierung ein homogenes, grobes und vollständig rekristallisiertes Mikrostruktur, während die Ca-haltige Legierung ebenfalls ein vollständig rekristallisiertes, aber feineres Mikrostruktur aufwies. Im Gegensatz dazu zeigte die Nd-haltige Legierung bei einigen Strangpressbedingungen ein teilweise rekristallisierte Mikrostruktur. Nach Abschluss des Rekristallisationsprozesses bildete sich ein feinkörniges Gefüge, das feiner war als dass in der Ca-haltigen Legierung beobachtete. Dieses Ergebnis zeigt, dass die Ca- und Nd-Zusätze nicht nur eine Verzögerung des DRX-Prozesses, sondern auch der Kornvergröberung bewirken. Darüber hinaus wies die Mg-Zn-Legierung im Allgemeinen eine basale kristallographische Textur $< 11\bar{2}0 >-< 10\bar{1}0 >$ auf, während in der Ca-haltigen Legierung die Haupttexturkomponente der $< 10\bar{1}1 >$ Pole ist. In der Nd-haltigen Legierung dominiert der $< 11\bar{2}1 >$ Pole die Textur. Werden dagegen teilweise rekristallisierte Mikrostruktur geglüht, so konnte dieses ausgeprägte Texturverhalten verändert werden. Die nach dem DRX-Prozess beobachtete nicht-basale Textur entwickelte sich nach dem SRX-Prozess zu einer basalen Textur. Dies führt zu einer Erhöhung der Bedeutung von SRX und einer anderen resultierenden Textur bei gleichbleibender Kornstruktur.

Einachsige Zug- und Druckversuche an den stranggepressten Legierungen zeigten, dass die Zugabe von Nd und Ca zu einer signifikanten Erhöhung der Duktilität bei Raumtemperatur führt. Zusätzlich kommt es zu einer bemerkenswerten Verringerung der Zug-Druck-Asymmetrie. Diese Eigenschaften sind auf nicht-basale kristallographische Texturen und die Aktivität nicht-basaler Verformungsmechanismen zurückzuführen.

Die VPSC-Simulationen zeigten, dass basales <a> Gleiten und prismatisches <a> die Verformung im Zugversuch der Mg-Zn-Legierung dominieren, während Dehnungszwillinge und basales <a> Gleiten die Verformung im Druckversuch kontrollieren. In Mg-Zn-Ca- und Mg-Zn-Nd-Legierungen wurden zusätzlich zu den basalen <a>- und prismatischen <a>-Modi Anzeichen von pyramidalem <a> in der Spannung beobachtet. Obwohl basales <a> Gleiten und Zugzwillinge die Verformung in der Kompression aufnahmen, spielten pyramidales <a>, pyramidales I <c+a> und pyramidales II <c+a> eine wichtige Rolle während der Verformung. Die Aktivität der Verformungsmoden, die während der Analyse der Gleitspuren beobachtet wurde, ist vergleichbar mit den Ergebnissen der VPSC-Simulationen.

Acknowledgements

The present thesis was written during my work as a PhD student at the Helmholtz-Zentrum Hereon. I would like to take this opportunity to thank all those who supported me and contributed to the success of this work.

In first place, I would like to thank to my academic supervisor Prof. Dr.-Ing. Karl Ulrich Kainer and to my group leader Dr. Dietmar Letzig, who have given me the opportunity to do this work and have always encouraged and supported me in its completion. I am also grateful to Prof. Dr.-Ing. Claudia Fleck for giving me the opportunity to carry out my doctoral research under her supervision at the Technical University of Berlin.

My deep gratitude to Dr. Jose Victoria-Hernandez who supported, advised, and motivated me tirelessly in all situations and had the time and pleasure in correcting this work. I would like to thank to Dr. Jan Bohlen for the interesting discussions as well as suggestions and motivating guidance since the start of this work. I would like to thank Dr. Gerrit Kurz and Dr. Sangbong Yi for their help with lab facilities as well as experiments.

I value the colleagues help with whom I have been working during my stay at Helmholtz-Zentrum Hereon: Dr. Sumi Jo, Dr. Sangkyu Woo, Dr. Rosario Silva, Mr. Xun Zeng, Mrs. Maria Nienaber and Mr. Changwan Ha. Thank all of you for such a nice and friendly atmosphere during working.

I would like to thank to Mrs. Petra Fischer, Mrs. Yukyung Shin and Mr. Gerd Wiese for their support in the metallographic preparation and microscope observation. I want to thank to Mr. Günter Meister for assisting me in the foundry, Mr. Alexander Reichert and Mr. Stefan Koch for helping me in the sample preparation for mechanical testing.

I want to thank the financial support from the Mexican Council of Science and Technology (CONACyT) and the German Academic Exchange Service (DAAD) who providing me the opportunity to do this project.

I am deeply and forever indebted to my family, my mother Felipa Castillo, my brothers and sisters, thank you very much for your love throughout my life. I want to thank to my friend Maria Teresa Rojas Sánchez for encouraging me to continue with my professional preparation. Thanks to my friends, Alan Quispe and Melina Ortega for making me feel like part of their family. I also want to thank to Daniel Tamara, Sara Huamanzana, Martha Vinueza, Alex Almeida, Mario Gomez, Zully Flores, Ana Bayas, Edelina Gentile, Kathia Gerdts and Urban Röpke for their friendship and invaluable advices.

Table of Contents

1. Introduction

Nowadays, the use of light materials for diverse applications has become inevitable in the world. The growing demand for improved fuel economy has created a huge attention in lightweight materials to create new structures for the transportation industry [1]. This can be achieved through the development of innovative strategies directed to saving weight by using lightweight materials e.g. magnesium. Magnesium and its alloys have the potential to be used for diverse components in automotive and aerospace industries owing to its low density (1.74 g/cm), high specific strength and stiffness. Furthermore, the use of magnesium for manufacturing diverse devices applicable to biomedical industry is also possible; this is due to the excellent biocompatibility with the human body.

Differently from the magnesium castings alloys, which are more commonly used, the wrought magnesium alloys still are not often used for industrial applications [2]. To take advantage of the full weight saving capacity of parts made of magnesium, wrought alloys are required, because they usually exhibit better mechanical properties such as higher strength and ductility in comparison with cast alloys. Conventional thermomechanical processes such as extrusion and rolling as well as non-conventional processes like equal channel angular extrusion (ECAE) and friction stir processing (FSP) are quite important to alter the grain size, crystallographic texture and the distribution of secondary phases [3]. Despite such microstructure modifications, issues such as low strength and high anisotropy still limit the extensive use of the wrought Mg alloys. This is due to the strong crystallographic textures formed during processing where the basal planes of the hexagonal close packed (HCP) structure of magnesium align parallel to the deformation direction. The use of different alloying elements combined with thermomechanical treatments have been applied to overcome the limitations mentioned previously.

It is well accepted that the mechanical properties of Mg alloys are impacted by the microstructural evolution and the crystallographic texture development [4]. The crystallographic texture promotes or hinders the activation of individual deformation modes due to the changing of critical resolved shear stress (CRSS) or Schmid factor (SF). To alter the grain size and tailor the crystallographic texture, the extrusion process is one of the most commonly applied thermomechanical processes. Processing conditions such as extrusion ratio, temperature and speed can influence the recrystallization behavior and the development of microstructure and therefore have a strong effect, first on the crystallographic texture and finally, modifying the mechanical response of the extruded materials.

Consequently, a profound understanding of the relationship between the processing parameters and the resulting microstructure as well as between the microstructural development and the resultant mechanical properties is required. Therefore, the present work analyzes the effect of the extrusion temperature and speed and of post-extrusion heat treatments of Mg-Zn based alloys modified with single additions of Ca and Nd. This enables the analysis and the comparison of the effects of the Ca and Nd on the microstructure and crystallographic texture development of the extruded Mg-Zn based alloys.

As a processed magnesium product, the microstructure and crystallographic texture developed during the processing has a great impact on several features of the mechanical properties such as yield stress on tension or compression (TYS or CYS), ultimate stress on tension or compression (UTS or UCS) and fracture strain. From a general point of view, the crystallographic texture and microstructure affect the plastic flow of the extruded products. It is well known that the plastic behavior is susceptible to different deformation mechanisms.

Even though the relationship between plastic behavior and different deformation mechanisms is known, the general relationship remains largely unclear. Hence, this research work seeks to determine the effect of recrystallization evolution during extrusion and its impact on the microstructure and crystallographic texture development of Mg-Zn based alloys with separate additions of Ca and the rare earth Nd. An emphasis to the development of different crystallographic textures based on the dynamic recrystallization (DRX) and grain growth due to the modification of extrusion conditions is given. Furthermore, the effect of static recrystallization (SRX) on the grain growth to modify the crystallographic texture by using partially dynamic recrystallized microstructures is also investigated.
Finally, the mechanical properties of the extruded materials are correlated with the resultant microstructure and crystallographic texture during the extrusion processing. A detailed analysis of the possible deformation mechanisms dominating the plastic behavior of the extruded magnesium alloys due to the different microstructure is carried out.

1.1 Objectives

The present work aims to provide a comprehensive analysis of the relationship between single additions of Ca and Nd and extrusion parameters on the microstructure evolution of extruded Mg-Zn based alloys. This work also aims to elucidate the role of the initial microstructure and texture on the activity of possible deformation mechanisms and the correlated mechanical properties of the extruded alloys.

1.1.1 Specific objectives

- Assessing the extrusion process parameters for each extruded alloy.
    - The extrusion process is analyzed in terms of the alloy composition as well as the final surface quality of the extruded bars. Also analyzed is the effect of Ca or Nd on the microstructure and crystallographic texture evolution of Mg-Zn based alloys. Adding Ca or Nd combined with the extrusion parameters will alter differently the microstructure and crystallographic texture of the Mg-Zn based alloy.

- Studying the microstructure and crystallographic texture evolution of each alloy due to the recrystallization process.
    - The crystallographic texture evolution is analyzed in terms of different fractions of deformed and dynamically recrystallized grains. Furthermore, the importance of static recrystallization (SRX) on the crystallographic texture modification is also studied. The analysis of grain growth with specific orientations, following DRX or SRX nucleation, is essential for understanding the recrystallization texture evolution.

- Correlating the resultant microstructure and crystallographic texture with the mechanical properties of the extruded alloys.
    - The importance of the initial microstructure and texture on the mechanical behavior and the activation of the possible deformation modes during the plastic behavior of extruded bars is analyzed by coupling experimental work, e.g. slip trace analysis with crystal plasticity simulations using the viscoplastic self-consistent (VPSC) model. This to provide a sound understanding of the possible activation of additional non-basal slip systems according not only to chemical composition, but to also initial crystallographic texture.

2. Background

2.1 Magnesium

Magnesium (Mg) is the lightest engineering metal with a lower density than aluminum and steel, i.e., 1.74 g/cm^3, 2.7 g/cm^3 and 7.8 g/cm^3, respectively. Useful characteristics of Mg include its high stiffness, which is higher than for example Al, Fe, and plastics, i.e., 2.0 GPa$^{1/3}$/ (Mg/m^3), 1.5 GPa$^{1/3}$/ (Mg/m^3), 0.75 GPa$^{1/3}$/ (Mg/m^3), 1.1-1.5 GPa$^{1/3}$/ (Mg/m^3), respectively [5, 6]. In addition, its Young's modulus is about 45 GPa at room temperature, it has a specific heat of roughly 1.05 kJ/kg°C and a low melting temperature (~650°C) [7].

Magnesium as well as its alloys are readily produced following the near-net shape casting process. Already in 1909, an Mg crankcase was presented at the International Air Transport Fair in Frankfurt and in 1924, Mg alloys were used in the automobile industry for the first time to produce pistons by die casting [8].

Even though the Mg alloys have been used in the industry since the early 20th century, the spread of their applications remain limited, predominantly due to the cost-effective commercial Mg alloys do not have the adequate properties such as yield strength (YS), ductility, formability and corrosion resistance [9, 10]. In recent years, the renewed interest in Mg and its alloys has been motivated due to the requirement of weight-saving in the automotive, aerospace and portable electronics industries.

In the transport industry, the magnesium alloys are considered as a material important to achieve lightweight and therefore in the improvement of the energy efficiency and the greenhouse gas reduction on the world. Notwithstanding the emerging importance of magnesium alloys as a class of engineering material, up to now the magnesium alloys have had a minimal usage in the industry, the same can also be said for the extruded alloys.
The extruded magnesium products represent less than 1.5 % of the annual production of magnesium in 2004 and remained at less than 3% in 2013 [1, 3]. In contrast, roughly 25% of the Al alloy products are produced by extrusion and have been adopted in different applications [11]. Three major issues have restricted the wider use of magnesium alloy extrusions.

The first issue corresponds to the properties of the extruded profiles, in that regard, the Mg extrusions has lower strength than the Al extrusions, limited formability as well as a high tension-compression yield asymmetry. The next issue is the commercial viability, being some of the Mg alloys more expensive, which depends on the alloying elements. In addition, only few magnesium alloys are capable of being extruded at high enough speeds to be viable. The last issue is related with the poor corrosion resistance of the magnesium extrusion alloys. In general, the corrosion rate of magnesium alloys is dominantly given by the electrochemical potential and secondly by the alloy chemistry, it is determined by the specific elements with which the magnesium is alloyed [12].
Nevertheless, the corrosion topic is beyond the scope of this work. Therefore, it is covered the effect of the extrusion processing parameters on the subsequent microstructure development as well as the mechanical performance of magnesium alloys.

Through the last years, improvements on the magnesium alloys have been done. These improvements have been reported on the extrudability and the mechanical properties of magnesium alloys. With respect to the extrudability, the most investigated has been principally the extrusion speed. It has been reported that the maximum extrusion speed of some dilute Mg alloys can be as high as that of Al extrusion alloys [13]. In terms of the mechanical performance, the tensile yield strength of the extruded magnesium alloys has shown an

increment from less than 300 MPa to a yield strength of over 400 MPa for rare earth element free alloys, for instance, the Mg-Al-Ca-Mn alloy [14] and roughly 500 MPa for a Mg-Gd-Y-Zn-Zr alloy reported by N. Kunito et al [15]. The ductility has also been improved, from less than 20% to bigger than 40% [16].

The improvements are all of them correlated with the microstructure development due to the combination of processing and alloy design. To date, different alloying elements have been used to produce different magnesium alloys. Each alloying element has a specific effect on magnesium. In the next section is described the effect of some alloying elements used to alloy it.

2.2 Influence of alloying additions on Magnesium

An effective way to improve the properties of magnesium is by using alloying elements. The presence of alloying elements improves the properties of magnesium, this is due to the grain size refining as well as the formation of intermetallic particles. Significant advances have been achieved in the alloy development using alloying elements such as Aluminum (Al), Zinc (Zn), Manganese (Mn), Zirconium (Zr), Calcium (Ca) or rare earths (RE). In this section is described the effect of some alloying elements on magnesium.

2.2.1 Aluminium

Aluminium (Al) has a large solubility in magnesium, which is about 12.9 wt.% at the eutectic temperature of 437 °C, and it decreases to about 3.6 wt.% at 200 °C [17]. It is the most used alloying element in magnesium. Most of the commercial extruded alloys are based on the Mg-Al alloy system. Some of these alloys are AZ31, AZ61 and AZ80. The addition of certain amount of Al can increase not only strength but also ductility. The low density of Al is an advantage when it is added to magnesium, such advantage does not compromise the density of the alloy when Al is added in large additions [12]. The formation of the intermetallic phase $Mg_{17}Al_{12}$ contribute to increasing the tensile strength.

2.2.2 Zinc

Zinc (Zn) is one of the most frequently used alloying elements in magnesium. Its maximum solubility in magnesium is 6.2 wt.% [17]. Combined with aluminum, Zn is often used to produce improvements in the strength at room temperature [18]. Zn can improve the mechanical properties by solid solution hardening and age hardening. Nevertheless, with amounts higher than 1 wt.% leads a precipitation sequence which is associated with hardness decrease [19, 20]. When Zn is added in quantities bigger than 1 wt.% to magnesium alloys containing aluminum from 7 to 10 wt. %, the hot-shortness increases [18]. In terms of cast-ability, Zinc produces a similar effect as Al. Besides, Zinc is an important alloying element that contributes to the grain refinement [21, 22]. Such a grain refinement can be related with the increase of strength because of Hall-Petch effect [23, 24]**.**

2.2.3 Manganese

Manganese (Mn) as alloying element helps to increase the strength of magnesium alloys but also improves their corrosion resistance by reducing the harmful effects of Fe [25]. This alloying element has a solubility limit of 2.2 wt.% on magnesium at high temperature [26]. At lower temperatures, the precipitation of α-Mn is expected [27]. It is usually added in combination with Al. Mn as alloying element helps to refine the microstructure or forming

special structures. When Mn is added to magnesium alloys, such alloying element tend to form weak textures after extrusion [4].

2.2.4 Calcium

Calcium (Ca) as alloying element has a maximum solubility of 1.35 wt.% in Magnesium [17]. It also works as a grain refiner when is added to Mg. Thermally stable intermetallic compounds, such as the Mg_2Ca would precipitate along grain boundaries of α-Magnesium matrix during solidification [28]. A size misfit in the magnesium lattice structure or a decrease of the stacking fault energies are some of the features, which change the balance of deformation mechanisms in alloys modified by Ca [29, 30]. Therefore, Calcium also modifies the texture during processing. The addition of this alloying element, for example to Mg-Zn based alloys leads to the development of some characteristic texture components also resulting in a certain tilt of basal planes out of the extrusion direction [16, 31, 32]. The changes in the grain structure and texture lead to an increase of the ductile behavior at room temperature.

2.2.5 Neodymium

Recent investigations pointed out the role of rare earths (RE) elements on Magnesium [4, 33, 34]. The RE alloying elements can be divided into two groups with large and limited solubility in Mg. In the specific case of Neodymium (Nd), this alloying element belongs to the group with a low solubility in Magnesium, roughly 0.59 wt.% [35]. Different authors have found that still this element leads to reduce the grain size and weakening the texture even in low quantities into Magnesium [36-38]. The retardation of the recrystallization process and the formation of specific texture components after thermomechanical treatments are the effect of the addition of rare earth elements to magnesium [39]. The particular feature associated with the texture weakening are some special texture components named as ‘‘RE-textures. A common example of RE textures are the <11-21> formed during extrusion where the basal planes are tilted out of the extrusion direction [40]. The formation of that kind of texture contributes with an enhancement of ductility and the reduction of the asymmetry of mechanical properties at room temperature [37, 39].

2.2.6 Cerium

Cerium (Ce) belongs to the rare earths allying elements commonly used in magnesium. This rare earth element has a solubility of 0.74 wt.% in magnesium [26]. It is one of the strongest potential texture modifiers for the wrought magnesium alloys [41]. Ce weakens the deformation and annealing texture at concentrations as small as 0.057 wt.%, however this effect is quickly leveled at concentrations above 0.17 wt.% [39]. Magnesium alloys containing Ce develop relative softer texture away from the basal texture. It has been suggested in [42] that the superior efficiency of Ce has to do with its low solubility limit in comparison with other RE elements.

2.2.7 Zirconium

Zirconium (Zr) is added to magnesium as a potent grain refiner to improve the mechanical properties. The maximum solubility of Zr in magnesium is 3.8 wt.% [26]. This alloying element helps to enhance the extrudability of magnesium alloys, furthermore its addition leads to a much denser distribution of precipitates [12]. The Zr addition also includes the corrosion resistance improvement of the magnesium alloys [43].

From the previously described alloying elements, the relevant alloying elements for this study are Zn, Ca and the rare earth Nd.

2.3 Deformation mechanisms in magnesium

The crystal structure of magnesium corresponds to HCP, which is schematically shown in Figure 2.1. In the HCP lattice, the planes and directions are described by using the Miller-Bravais indices which relates to a coordinate system of three basal vectors (a_i) and a longitudinal axis called *c*-axis [44]. The hexagonal unit cell has axes $a_1=a_2=a_3 \neq c$, and angles $\alpha=\beta=90°$, $\gamma=120°$. In case of magnesium, the c/a ratio is 1.623, which is quite close to the lattice parameters (c/a) for the ideal packing arrangement in the HCP unit cell, 1.633.
In contrast to FCC and BCC materials, the HCP structure has limited slip systems. At room temperature, the deformation of Mg and its alloys is made by slip, which means that the dislocations glide takes place along different crystallographic planes known as slip planes. The basal, prismatic and pyramidal are the principal slip systems on magnesium. Besides, twining is other possible deformation mechanism that can be activated at room temperature.

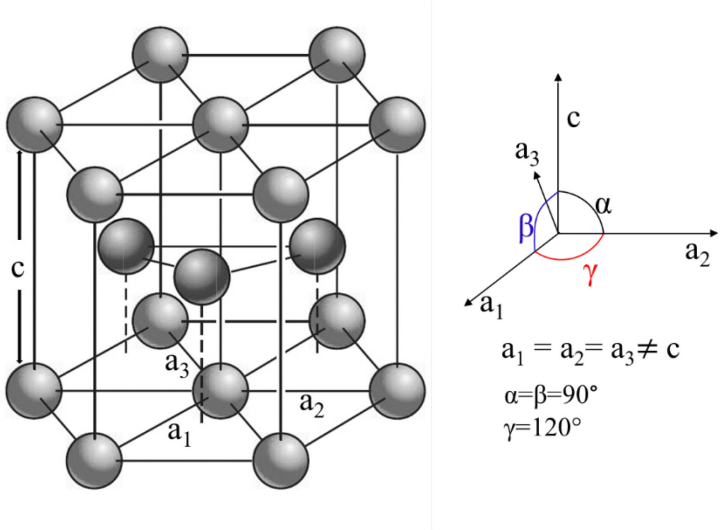

Figure 2.1. The hexagonal unit cell [45].

2.3.1 Slip systems

A slip plane together with the slip direction defines a slip system. The crystallographic slip normally occurs due to the sliding of a particular crystallographic plane over a neighbor plane in a specific crystallographic direction. Slip begins when the shearing stress reaches a threshold value called as the *critical resolved shear stress* (CRSS), which for uniaxial loading, the CRSS is calculated as follow in equation 1 [46] and schematically shown in figure 2.2.

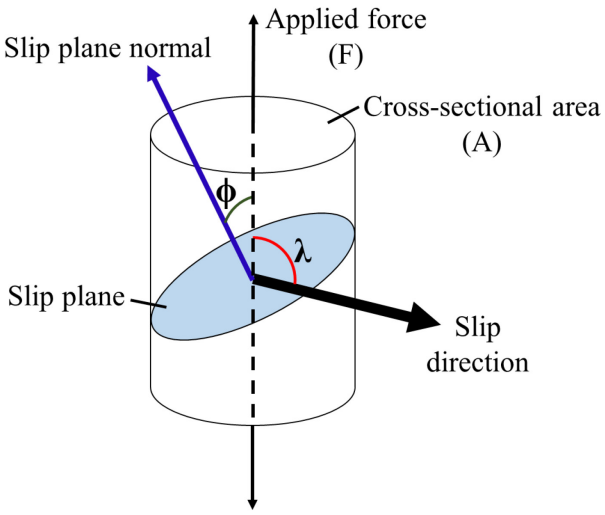

Figure 2.2. Schematic representation of the resolved shear stress determination [46].

$$\tau_R = \frac{P\cos\lambda}{A/\cos\phi} = \frac{P}{A}\cos\phi\cos\lambda \qquad \text{(Eq. 1)}$$

Where:

A is the cross-sectional area, ϕ corresponds to the angle between the normal to the slip plane and the tensile axis, λ is the angle between the slip direction and the stress axis, $A/\cos\phi$ corresponds to the area of the slip plane inclined at the angle ϕ and $P\cos\lambda$ is the component of the axial load acting in the slip plane in the slip direction.
Then, the deformation is influenced by the anisotropy that results from the low symmetry of the HCP structure. According to Von Mises criterion, a material requires five independent slip systems to deform in an arbitrary way [47]. The low symmetry of the HCP structure of magnesium strongly influences the deformation. Such a low symmetry restricts the availability of slip modes, which can be activated simultaneously. In magnesium, the possible slip modes are schematically illustrated in Figure 2.3. Each slip mode has a number of systems that can operate during deformation. It is generally accepted that basal slip is the softest mechanism; and the activation of the other slip modes normally depends on the temperature and the stress level [48]. For magnesium and its alloys, the principal slip mode is the basal slip [49]. However, the basal slip provides only three independent slip systems [8], therefore it becomes necessary the activation of the non-basal slip modes [8, 50]. Nevertheless, the activation of the non-basal slips is hard, in that case, the high temperature and the high stresses are the responsible for the activation of such slip modes [51].

In figure 2.4, the effect of temperature on the CRSS of different slip systems of the magnesium single crystal is illustrated. A transition occurs after 230 °C when the values of CRSS of prismatic and pyramidal slip decrease considerably.

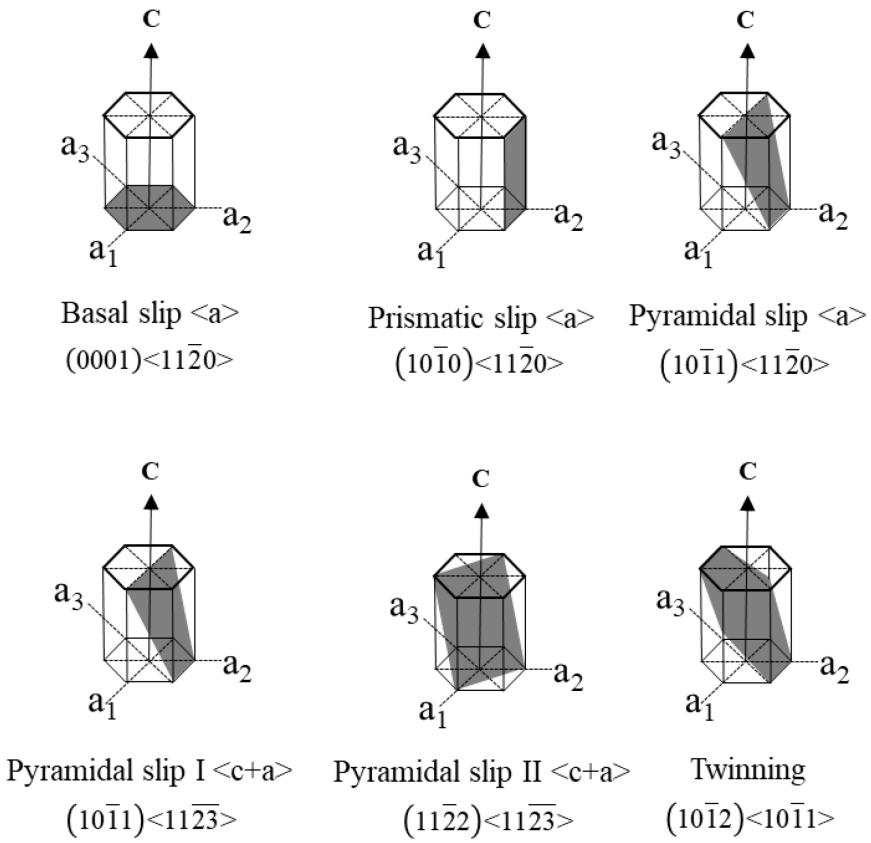

Figure 2.3. Slip systems in magnesium [52].

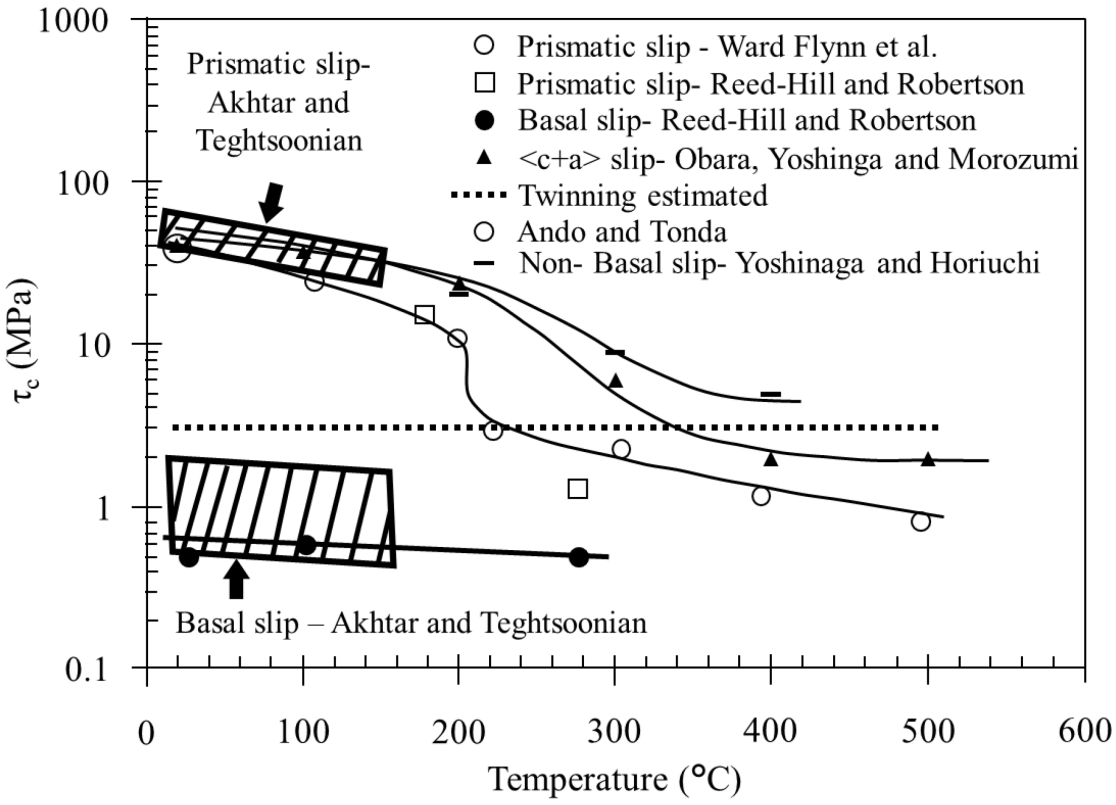

Figure 2.4. Effect of temperature on the CRSS of slip systems and twinning in pure Mg [53].

The use of alloying elements may also affect the balance of slip systems through different ways, for example by altering the *c/a* ratio and changing the CRSS of the slip systems, changing the crystal structure of magnesium, modifying the stacking fault energy (SFE) and changing the grain size [12, 39].

2.3.2 Deformation by twinning

The other important mechanism by which is possible to deform a metal is the process known as twinning. The twinning results when a portion of the crystal takes up an orientation that is related to the orientation of the rest of the untwined lattice in a definite, symmetrical way. The twined portion of the crystal is a mirror image of the parent crystal. The plane of symmetry between the two portions is called the twinning plane [46]. Figure 2.5 illustrates a schematic representation of twinning. Twinning takes place when the slip systems are restricted, then, the occurrence of twining at low temperatures or high strain rates in hcp metals is due to the unfavorable orientation for basal slip [54]. The importance of twinning in plastic deformation does not come from the strain produced by the twinning process but from the fact that orientation changes resulting from twinning may place new slip systems in a favorable orientation with respect to the stress axis so that additional slip can take place [46].

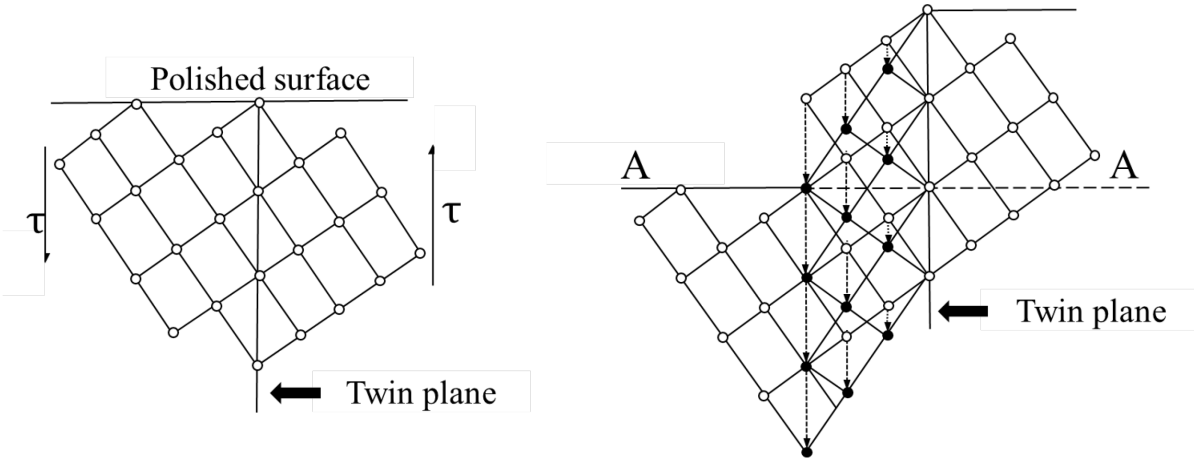

Figure 2.5. Schematic presentation of how twinning results from shear stress τ [46].

Contrasting to slip, due to the polar nature of twinning, the shear can take place only in one direction. According to the amount of twinning shear as a function of the *c/a* ratio, the twinning modes may be either tensile or compressive [55]. A twin mode showing a positive slope in Figure 2.6 results in contraction along the *c*-axis meanwhile a twin mode showing a negative slope results in extension along *c*-axis.
In magnesium alloys, three types of twins have been reported: tensile twins, compressive twins and double twins. Extension alongside the *c*-axis favors {10-12} twinning whereas a compression along this axis favors {10-11} <10-12> twinning [56]. Therefore, the most common twinning mode in magnesium, i.e. {10-12} twinning is recognized as tension or extension twin since it provides extension along the c-axis [57, 58]. Thus, the {10-11} twining is known as compression or contraction twin.

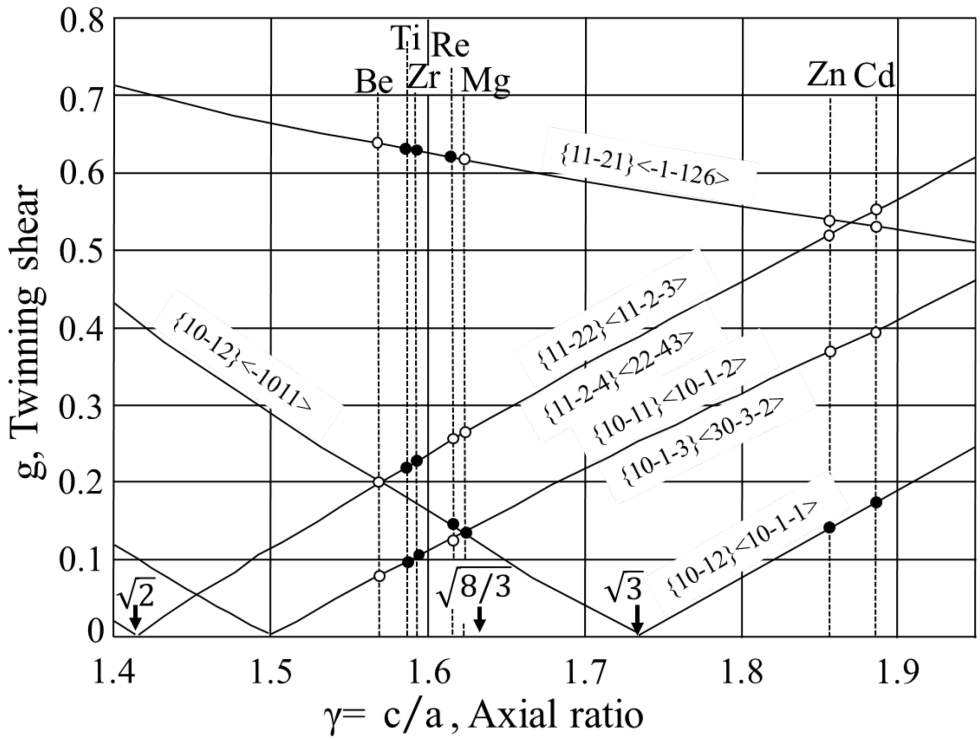

Figure 2.6. Variation of twinning shear with the c/a ratio for various twinning modes in HCP metals [55].

Twinning can alter the orientation of the original grains and is accepted that reorients the basal planes. The reorientation by 86 ° is associated to the tensile twinning, the reorientation by 56 ° is related to compression twinning while the double twinning is correlated with a reorientation by 38°. A schematic representation of the tensile and compression twinning is shown in figure 2.7.

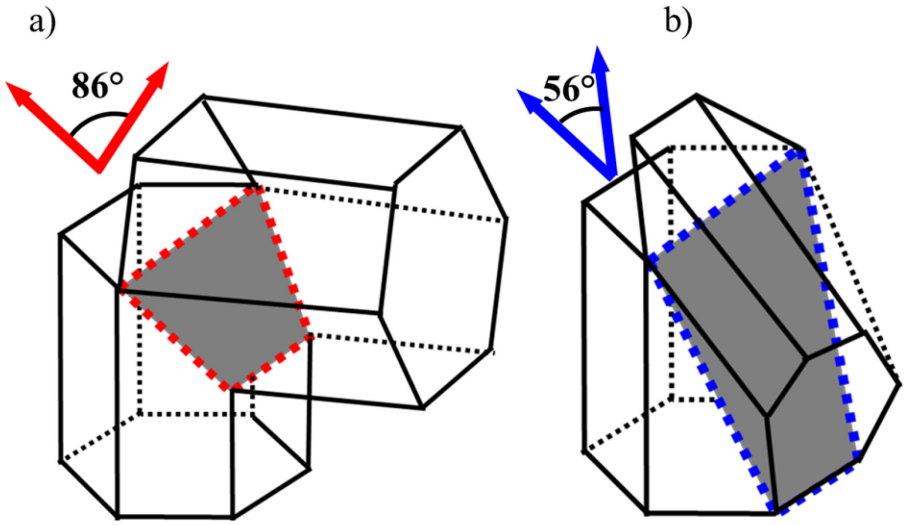

Figure 2.7. Schematic representation of twinning, a) tension twinning $(10\bar{1}2) < 10\bar{1}\,\bar{1} >$ and b) compression twinning $(10\bar{1}1) < 10\bar{1}\,\bar{2} >$ [59].

2.4 Extrusion process

Extrusion is an important processing method for producing different kind of profiles in a single forming step. In this forming process, a billet, usually round, is pressed by a stem at high pressure through a tool of the desired shape, the die [11] .

The extrusion processing is usually subdivided according to the billet temperature, i.e., cold or hot extrusion and the relative movement of the extruded material and the ram. Concerning to the relative movement of the material and the ram, the two basic types of extrusion are the direct and indirect extrusion [60]. In figure 2.8 is depicted a schematic representation of both extrusion process.

In ***direct extrusion***, a ram, usually with a pressure pad in front, pushes the billet in a stationary container through a tool of the desired shape, the die. Relative movement takes place between the billet and the container [11].

In contrast, in ***indirect extrusion,*** the die is located in front of a hollow ram and pushed against the billet by the forward movement on the container closed to at the back. There is, therefore, no relative movement between the billet and the container [11].
The properties of the extruded bars are affected greatly by the way in which the metal flows during extrusion. The metal flow is influenced by parameters like the extrusion ratio, the billet temperature, the ram or extrusion speed and the frictional conditions at the die and container wall [11, 60]. The first three parameters are the most usually varied in order to control the extrudability of the material and the resulting conditions of the produced bars.

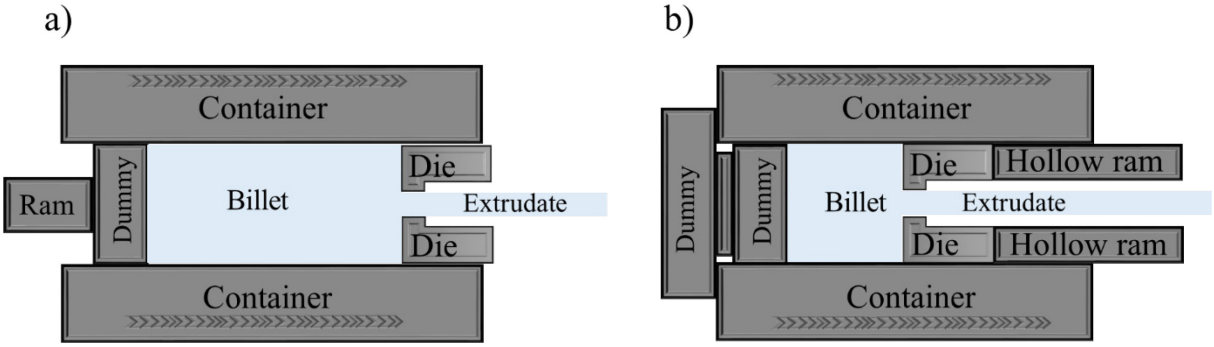

Figure 2.8. Schematic representation of the extrusion process; a) Direct extrusion, and b) Indirect extrusion [11].

2.5 Extrusion of magnesium alloys

Magnesium alloys are usually extruded in the rage of 250 °C- 450 °C [61]. Diverse factors affect its extrudability. The property of extrudability refers to the multivariable processing window of an alloy during extrusion [12]. The press limit (left lines) and the limit of hot cracking (right lines) determine the extrusion window as is shown in figure 2.9. In comparison with the aluminum extrusion alloys, magnesium alloys have lower extrudability, i.e. they must be extruded at lower speeds and within a narrower range of extrusion temperatures [62]. Therefore, this low extrudability of magnesium alloys leads to a lower production efficiency and higher cost than aluminum extrusion alloys.

Magnesium alloys such as AZ61, ZK60 and alloys with high amount of rare earth elements have a low extrudability owing to these alloys are hard and the extrusion press machine cannot

press them at low extrusion temperature. Thus, they must be extruded at high temperature with low extrusion speed. Attention should be paid to the control of the extrusion speed; this is because when the extrusion speed is beyond the right limit of the adequate processing window some cracks are formed in the surface of the extruded profiles. These cracks formed during extrusion are known as hot shortness [63]. The hot shortness phenomenon is formed when the local temperature in the die exceeds the solidus temperature of the alloy or the melting temperature of the second phases [64].

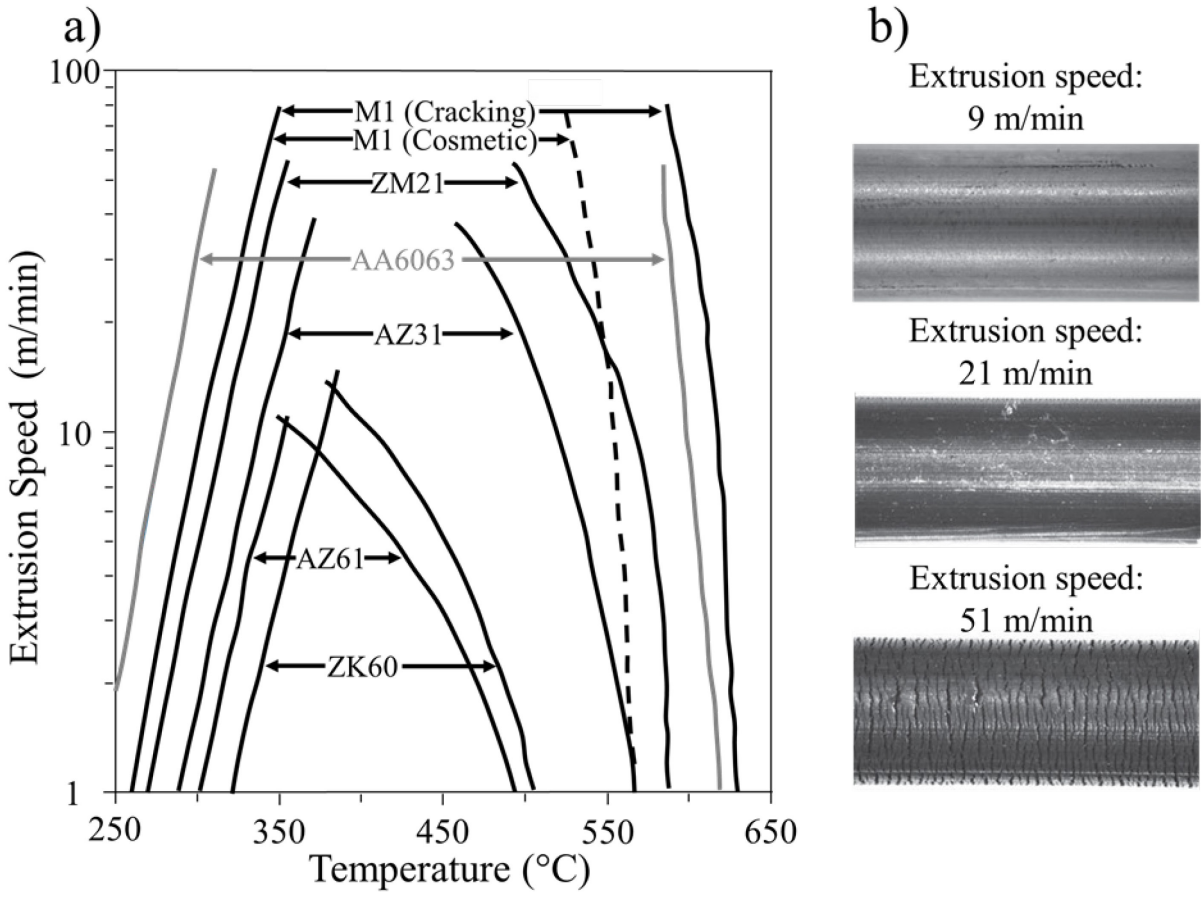

Figure 2.9. a) Extrusion limits diagrams of some commercial Mg alloys and the Al-alloy AA6063 [62], and b) surface quality of AZ31 extruded at 375 °C and different extrusion speeds [63].

The alloy design has been applied to enhance the extrudability. The low alloying concentration on the magnesium alloys is related to a softer deformation during extrusion and thus a lower extrusion temperature and higher speeds can be tolerated before the press capacity is reached [12]. Then, a lower alloy content can result in better extrudability.

In recent years, diverse research have been done with the aim to obtain a high performance on the extruded magnesium alloys. In that regard, the development on the extruded magnesium alloys has been focused mostly in the evolution of the microstructure as well as the crystallographic texture. Of these two alloy characteristics, the investigation of the basal texture weakening has received much more attention. Such microstructure or crystallographic texture evolution has been associated to dynamic or static recrystallization. Diverse recrystallization or deformation mechanisms have been considered to explain the formation of different texture after processing.

It is well accepted that in the evolution of microstructure and crystallographic texture, the temperature plays an important role to a great extent. During the deformation, cross slip and climb are the main plastic deformation mechanisms in the extruded magnesium alloys, besides at high temperatures usually dynamic recrystallization occurs. The combination of both, recrystallization and deformation mechanisms are implied in the crystallographic texture formation.

In the selection of the appropriate process parameters, it is important to consider the effect of the selected alloying elements on the extrudability of magnesium. A high extrudability can be reached by using alloying elements that can increase the solidus temperature of the alloy, such as Ca and RE elements.

In case of Zn, this element decreases the solidus temperature of the alloy or induce the formation of second-phase particles with low melting temperature [12], then its presence in magnesium should be low. Murai et al [65] found that during direct extrusion, Zn additions greater than 1 wt. % promoted the occurrence of hot-cracking. Yan and Chen [66] reported that Ca additions promotes an increase in the solidus temperature, they found that the excellent extrudability of the dilute Mg-Zn-Ca-Mn alloys can be mainly ascribed to the thermally stable Mg_2Ca phase and high solidus temperatures of ~620 °C. In the case of the rare earth alloying elements, the high content of it produces a low extrudability of magnesium alloys [12]. The RE elements such as Ce, Gd, Y, La and Nd are commonly added to improve the mechanical properties of magnesium via microstructure and texture modification.

2.6 Recrystallization in magnesium alloys

The recrystallization process is defined as the replacement of a deformed microstructure by a new set of strain-free grains, this process involves the nucleation and subsequent growth of the new grains at the expense of the surrounding deformed grains [67].

There are two types of recrystallization, i.e. dynamic (DRX) and static recrystallization (SRX). During the extrusion processing the microstructure of magnesium changes significantly, which includes both, the dynamic and static recrystallization. In figure 2.10 is depicted a representation of the possible softening process during extrusion.

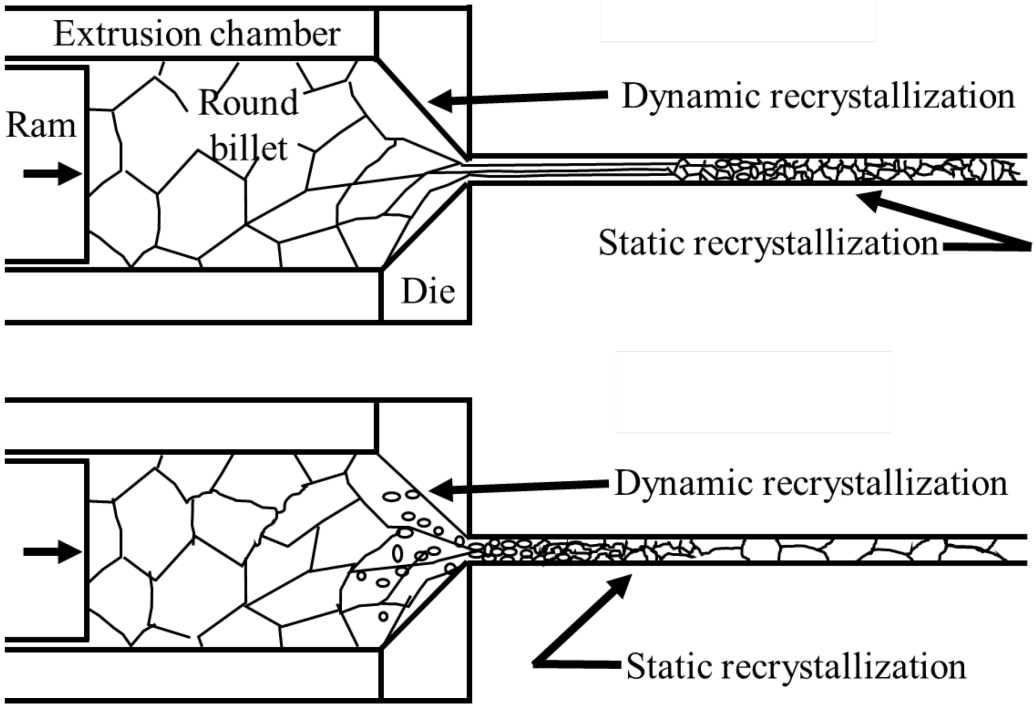

Figure 2.10. Schematic representation of possible softening process during extrusion [68].

Considering the tree most important extrusion parameters, i.e., temperature, speed, and ratio, three different mechanisms of DRX have been observed to operate in magnesium during processing [69]. The continuous DRX (CDRX), discontinuous DRX (DDRX) and twin DRX (TDRX) are included on those three types of DRX.

The continuous DRX (CDRX) consists of the formation of stable three-dimensional arrays of deformation low angle boundaries (LAGBs) followed by their gradual transformation into high angle grain boundaries (HAGBs) upon straining [67, 70, 71]. During the CDRX, a rotation and migration of low-angle grain boundaries take place homogeneously in the microstructure, therefore this type of recrystallization could be considered as an extended recovery phenomenon [39].

The discontinuous DRX (DDRX) involves the development of HGABs via the nucleation and growth of new grains. The nuclei develop on original HGABs due to the operation of a bulging mechanism [72, 73]. Such recrystallization mechanisms usually occur in materials with relatively low stacking fault energies [67, 73]. The local migration of the grain boundaries, i.e. bulging, leads to the formation of nuclei, which then grow out and consume a deformed matrix, resulting in decreased dislocation density, and providing strain softening. Thus, this mechanism involves the development of high-angle grain boundaries via the nucleation and growth of new grains. It is closely related to strain induced migration of initial boundaries [69, 74].

Finally, the DRX mechanism associated with twinning (TDRX); in this case, the twinning leads to the formation of coarse lamellae surrounded by special grain boundaries [75]. This mechanism can occur by at least three processes. Such processes are (1) mutual intersection of primary twins, (2) the occurrence of secondary twinning within the coarse lamella and (3) the subdivision of the coarse twin lamellae [72, 76].

The recrystallization process inside the twins is governed by local recovery, which can be possible by slip assisted or thermally activated, which gives to the formation of sub-grains similar to twin orientations [77, 78]. Studies indicate that the nucleation inside the compression and double twins can give rise to soft orientations, which gives an important role in the recrystallization texture modification [79, 80]. A higher thermal activation can trigger growth of such orientations owing to the associated high driving pressures [81].

The deformation during processing leads to a buildup of dislocations and this increases the amount of strain energy stored in the material [82]. Then, during the subsequent annealing of the hot deformed material, there is a reduction of this stored energy, which drives the nucleation and growth of new, strain-free grains, i.e., the static recrystallization (SRX) occurs [67]. During the static recrystallization (SRX) of Mg alloys, the formation of twins plays an important role. It has been shown that under certain conditions, the Mg and Mg alloys have a tendency to form twins during the deformation processing [81, 83-85]. Studies have revealed that the twins and the twin boundaries serve as dominant nucleation sites during recrystallization of Mg alloys [81, 83-87].

2.7 Texture of magnesium alloys

Due to of the effects of deformation and recrystallization during the processing, the magnesium alloys develop a crystallographic texture or crystallographic orientation. The *crystallographic orientation*, or in this context simply *texture*, refers to how the atomic planes in a volume of crystal are positioned relative to a fixed reference [88].
Due to the anisotropy of magnesium single crystals combined with the uniaxial character of deformation twinning [89], the crystallographic texture of a polycrystalline material plays an important role on the impact on the deformation behavior of magnesium wrought products.
The global behavior of the polycrystalline material is somewhat similar to that of a single crystal if the texture is strongly developed; therefore, the anisotropy of the HCP structure of magnesium is also carried over to the thermo-mechanically processed polycrystalline material.

During the thermomechanical processing, some specific planes or directions can be strongly oriented with respect to a specific direction in the material, for example, the extrusion direction of the extruded bar. Figure 2.11 shows a schematic representation of the alignment of basal planes during extrusion.

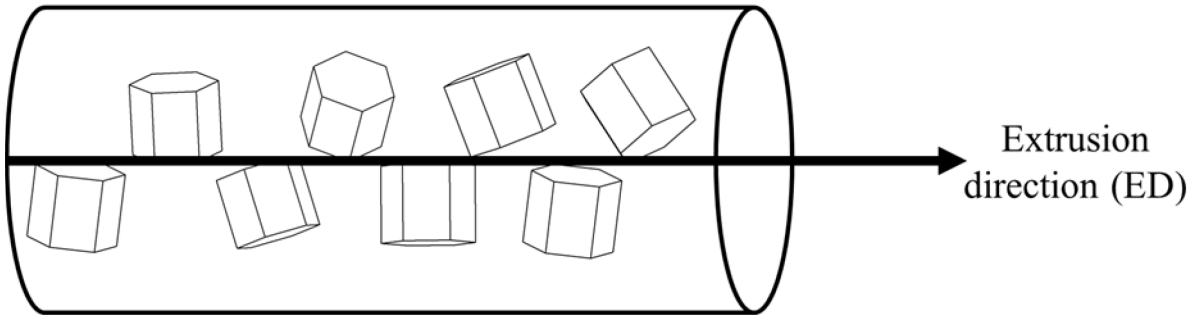

Figure 2.11. Schematic representation of the distribution of magnesium crystals after extrusion [90].

The X-Ray diffraction technique is normally applied to do texture analysis of the processed materials. The quantitative determination of textures can be done using a pole-figure goniometer, which uses a reflection geometry and a monochromatic X-rays Cu Kα radiation.

In the goniometer, the source and counter are arranged in a fixed geometry, depending only on the Bragg angle of the investigated crystallographic plane. The Bragg angle refers to a reflection condition if Bragg's law is obeyed [91]:

$$n\lambda = 2d \sin\theta \qquad \text{(Eq. 2)}$$

Where:
λ is the wavelength, *d* is the spacing of the reflecting planes, θ is the angle of incidence and reflection and *n* is the order of diffraction

The sample is mounted on a holder, which can be rotated around two perpendicular axes to orient the specimen in any position with respect to the incident X-ray beam. The goniometer moves the detector with respect to the X-ray beam (rotation 2θ); the sample is positioned relative to the X-ray beam by two rotations, Φ and χ. Figure 2.12 displays the definition of such rotations. The χ circle is generally symmetrical between incoming and diffracted beam (positioned at an angle θ). The 2θ and ω axis coincide. The nomenclature Φ, χ, and θ is standard in single crystal diffractometry and marked on most instruments. In a pole figure goniometer, the crystallographic 'goniometer head' is replaced by a texture attachment on which the sample can be mounted and oscillated. Stepper motors, controlled by a personal computer, enable one to obtain any arbitrary angular position on the three axes 2θ, χ and Φ (within a certain range to avoid mechanical collisions). The axe ω sets only the detector to the proper Bragg angle, 2θ, of the diffraction peak of interest [92].

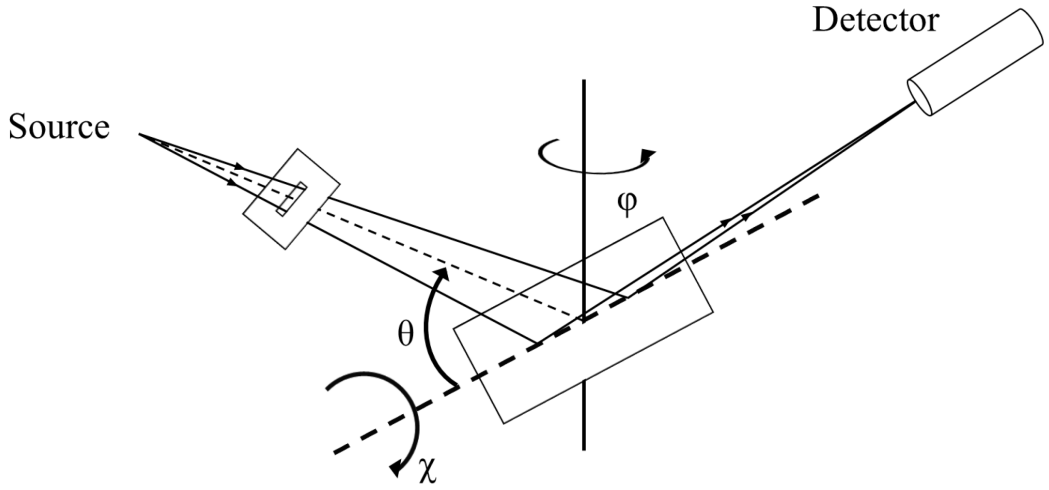

Figure 2.12. Ray path and sample rotation in an X-ray texture goniometer and definition of the instrument angles [92].

The movement of the specimen unveils the spatial orientation of the respective poles $\{hkl\}$. In a stereographic projection, the measured intensity distribution generates the $\{hkl\}$ pole figure (P.F). A pole figure (P.F) is a two-dimensional stereographic projection in which the positions and intensities of specific crystallographic orientations are plotted in relation to the specimen geometry. In figure 2.13a is displayed a pole figure that shows the distribution of a selected crystallographic direction relative to certain directions in the specimen. In the case of magnesium, typical pole figures of interest are (0001), $(11\bar{2}0)$, $(10\bar{1}0)$, $(10\bar{1}1)$, $(10\bar{1}2)$ and $(10\bar{1}3)$.

Drawing the conventional pole figures is the most common method to represent textural data for materials. Nevertheless, the satisfactory description of texture, sometimes, can also be given

in terms of an inverse pole figure (IPF). In such inverse pole figure, the distribution of a selected direction in the sample is depicted in relation to the crystal axes. The representation in the I.P.F is exactly inverse of the pole figure. In the I.P.F, the sample directions are projected into the crystal frame as opposed to pole figures, which are essentially the projection of crystallographic directions in the sample frame of reference. For an I.P.F, the projection plane is a standard projection of the crystal, of which only the unit stereographic triangle needs be shown. Figure 2.13b shows the stereographic projection of a standard representation of an inverse pole figure in the HCP lattice structure. The texture component $< 0001 >$ is associated to the basal planes of the HCP structure, while the $<10\bar{1}0>$ and the $<11\bar{2}0>$ are related to the prismatic planes of the first and the second order, respectively.

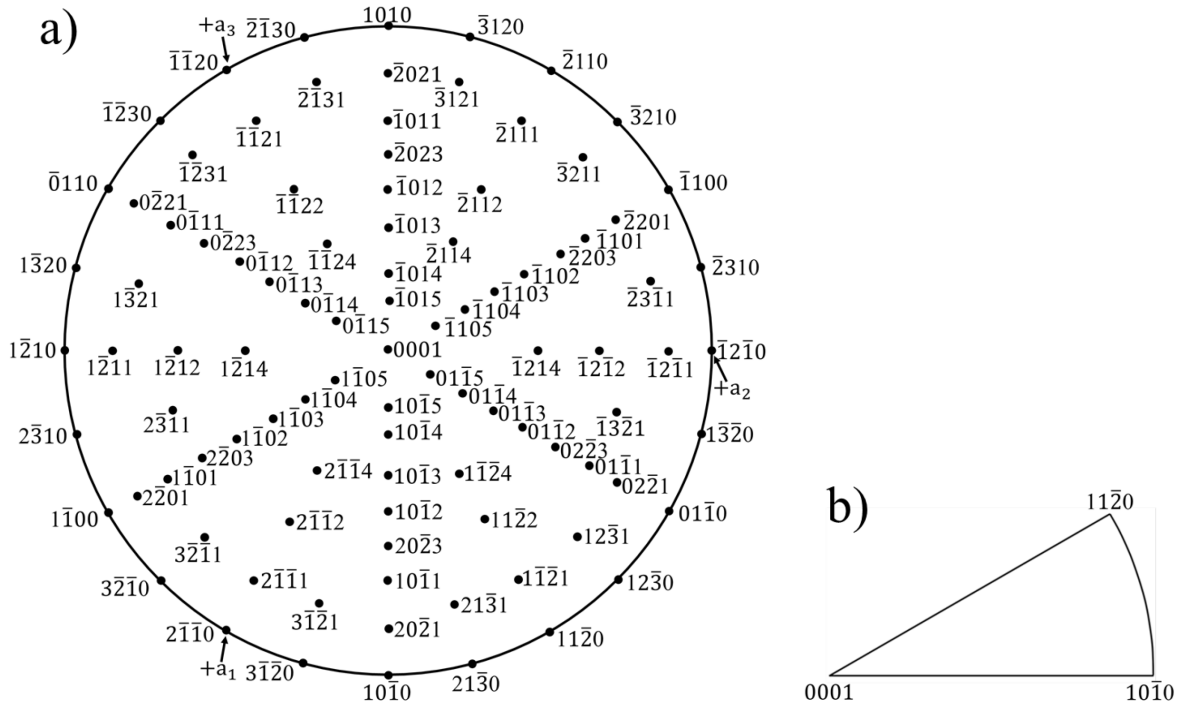

Figure 2.13. a) Standard (0001) stereographic projection of an HCP crystal structure [91], and b) inverse pole figure (I.P.F) used in this study for the representation of textures in extruded bars [91].

2.8 Mechanical properties on magnesium alloys

Nowadays, the main applications of magnesium are as cast products. These cast products can be complex, but in many cases, they lack the desired mechanical properties. It is well known that the mechanical properties of magnesium and its alloys are influenced by the microstructure and texture. In general, the mechanical properties shown by the wrought magnesium alloys are better compared to the as-cast alloys; this is mainly because of the small grain size, the crystallographic texture and the absence of porosity [93]. However, still the wrought magnesium alloys have a low strength, ductility and tend to exhibit a tension-compression yield asymmetry.

The yield asymmetry refers to the difference between the yield stress (YS) in tension and in compression; the compressive YS is typically lower than the tensile YS when the material is

tested [77]. An example of texture developed in Z1 alloy as well as its mechanical properties are depicted in figure 2.14. The tension-compression asymmetry is observed (figure 2.14b). This behavior is normally associated to the texture developed during the thermomechanical processing. In these textures, the basal planes of the HCP structure of magnesium are aligned parallel to the main forming direction, [94] e.g., extrusion direction.

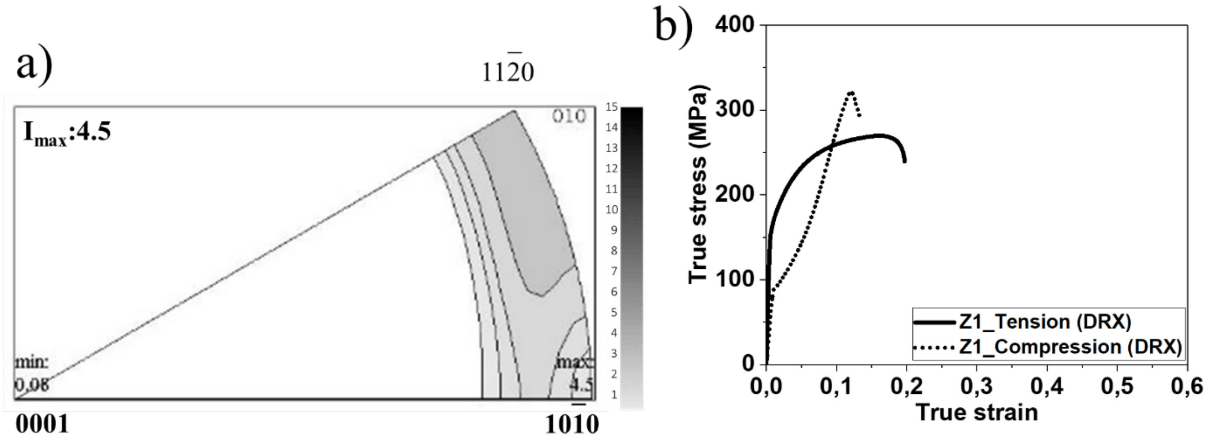

Figure 2.14. a) Texture in the form of I.P.F, and b) mechanical properties of extruded magnesium alloy Z1 [95].

Studies have been reported that the yield asymmetry is related to the twining activity [57, 96, 97]. In the textures where the basal planes are predominately oriented parallel to the extrusion direction, the twinning activity is more pronounced in compression rather than in tension. Therefore, if twinning activity could be suppressed, the asymmetry may be reduced. The reduction of twining activity can be achieved by crystallographic texture modification. Besides, it has been also reported that the grain refinement leads to a reduction in the yield asymmetry [98]. This observation is also related to twinning activity since twinning becomes less favorable if the grain size is reduced. Lately, different studies have reported that the presence of certain alloying elements on magnesium can lead to the suppression of the development of a strong fiber texture during thermomechanical processing. This idea is related with the development of weaker textures and more randomly oriented basal planes, which increases the ductility and reduces the yield asymmetry, as is shown in figure 2.15.

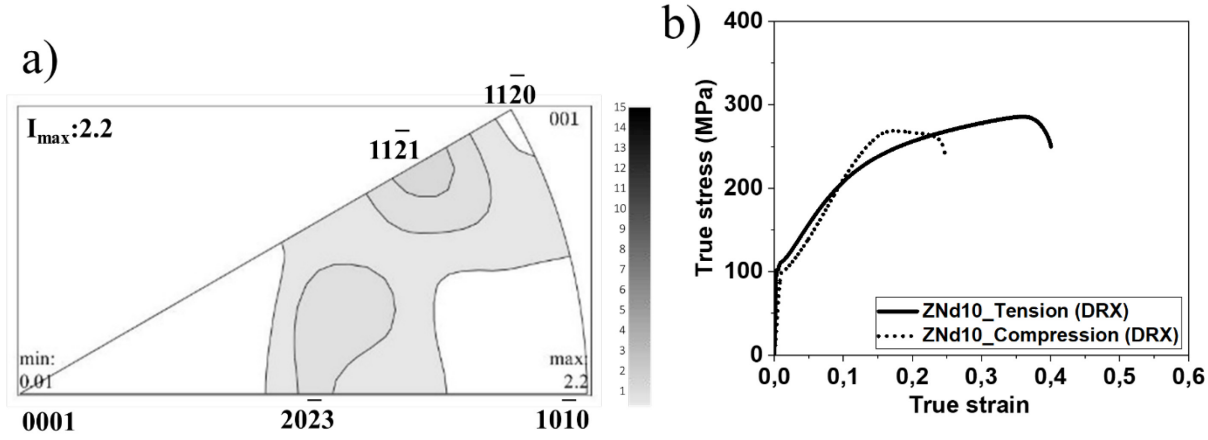

Figure 2.15. a) Texture in the form of I.P.F, and b) mechanical properties of wrought magnesium alloy ZNd10 [95].

2.9 The Visco-Plastic Self-Consistent model

The use of semi-finished magnesium products is still limited due to its low mechanical properties, which is normally associated to the lack of adequate activation of slip modes. The differences in the texture of such semi-finished products developed during processing can have significant effects on its mechanical properties. For this reason, it is of fundamental interest to gain a more detailed insight during the deformation of magnesium alloys. In that regard, the modelling of deformation behavior plays an important role on a better understanding of the deformation of magnesium alloys. The crystal plasticity simulations is a powerful tool that have been used for simulating the deformation. Different plasticity models have been suggested to simulate the deformation. For the understanding of the deformation modes in the extruded magnesium alloys of this research work, the visco-plastic self-consistent model (VPSC) has been applied.

The VPSC model is a computer code written mostly in Fortran 77. The VPSC model stands for Visco Plastic Self Consistent and refers to the particular mechanical regime addressed (VP) and to the approach used (SC). It allows the simulation of the plastic deformation of polycrystalline aggregates. Such model it is been developed for application to low-symmetry materials like hexagonal, trigonal, orthorhombic, monoclinic, triclinic, but also performs well when simulating plasticity of cubic materials. It simulates the plastic deformation of aggregates subjected to external strain, external stress, or a combination of both. It is based on the physical shear mechanisms of slip and twinning, and accounts for grain interaction effects. The model considers the deformation based on the crystal plasticity mechanisms activated by a Resolved Shear Stress [99]. In addition to the provided macroscopic stress-strain response, it accounts for hardening, reorientation and shape change of individual grains. Therefore, it predicts the evolution of hardening and texture associated with plastic forming.

As it is well known, the deformation is accommodated by crystallographic slip and twin shear rates inside the grains. In that sense, it is typically assumed that in the HCP metals, the shear is accommodated by $\{0001\} < 11\bar{2}0 >$ basal slip, $\{10\bar{1}0\} < 11\bar{2}0 >$ prismatic slip, $\{10\bar{1}0\} < 11\bar{2}3 >$ pyramidal slip and $\{10\bar{1}2\} < 10\bar{1}1 >$ tensile twinning. Their threshold stresses for activation are very different depending on the material, temperature and deformation rate. The threshold stress describes the resistance for activation that the deformation mechanisms experience, and it usually increases with deformation. Then, the VPSC model has the capability of using a reference hardening function for each system, described by an extended Voce law [100].
The Voce hardening is characterized by an evolution of the threshold stress with accumulated shear strain in each grain of the form:

$$\hat{\tau}^s = \tau_0^s + (\tau_1^s + \theta_1^s \Gamma)(1 - \exp\left(-\Gamma \left|\frac{\theta_0^s}{\tau_1^s}\right|\right)) \quad \text{(Eq.3)}$$

Where

$\Gamma = \sum_s \Delta\gamma^s$ is the accumulated shear in the grain, τ_0 is the initial CRSS, θ_0 is the initial hardening rate, θ_1 is the asymptotic hardening rate and $(\tau_0 + \tau_1)$ corresponds to the back extrapolated CRSS.
Furthermore, the code also incorporates the 'self' and 'latent' hardening defining the coefficient $h^{ss\prime}$, which account for the obstacles that new dislocations associated with s' activity represent for the propagation of system 's'. The increase of the threshold stress of a system due to the shear activity $\Delta\gamma^s$ in the grain is given by:

$$\Delta\tau^s = \frac{d\hat{\tau}^s}{d\Gamma}\sum_{s'} h^{ss'}\,\Delta\gamma^{s'} \qquad \text{(Eq. 4)}$$

Where

$$\frac{d\hat{\tau}^s}{d\Gamma} = \left[\theta_1 + \left(\left|\frac{\theta_0}{\tau_1}\right| + \tau_1 - \theta_1\right) exp\left(-\Gamma\left|\frac{\theta_0}{\tau_1}\right|\right) + \left|\frac{\theta_0}{\tau_1}\right| \theta_1\Gamma\, exp\left(-\Gamma\left|\frac{\theta_0}{\tau_1}\right|\right)\right] \qquad \text{(Eq. 5)}$$

The code uses the self-hardening as a reference and set $h^{ss} = 1$. At that time, when 'self' and 'latent' hardening are indistinguishable, then $h^{ss'} = 1$, the evolution of threshold stress is given by only the Voce hardening function:

$$\Delta\tau^s = \frac{d\hat{\tau}^s}{d\Gamma}\Delta\Gamma \qquad \text{(Eq. 6)}$$

The hardening law labeled in the equations previously showed, let to describe the hardening rate observed at the beginning of plasticity and its decrease towards constant hardening rate at large strains. The condition $\theta_0 \geq \theta_1 \geq 0, \tau_1 \geq 0$ corresponds to an increment of the yield stress and a reduction of the hardening rate with a tendency to linear saturation. The linear hardening corresponds to a limit case of the law corresponding to $\tau_1^s = 0$ while the case of rigid-perfectly plastic hardening corresponds to $\theta_0 = \theta_1 = \tau_1 = 0$. This is schematically exemplified in figure 2.15a.

The incremental expression referred in Eq. 6 represents a forward extrapolation, which tends to overestimate the hardening and make it dependent on the step size, more so when the derivative is large. Consequently, in the code is implemented an analytic integration of Eq. 6. Normally, the evolution of the threshold stress represented by Eq. 3 is monotonically increasing and the hardening rate Eq. 4 is monotonically decreasing. This is achieved using a 'kosher' set of parameters $\tau_0 > 0,\ \tau_1 > 0,\ \theta_0 > \theta_1 > 0$. Nevertheless, for some empirical cases, it is possible to use parameters giving monotonic decrease $\tau_0 > 0,\ \tau_1 < 0,\ \theta_0 < \theta_1 < 0$ or increased the hardening rate $\theta_1 > \theta_0 > 0$. The VPSC model accepts parameters describing negative hardening. The figure 2.15b shows possible configurations of Voce parameters leading to non-classic hardening.

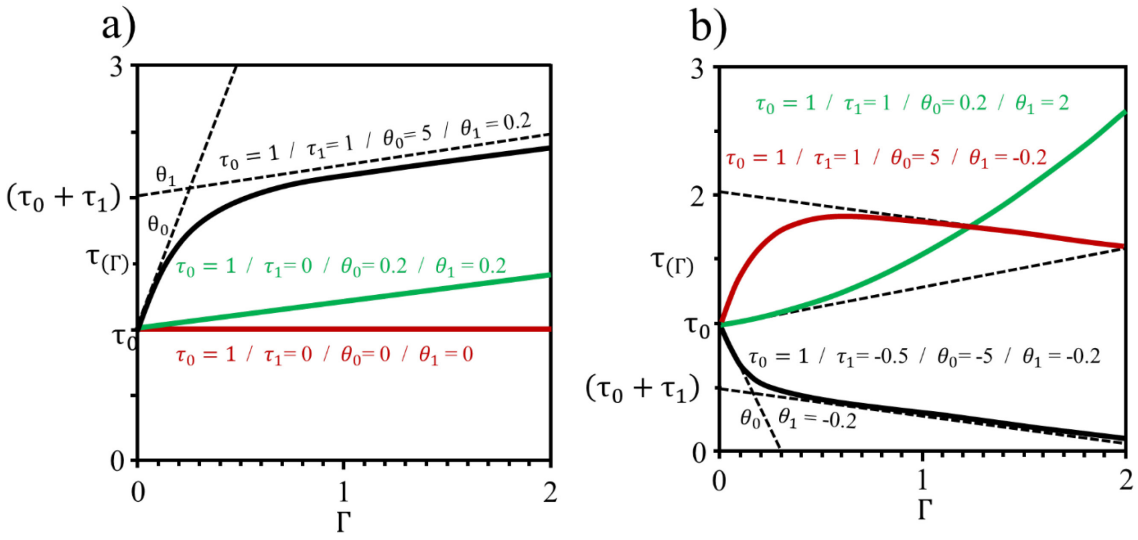

Figure 2.16. Schematic representation of a) the dependence of the hardening curve on the modified Voce model parameters, and b) possible configurations of Voce parameters leading to non-classic hardening [99].

In the VPSC model is assumed that twinning has associated a critical resolved shear of activation in the twinning plane and along the twinning direction, like a slip system. However, it differs from slip in its directionality, which is modeled by allowing activation only if the resolved shear stress is positive along the Burgers vector of the twin. Here, the hardening induced by twinning is empirically enforced by assigning high values to the latent hardening coefficients $h^{ss'}$ describing slip-twin and twin-twin interactions.
As for the effect on texture of the twinned fractions, here it is used the Predominant Twin Reorientation Scheme (PTR) proposed by Tomé et al [101].
Such PTR scheme works as follows: within each grain g it is keep a track of the shear strain $\gamma^{t,g}$ contributed by each twin system t, and of the associated volume fraction $V^{t,g} = \gamma^{t,g}/S^t$ as well. In this case, S^t refers to twin shear. The sum over all the twin systems associated with a given twin mode, and over all grains, represents the accumulated twin fraction ($V^{acc,\ mode}$) in the aggregate for the particular twin mode.

$$V^{acc,mode} = \sum_g \sum_t \gamma^{t,g}/S^t \qquad \text{(Eq. 7)}$$

Each twinned fraction is not numerically feasible to be considered as a new orientation, then; in the PTR scheme is adopted a statistical approach. At each incremental step, some grains are fully reoriented by twinning, provided certain conditions are fulfilled.

This is call as 'effective twinned fraction' ($V^{eff,\ mode}$) the volume associated with the fully reoriented grains for that mode, and define a threshold volume fraction as

$$V^{th,\ mode} = A^{th1} + A^{th2}\ \frac{V^{eff,\ mode}}{V^{acc,\ mode}} \qquad \text{(Eq. 8)}$$

After each deformation increment, a grain is picked at random and is identified the twin system with the highest accumulated volume fraction.
If the latter is larger than the threshold ($V^{th,\ mode}$) then the grain is allowed to reorient and ($V^{eff,\ mode}$) and $\left(V^{th,\ mode}\right)$ are updated. The process is repeated either until all grains are randomly checked or until the effective twin volume exceeds the accumulated twin volume. In the latter case, it is stopped the reorientation by twinning and proceed to the next deformation step. In this process, two things are achieved: a) only the historically most active twin system in each grain is considered for reorienting the whole grain by twinning; b) the twinned fraction is consistent with the shear activity that the twins contribute to deformation. The algorithm given in Eq. 8 prevents the grain reorientation by twinning until a threshold value A^{th1} is accumulated in any given system and rapidly raises the threshold to a value around $A^{th1} + A^{th2}$.
The input to the code consists in the initial crystallographic texture (grain orientations and weights), the single crystal properties (active slip and twinning systems, their critical resolved shear stresses, and the associated hardening parameters), the boundary conditions (overall velocity gradient components, or overall stress components) and the parameters controlling convergence, precision and type of run. The output of the code is: the final crystallographic and morphologic textures after deformation (additionally is also possible to obtain the intermediate textures), the evolution of the stress and strain components during deformation, the statistics of slip and twinning systems activity during deformation, the statistic over grain stress and strain-rate components and their standard deviations.

2.10 Summary and motivation of the work

In summary, Magnesium and its alloys have a great potential to be used in the replacement of diverse components in automotive, aerospace and biomedical industries. Nevertheless, the low strength, limited ductility and high anisotropy still limit the use of wrought Mg alloys. Such issues are directly associated to the limited number of active slip systems in directions other than those contained in the basal planes of the HCP structure. Usually, the activation of determined slip systems are connected to the texture of the Mg alloys. In agreement to that, great progress has been made in the last decade to produce alloys and design thermomechanical treatments for modifying the texture to overcome the issues previously mentioned. However, still significant efforts are required to optimize the microstructure and mechanical properties. It is known that thermomechanical processes like rolling or extrusion have been employed to enhance the microstructure of Mg alloys. Concerning to extrusion process, it has a high potential to be employed in the manufacturing of components for industrial applications. For years, many studies have been realized while focusing in the classical wrought Mg alloys such as AZ31. More recently, Mg alloys with additions of Rare earth elements (RE) like Nd or Calcium (Ca) show important improvements on the mechanical behavior. The combination of Zn with Ca or Nd can create a synergetic effect to modify the microstructure and texture of Magnesium alloys. The processing routes combined with alloying elements offer the prospect to modify the microstructure and the strong textures of wrought Mg alloys and hence their mechanical behavior. Therefore, a profound understanding of the correlation between processing parameters and the microstructure as well as the microstructure-mechanical properties correlation of the processed alloys is necessary for tailoring materials for specific applications or for processes post-extrusion.
During deformation, in addition to the activation of basal <a> mode, the Ca or Nd additions into Mg-Zn alloy system, activate non-basal deformation modes, for instance, prismatic <a> and pyramidal <c+a> at low temperatures. Such deformation modes mitigate the need of twinning and thus improve ductility and reduce the tension-compression yield asymmetry. However, although Ca or Nd additions offer the prospect to improve mechanical properties, understanding of the mechanisms by which they can enhance it is still lagging. Consequently, the study of the effect of initial microstructure and texture is fundamental to understand which slip modes are activated to satisfy the material behavior during deformation and texture development.

3. Experimental procedure

3.1 Studied and cast alloys

In this work, three different alloys were investigated. The base alloy Z1 (Mg-Zn) was modified with separate additions of Calcium and the rare earth element Neodymium to obtain the ZX10 (Mg-Zn-Ca) and ZNd10 (Mg-Zn-Nd) alloys, respectively.

The billets for extrusion processing were produced by permanent mold casting. The alloying element additions were added to the molten magnesium in the furnace at temperatures between 750 and 770 °C. The molten melt was stirred for around 15 minutes to make a homogeneous material before pouring. Table 3.1 shows the chemical composition of each alloy. The values are in weight percent. The figure 3.1a shows an example of the billets after casting. In the preparation of the material for extrusion, the cylindrical billets were prepared with a length of 150 mm and a diameter of 49 mm. An example of the billets prepared with the dimensions for extrusion processing is depicted in figure 3.1b.

Table 3.1. Chemical composition of each alloy.

	Chemical composition (wt%)			
Alloy	Zn	Ca	Nd	Mg
Mg-Zn	0.91	----------	----------	Bal.
Mg-Zn-Ca	0.94	0.15	----------	Bal.
Mg-Zn-Nd	0.98	----------	0.57	Bal.

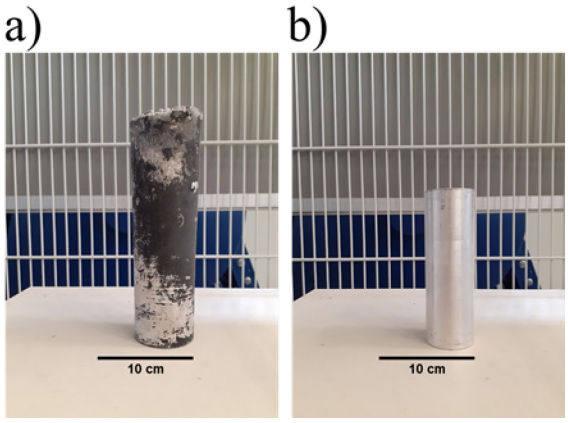

Figure 3.1. a) Billet after casting process, and b) prepared billet for extrusion processing.

3.2 Heat treatments before extrusion

Solution heat treatments were applied to the billets before extrusion. For the Z1 and ZX10 alloys, the heat treatments were done at 400 °C. In case of the ZNd10 alloy, the applied temperature was 450 °C.

A higher temperature was required for the ZNd10 alloy because of complexity to achieve a solid solution. In each alloy, the heat treatment was applied for 16 hours. In the figure A.1 of appendix, the zones that were reached during the solution treatments are depicted.

3.3 Extrusion process

The thermomechanical process chosen for the processing of the selected alloys was indirect extrusion. The billets were preheated before extrusion at the extrusion temperature for 60 minutes. The selection of the first parameters like extrusion speed and extrusion temperature was done according to the literature review. A constant extrusion ratio was used during the extrusion modifying the temperature and speed. The modification of extrusion speed and temperature led to obtain different materials in terms of microstructure and texture in each alloy. The obtained results allowed analyzing the effect of both parameters on the recrystallization behavior as well as show a processing window in each alloy. The extrusion experiments were executed at the Helmholtz-Zentrum Hereon. It was carried out using a 2.5 MN automatic extrusion press of Müller Engineering (Müller Engineering GmbH & Co. KG, Todtenweis/Sand, Germany), see Figure 3.2.

Specifications	
Maximum ram speed	8.0 mm/s
Diameter of the container	50 mm
Length of the billet	150 mm
Press force	2.5 MN

Figure 3.2. Extrusion press machine of the Magnesium Innovation Center at the Helmholtz-Zentrum Hereon.

3.4 Indirect extrusion

The applied parameters during the indirect process are shown in Table 3.2. It was used as an extrusion die with a round hole of 10 mm in diameter. The combination of the extrusion parameters and the die used allowed the production of extruded round bars with a diameter of 10 mm.

Table 3.2. Extrusion parameters during processing.

Indirect extrusion				
Extrusion temperature (°C)	Extrusion speed (mm/s)			Extrusion ratio
250	2.0	5.0	7.5	1:25
300	2.0	5.0	7.5	1:25
400	2.0	5.0	7.5	1:25

3.5 Post-extrusion heat treatments

To understand the effect of static recrystallization on the microstructure and texture development, partly recrystallized microstructures were annealed to fully recrystallized microstructures. The partly recrystallized samples from ZX10 and ZNd10 were obtained at 0.1 mm/s of extrusion speed and 300 °C of extrusion temperature. The Z1 alloy does not presented changes in the texture after SRX because of the high fraction of recrystallized microstructure

found even in samples extruded at low speed. Therefore, it analysis is not presented. The microstructures of samples from the ZX10 and ZNd10 alloys were tailored so the grain size of the SRX samples could be compared to grain structures of DRXed samples, i.e. samples from ZX10 alloy (extruded at 300 °C and 2.0 mm/s) and ZNd10 alloy (extruded at 300 °C and 5.0 mm/s). The partly recrystallized samples were annealed at 400 °C for 3.0 minutes in case of ZX10 alloy and 30 minutes for the ZNd10 alloy.

3.6 Microstructure characterization

To study the microstructure development of each alloy, samples from the extruded bars were obtained, and then those samples were prepared following the standard methodology for metallographic observations. The samples were taken from the middle of each extruded bar. Then, the samples were ground to obtain a surface perpendicular to the extrusion direction. The grinding procedure started with a grinding paper of the number 500 finishing such process with a grinding paper of the number 2500. Then, the polishing process using a colloidal suspension (Struers OPS). Following this, an etchant liquid based on picric acid was used to reveal the microstructure.

The microstructure of all the alloys were observed by light optical microscopy. Pictures of each etched sample were taken at different magnifications using a Leica optical microscope (Leica DM15000M). The average grain size of each material was determined on pictures at 100X by means of the computer software AnalySIS Pro™ that uses the linear intercept method. The preparation of the samples for texture analysis followed exactly the methodology previously explained with the difference that the samples were not etched. Pole figures $(11\bar{2}0)$, (0001), $(10\bar{1}0)$, $(10\bar{1}1)$, $(10\bar{1}2)$, $(10\bar{1}3)$ were measured up to a tilt angle of 70° in a Panalytical texture goniometer (PANalytical X'Pert PRO MRD). A beam size of 1.0 mm^2 and Cu Kα radiation were employed during the operation of the texture goniometer. The inverse pole figures were recalculated using an open-source code MTEX [102].

The electron back scattered diffraction (EBSD) technique was employed to do a more detailed microstructure and grain orientation analysis. The sample preparation consisted on the implementation of the standard metallographic techniques followed by electro polishing using an AC2 solution (Struers ™) at 30 V for 25 s at -20 °C. The EBSD analyses were performed to measure the local orientation patterns using a field emission scanning microscope (Zeiss, Ultra 55, EDAX/TSL) on the longitudinal sections of the samples. The operation voltage was 15 kV and the used scanning step size was 0.45 μm.

3.7 Mechanical characterization

The mechanical properties were characterized applying uniaxial tensile and compression testing at room temperature. Samples for tensile tests were prepared with a diameter of 5.0 mm and a gauge length of 30.0 mm. Samples for compression tests were prepared with a length of 13.5 mm and a diameter of 9.0 mm. Mechanical testing was carried out along the extrusion direction using a 50 KN testing machine (Zwick Z050). All tests were performed at a constant strain rate of 10^{-3} s^{-1}. In figure A.2 of appendix, the schematic representation of the samples used for the mechanical characterization are shown.

3.8 Slip trace analysis

Ex-situ tension and compression tests were performed on samples with comparable grain sizes but different crystallographic texture. One sample per alloy was used either in tension or in compression. The tests were performed at room temperature at a strain rate of 1.5 x 10^{-4} s^{-1} to observed slip lines of distinct deformation modes. In tension, the tests were paused at strains of 0.03 and 0.12 in the three alloys. However, in compression the Z1 alloy was paused first at 0.03 and then at 0.08 strain. On the other hand, the ZX10 and ZNd10 alloys were tested as in tension. The tests were paused at such strains to allow the EBSD data acquisition for determining the grains orientation after each strain. Slip lines on polished and electro polished samples have been observed using pictures from a Laser Scanning Microscope (LSM), Keyence VK-X100/X200 series.

The slip trace methodology applied to determine the slip activity is as follows. In first place, on (LSM) pictures, straight lines on the grains were defined. The slip traces were pointed out with a black dashed line like the one displayed in figure 3.3a. The orientation of the grains showing slip lines was obtained from the inverse pole figure (IPF) maps of EBSD, i.e. its Euler angles (figure 3.3b). The Euler angles were used as the input of a MATLAB code [103] that gives as a result the possible slip system (Figure 3.3c). In this work, the theoretical slip trace directions for 36 slip systems (SS) were computed using the Euler angles of each grain. The observed slip trace was compared to each of the possible slip systems.

Finally, the one that provides the best match was considered as the activated slip system in such a grain. An example of a basal <a> slip trace is denoted by the black dashed line; see Figure 3.3c.

In table 3.3 are depicted the slip systems considered in the slip trace analysis. The previously explained procedure was applied to each grain that showed slip traces.

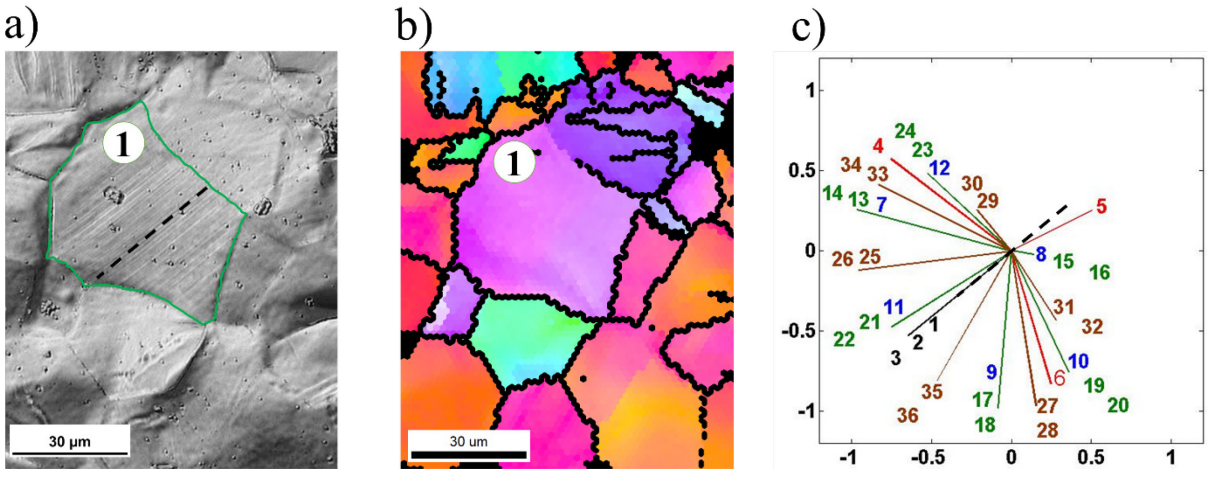

Figure 3.3. Example of slip trace analysis; a) LSM picture showing the appearance of slip trace (black dashed line), b) IPF map corresponding to the LSM picture, and c) estimation of the 36 possible slip traces and determination of the active slip system according to the best match. The black dashed line points out the corresponding slip trace.

Table 3.3. Slip systems taken into account during the slip trace analysis.

Slip system number	Slip system	Slip system type	Identification color	Slip system number	Slip system	Slip system type	Identification color
1	$<0001>(2\bar{1}\bar{1}0)$	Basal <a>	**Black**	19	$<\bar{1}011>(2\bar{1}\bar{1}3)$	Paramidal I <c+a>	**Green**
2	$<0001>(\bar{1}2\bar{1}0)$			20	$<\bar{1}011>(11\bar{2}3)$		
3	$<0001>(\bar{1}\bar{1}20)$			21	$<01\bar{1}1>(\bar{1}\bar{1}23)$		
4	$<10\bar{1}0>(\bar{1}2\bar{1}0)$	Prismatic <a>	**Red**	22	$<01\bar{1}1>(1\bar{2}13)$		
5	$<0\bar{1}10>(2\bar{1}\bar{1}0)$			23	$<1\bar{1}01>(\bar{2}113)$		
6	$<\bar{1}100>(\bar{1}\bar{1}20)$			24	$<1\bar{1}01>(\bar{1}2\bar{1}3)$		
7	$<10\bar{1}1>(\bar{1}2\bar{1}0)$	Pyramidal <a>	**Blue**	25	$<11\bar{2}2>(11\bar{2}3)$	Pyramidal II <c+a>	**Wine**
8	$<0\bar{1}11>(2\bar{1}\bar{1}0)$			26	$<11\bar{2}2>(\bar{1}\bar{1}23)$		
9	$<\bar{1}101>(\bar{1}\bar{1}20)$			27	$<\bar{2}112>(\bar{2}11\bar{3})$		
10	$<\bar{1}011>(\bar{1}2\bar{1}0)$			28	$<\bar{2}112>(2\bar{1}\bar{1}3)$		
11	$<01\bar{1}1>(2\bar{1}\bar{1}0)$			29	$<1\bar{2}12>(1\bar{2}\bar{1}3)$		
12	$<1\bar{1}01>(11\bar{2}0)$			30	$<1\bar{2}12>(\bar{1}2\bar{1}3)$		
13	$<10\bar{1}1>(\bar{1}\bar{1}23)$	Paramidal I <c+a>	**Green**	31	$<\bar{1}\bar{1}22>(\bar{1}\bar{1}2\bar{3})$		
14	$<10\bar{1}1>(\bar{2}113)$			32	$<\bar{1}\bar{1}22>(11\bar{2}3)$		
15	$<0\bar{1}11>(11\bar{2}3)$			33	$<2\bar{1}\bar{1}2>(2\bar{1}\bar{1}3)$		
16	$<0\bar{1}11>(\bar{1}2\bar{1}3)$			34	$<2\bar{1}\bar{1}2>(\bar{2}113)$		
17	$<\bar{1}101>(2\bar{1}\bar{1}3)$			35	$<\bar{1}2\bar{1}2>(\bar{1}2\bar{1}3)$		
18	$<\bar{1}101>(1\bar{2}13)$			36	$<\bar{1}2\bar{1}2>(1\bar{2}13)$		

3.9 Crystal plasticity simulations applying the VPSC model

Depending on the crystallographic texture, different combinations of deformations systems can be activated. In this work, the Visco Plastic Self Consistent (VPSC) model has been applied to simulate the plastic deformation during of the extruded bars with a comparable grain size and different crystallographic texture. The simulations with the VPSC model was carried out using the PC- based software selfcon [104].

The crystallographic texture was used in the form of discrete orientations with their weights. The texture discretization was generated using an MTEX code [102]. In order to have a better fit with the experimental texture and stress-strain curve, first a number of crystal orientations were selected.

In the development of this work, a number of 3000 crystal orientations were used. In the simulation, the considered slip modes were the basal <a>, prismatic <a> the pyramidal <a>, pyramidal I <c+a> and pyramidal II <c+a> slip as well as tensile twinning $(10\bar{1}2) < 10\bar{1}\,\bar{1} >$ and compressive twinning $(10\bar{1}1) < 10\bar{1}\,\bar{2} >$. The input parameters used at the beginning of the simulation were initially collected from different references [105-108]. Then, these parameters were modified during the course of the simulations to obtain the best fit between the experimental and simulated results, i.e., crystallographic texture (measured at the different strains) and the stress-strain curves.

4. Results

4.1 Extrusion processing

The extrusion experiments have been made at different extrusion conditions. The measured data during the processing extrusion are graphically represented in this section. In figures 4.1 to 4.3 the behavior of each alloy during the indirect extrusion processing is shown. The evolution of extrusion force during the process in each alloy is observed.

Figures 4.1 to 4.3 show the evolution of the extrusion force as a function of the ram displacement during processing. Except for the beginning of the extrusion of ZX10 alloy at 250 °C and 2.0 mm/s (Figure 4.1a), the rest of the experiments show a quite stable behavior. Once the force rises to its peak value, the force starts to decrease and a steady region during extrusion occurs, i.e., there is a displacement of the ram, but the force is constant. It is visible that in all the extrusion experiments, the addition of Ca and Nd into the binary Z1 alloy show an increase of the extrusion peak force. From the ternary alloys extruded at 250 °C and 300 °C, the highest-force peak is observed in the Ca containing alloy. At 400 °C of extrusion temperature, the force peak in the ternary alloys is similar. In all the alloys, there is a reduction of the extrusion force with the increase of extrusion temperature.

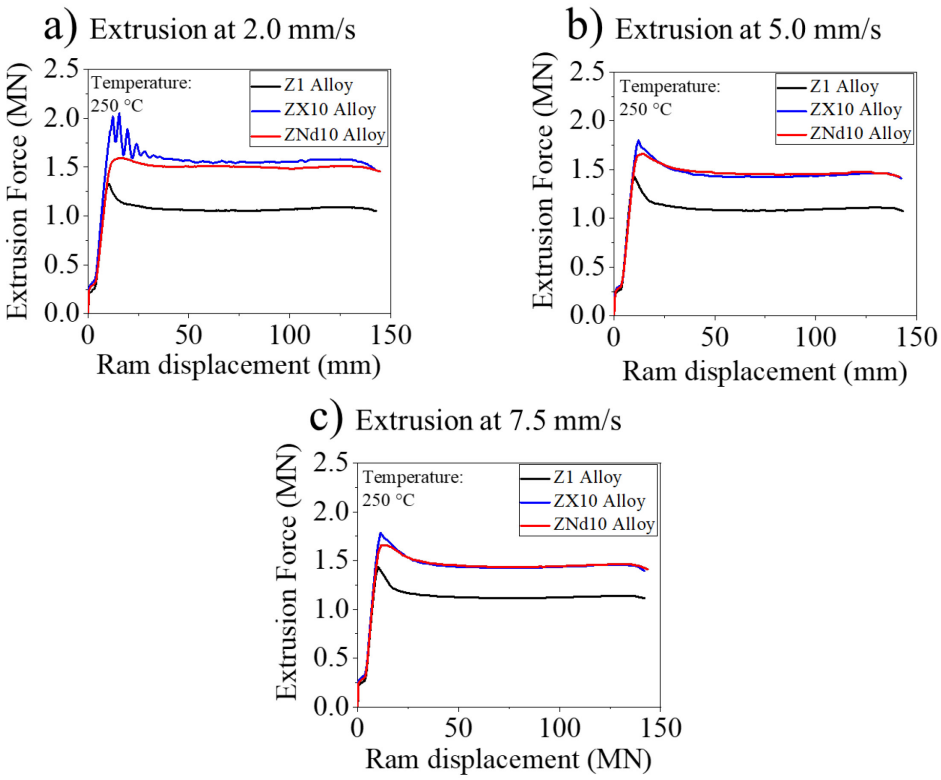

Figure 4.1. Extrusion force evolution as a function of ram displacement at 250 °C of processing temperature, a) 2.0 mm/s, b) 5.0 mm/s, and c) 7.5 mm/s.

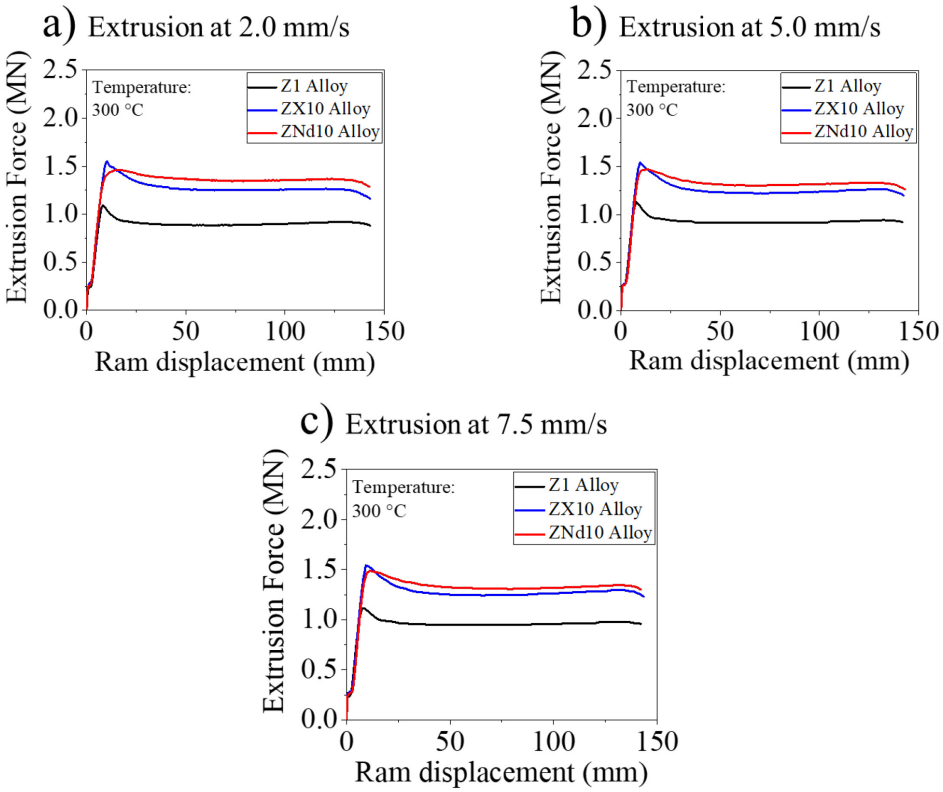

Figure 4.2. Extrusion force evolution as a function of ram displacement at 300 °C of processing temperature, a) 2.0 mm/s, b) 5.0 mm/s, and c) 7.5 mm/s.

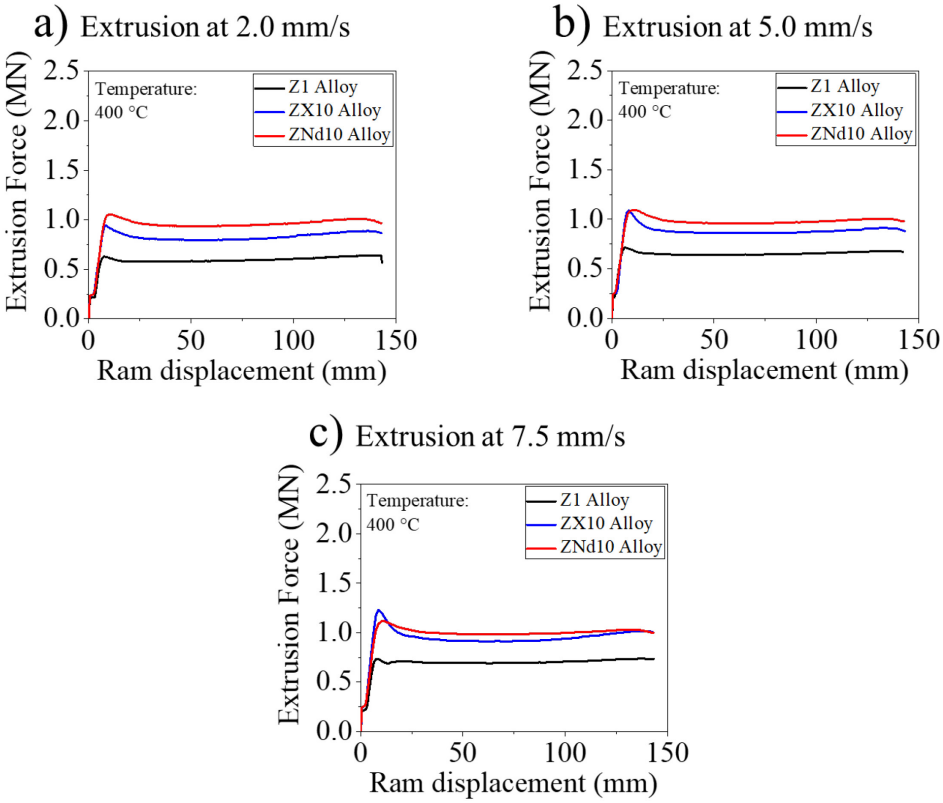

Figure 4.3. Extrusion force evolution as a function of ram displacement at 400 °C of processing temperature, a) 2.0 mm/s, b) 5.0 mm/s, and c) 7.5 mm/s.

Based on the applied extrusion parameters, figures 4.4 to 4.6 show the evolution of the surface appearance in each alloy during the extrusion processing.

Figure 4.4 displays the surface appearance on the Z1 alloy. From the figure, some lines or striations perpendicular to the extrusion direction (ED) are slightly visible. These perpendicular lines are more visible at the extrusion temperature of 400 °C at all the extrusion speeds, figure 4.4c. The extruded surfaces also show the presence of lines/scratches parallel to the ED. Clearly, these lines are visible at all the extrusion conditions.

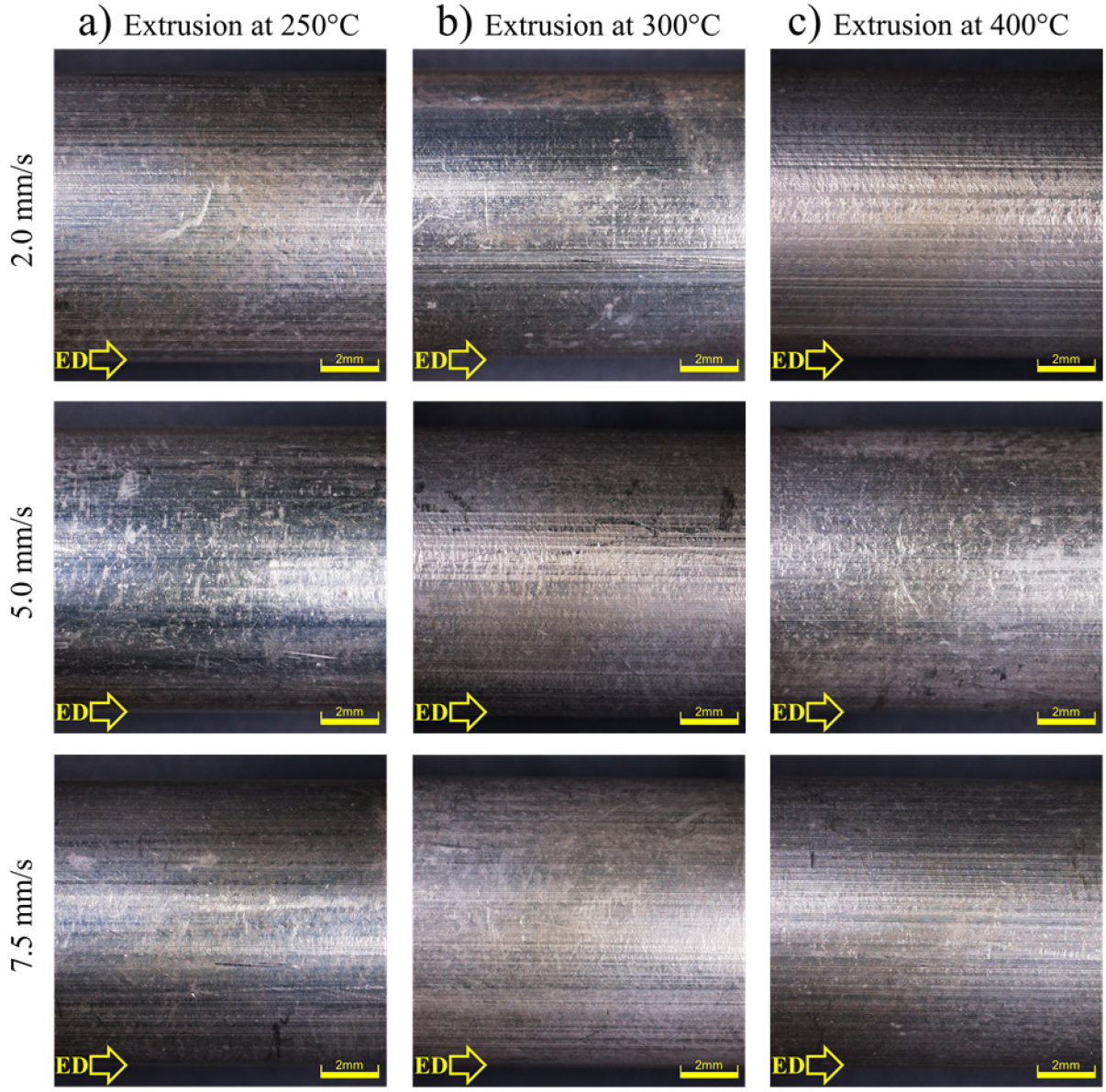

Figure 4.4. Pictures showing the surface of as-extruded alloy Z1 processed at different extrusion speeds and temperatures; a) 250 °C, b) 300 °C, and c) 400 °C. The extrusion speed increases from top to bottom. Yellow arrow indicates the extrusion direction (ED).

Figure 4.5 provides the surface appearance on the ZX10 alloy. As can be seen from the figure, the lines/striations perpendicular to the ED are also visible. As opposed to previous alloy, it seems that these perpendicular lines are present at all the extrusion conditions.

Similarly to previous alloy, the extruded surfaces also show the presence of lines/scratches parallel to the ED.

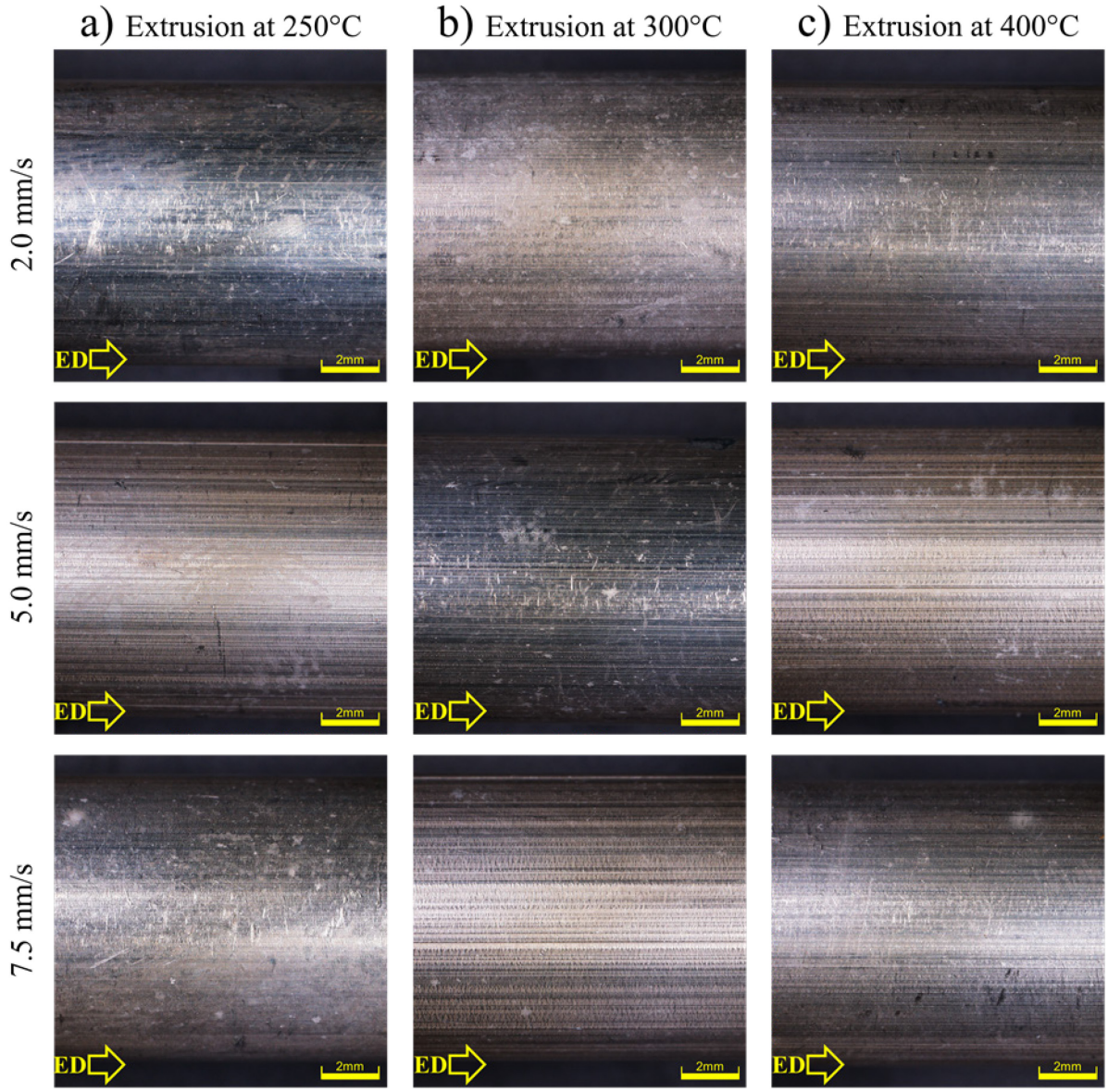

Figure 4.5. Pictures showing the surface of as-extruded alloy ZX10 processed at different extrusion speeds and temperatures; a) 250 °C, b) 300 °C, and c) 400 °C. The extrusion speed increases from top to bottom. Yellow arrow indicates the extrusion direction (ED).

Figure 4.6 presents the surface appearance on the ZNd10 alloy. As can be seen from the figure, there is no clear presence of lines/striations perpendicular to the ED. On the other hand, as in the previous alloys, the extruded surfaces of this ZNd10 alloy also show the presence of lines/scratches parallel to the ED.

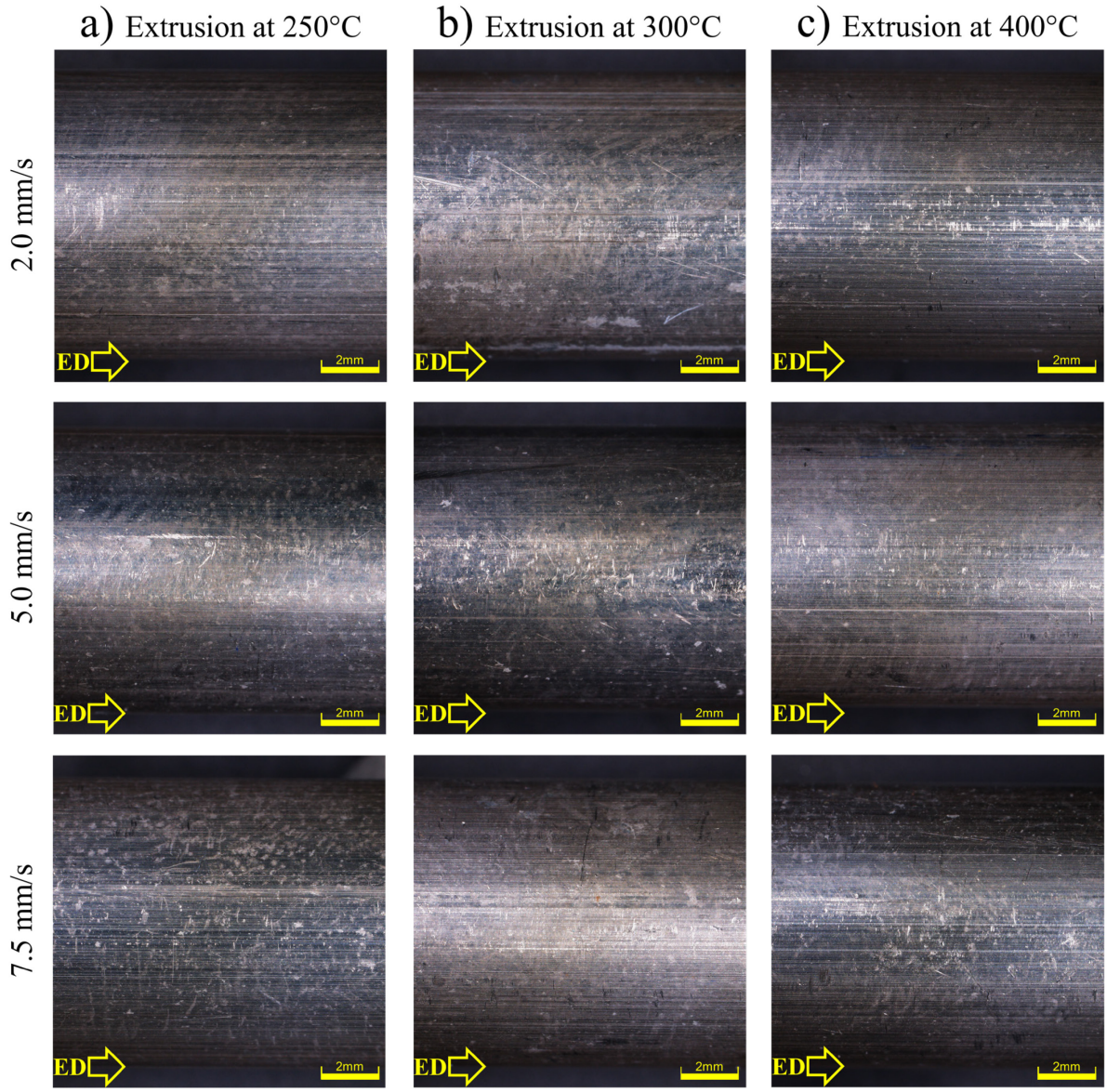

Figure 4.6. Pictures showing the surface of as-extruded alloy ZNd10 processed at different extrusion speeds and temperatures; a) 250 °C, b) 300 °C, and c) 400 °C. The extrusion speed increases from top to bottom. Yellow arrow indicates the extrusion direction (ED).

4.2 Microstructure evolution

4.2.1 Z1 alloy

Figure 4.7 shows the micrographs from longitudinal sections of the extruded bars, parallel to the extrusion direction. The average grain size (d) is shown as an inset in each picture. The microstructure evolution is organized as a function of processing temperature in such a way that the extrusion temperature increases from left to the right. It also shows the microstructure evolution in terms of the processing speed so that, the extrusion speed increases from up to down. The resulted microstructure exhibited completely recrystallized grains. It consists in homogeneous equiaxial coarse grains. It is observed that at each constant temperature, with the increase of extrusion speed there is a clear increase of the average grain size. It increases from 21.0 µm to 37.1 µm, as can be seen in figure 4.7a. On the other side, the figure 4.7b shows that

the average grain size increases from 21.3 µm to 44.5 µm. Furthermore, an increase of the average grain size from 35.2 µm to 51.4 µm at the extrusion temperature of 400 °C, see figure 4.7c. As shown also in figure 4.7, increasing the extrusion temperature while maintaining constant the extrusion speed, the same basic behavior is found in the average grain size evolution. It increases with the increase of extrusion temperature. The average grain size increases from 21.0 µm to 35.2 µm, from 34.7 µm to 42.9 µm and from 37.1 µm to 51.4 µm at the extrusion speeds of 2.0 mm/s, 5.0 mm/s and 7.5 mm/s, respectively.

Overall, the microstructure results shown in figure 4.7 indicate that the extrusion parameters applied to the alloy Z1 do not affect its recrystallization process. Clearly, the applied extrusion parameters only influence the average grain size.

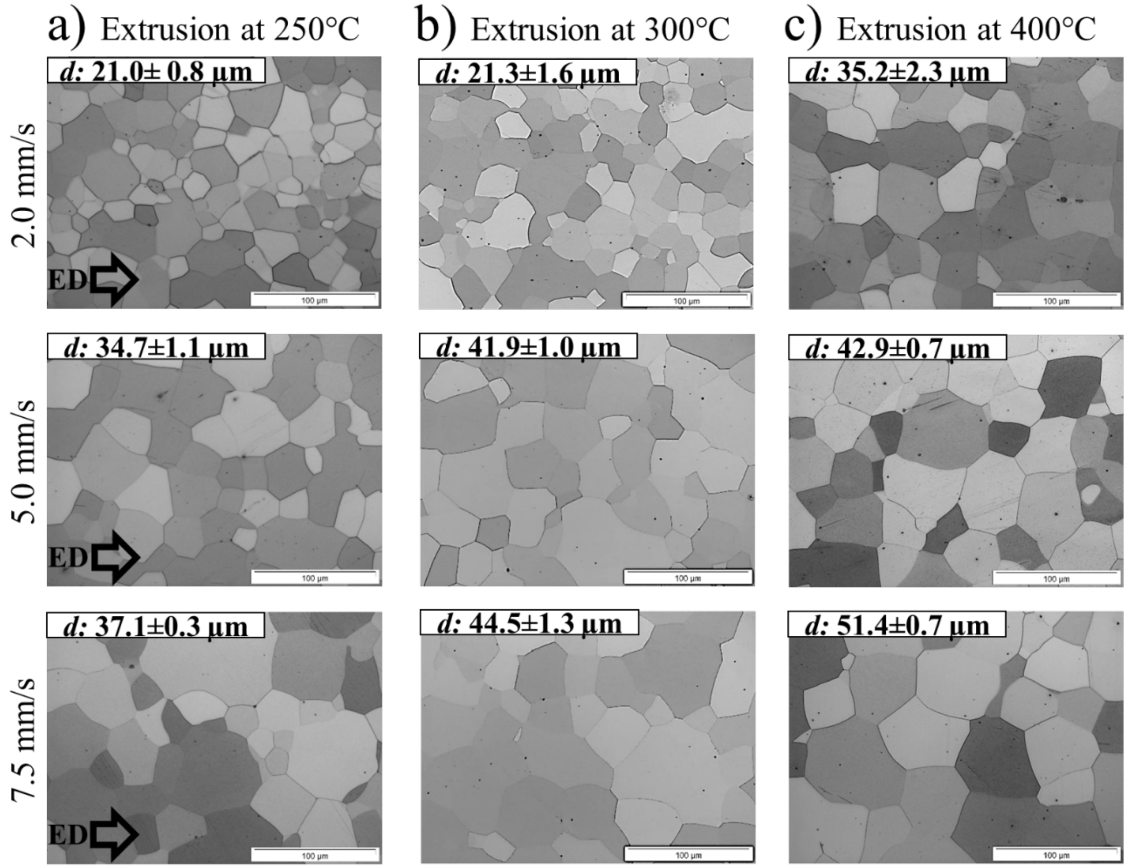

Figure 4.7. Microstructure evolution of the Z1 alloy extruded at a) 250 °C, b) 300 °C, and c) 400 °C. The inset (*d*) in each picture represents the average grain size. The extrusion speed increases from top to bottom. The black arrow indicates the extrusion direction (ED).

4.2.2 ZX10 alloy

Figure 4.8 provides the results on the microstructure evolution of the ZX10 alloy. The microstructure evolution is organized as in the previous alloy. The microstructure consists of homogeneous equiaxial grains. Clearly, the microstructure of this alloy is fully recrystallized at all the extrusion conditions. Then, the figure 4.8 suggests that this alloy developed a complete recrystallization process at the applied extrusion conditions in this work. It is observed that maintaining constant the extrusion temperature while modifying the extrusion speed, there is an increase of the grain size. There is a grain size increase from 9.5 µm to 18.5 µm at the extrusion temperature of 250 °C as can be seen in figure 4.8a. Meanwhile, at the

extrusion temperature of 300 °C (figure 4.8b), the grain size grows from 10.0 µm to 25.7 µm. At the highest extrusion temperature, i.e., 400 °C, the grain size increases from 25.1 µm to 34.0 µm, see figure 4.8c.
A similar finding is observed when the extrusion speed is constant, and the extrusion temperature varies. From the upper section of the figure 4.8, at 2.0 mm/s, the average grain size increases from 9.5 µm to 25.1 µm when increasing the extrusion temperature. An increase from 14.0 µm to 31.3 µm is observed when the alloy is extruded at 5.0 mm/s modifying the extrusion temperature, see the middle section of figure 4.8. At the bottom section of table 4.8, it is observed that when the alloy is extruded at constant speed of 7.5 mm/s, the average grain size increases from 18.5 µm to 34.0 µm.

In summary, the findings in this alloy relating to the grain size evolution is comparable to the one observed in the Z1 alloy, it increases either at the increment of extrusion speed or temperature. However, in comparison with the behavior of the Z1 alloy, the addition of Ca to the Mg-Zn system reduced the average grain size during the processing. That means, the Ca delayed the grain growth of the Mg-Zn alloy system.

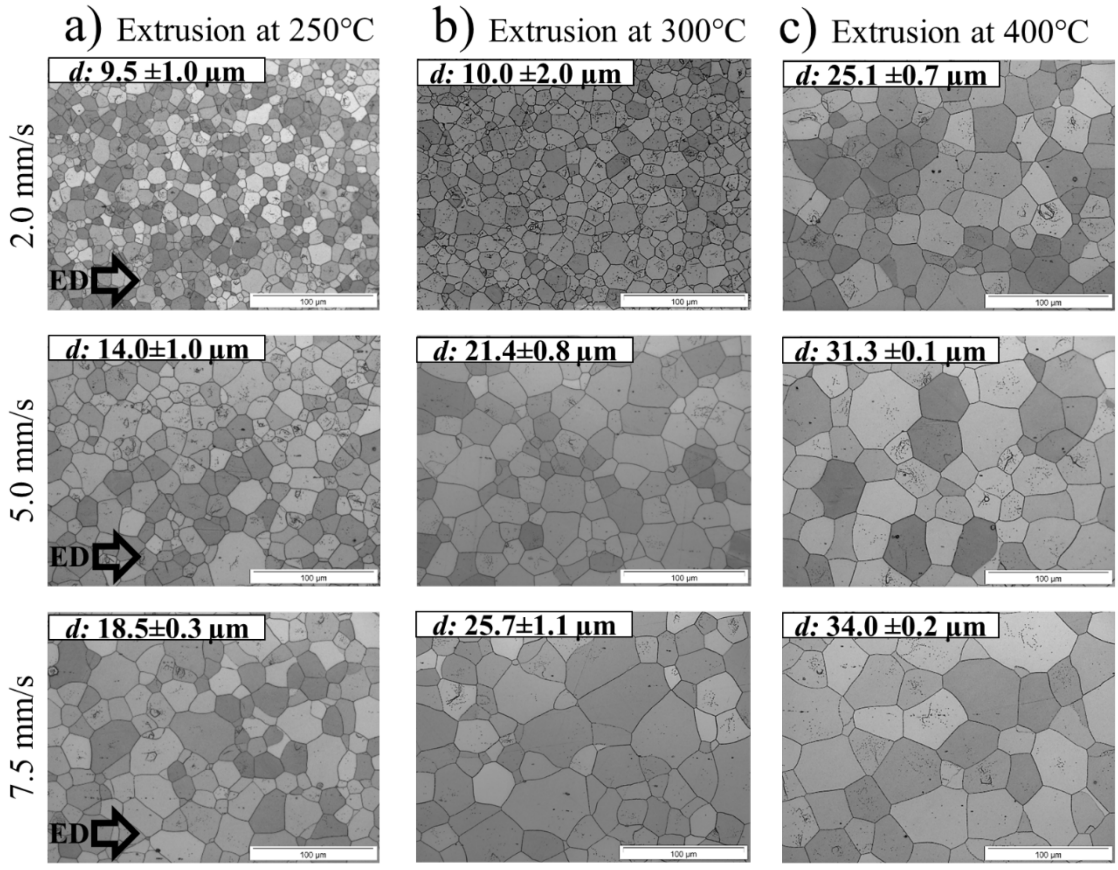

Figure 4.8. Microstructure evolution of the ZX10 alloy extruded at a) 250 °C, b) 300 °C, and c) 400 °C. The inset (*d*) in each picture represents the average grain size. The extrusion speed increases from top to bottom. The black arrow indicates the extrusion direction (ED).

4.2.3 ZNd10 alloy

Figure 4.9 displays the microstructure evolution in the ZNd10 alloy. The microstructure evolution in this alloy is different in comparison with the alloys previously observed.

This alloy shows a partly recrystallized microstructure which consists of large deform elongated grains parallel to the extrusion direction surrounded by small recrystallized grains, see figure 4.9a at 2.0 mm/s. Figure 4.9a also shows that the microstructure completely recrystallizes increasing the extrusion speed. The average grain size increases from 3.4 µm to 10.5 µm. Figure 4.9b depicts the microstructure evolution at 300 °C of extrusion temperature. However, even this extrusion temperature, the microstructure is not completely recrystallized. There are still some traces of non-recrystallized grains, see figure 4.9b at 2.0 mm/s. With increasing the extrusion speed, the microstructure is completely recrystallized. An increase of the average grain size from 4.5 µm to 16.1 µm is observed. After extrusion at 400 °C, the alloy shows a fully recrystallized microstructure, see figure 4.9c. At these extrusion conditions the average grain size increases from 13.8 µm to 26.5 µm.
The upper section of figure 4.9 shows the microstructure evolution of the alloy extruded at 2.0 mm/s increasing the extrusion temperature. As can be seen, the average grain size increases from 3.4 µm to 13.8 µm. The middle section of the figure 4.9 displays that at constant extrusion speed of 5.0 mm/s, the grain size increases from 8.4 µm to 22.4 µm. The bottom section of figure 4.9 shows the microstructure evolution at 7.5 mm/s of extrusion speed varying the extrusion temperature. The average grain size increases from 10.5 µm to 26.5 µm.

In summary, the microstructure evolution of the ZNd10 alloy shows a distinct behavior if compare with the alloys previously observed. The addition of Nd into the Mg-Zn system also delayed the recrystallization process. However, such a delay is more pronounced than with the Ca addition. This is revealed due to the presence of non-recrystallized grains as well as higher retardation of the grain growth.

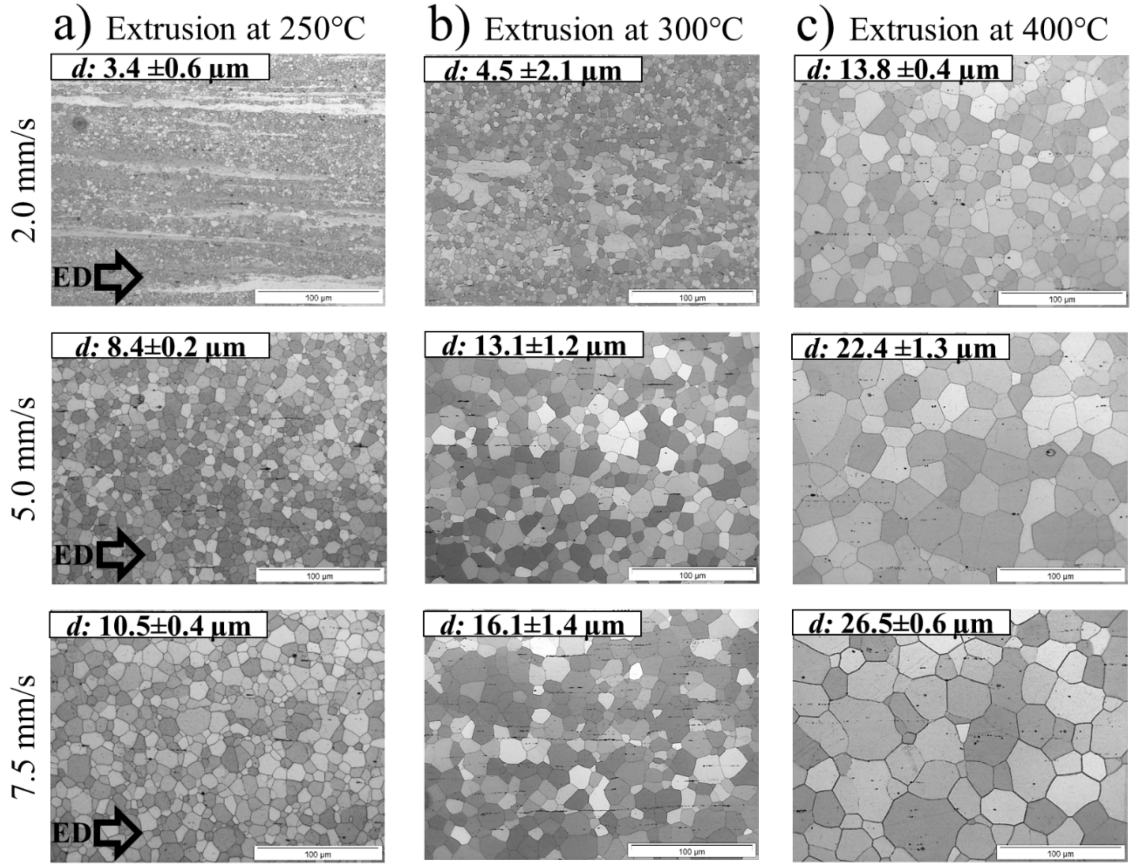

Figure 4.9. Microstructure evolution of the ZNd10 alloy extruded at a) 250 °C, b) 300 °C, and c) 400 °C. The inset (*d*) in each picture represents the average grain size. The extrusion speed increases from top to bottom. The black arrow indicates the extrusion direction (ED).

4.3 Crystallographic texture evolution

4.3.1 Z1 alloy

Figure 4.10 shows the crystallographic texture development of the Z1 alloy as a function of the applied extrusion processing parameters. The crystallographic texture is shown in the form of inverse pole figures in the extrusion direction. The texture intensity is in the unit of multiple of a random distribution (m.r.d).

As in traditional Mg alloys, the Z1 alloy shows a typical texture where the basal planes are aligned parallel to the extrusion direction. The preferential orientation of the grains is mainly distributed between the $< 10\bar{1}0 >$ and the $< 11\bar{2}0 >$ poles. As can be observed, there is a certain tendency of the grains to be preferably located at the $< 11\bar{2}0 >$ pole. This texture development is observed at all the extrusion conditions.

In summary, the results in figure 4.10 show that there is no significant influence of the applied extrusion parameters in the crystallographic texture evolution of this alloy.

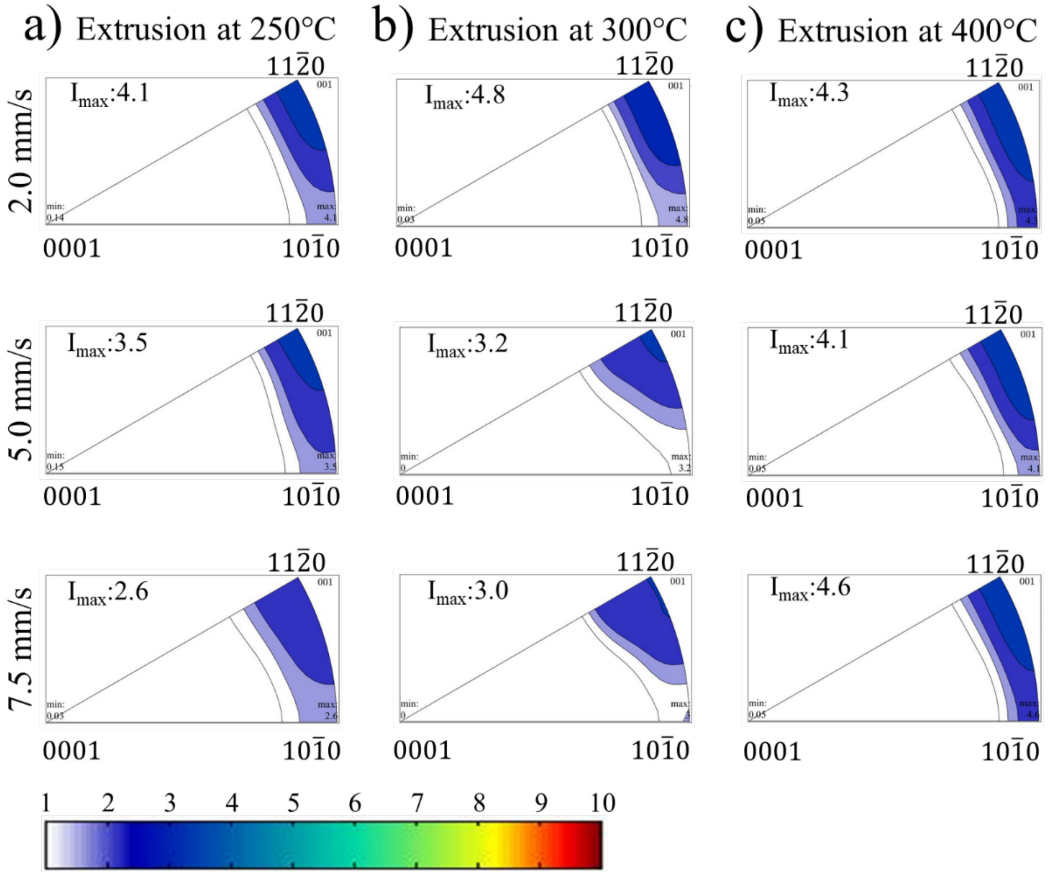

Figure 4.10. Inverse pole figures showing the crystallographic texture evolution of Z1 alloy extruded at a) 250°C, b) 300°C, and c) 400°C. Texture intensity is in m.r.d. The extrusion speed increases from top to bottom.

4.3.2 ZX10 alloy

Figure 4.11 illustrates the crystallographic texture evolution in the ZX10 alloy. As opposed to Z1 alloy, in this ZX10 alloy, a different crystallographic texture development is observed.
In figure 4.11a, the crystallographic texture evolution at a constant extrusion temperature of 250 °C varying the extrusion speed is shown. As can be seen, the texture is dominated mainly by the $< 10\bar{1}1 >$ pole. This crystallographic texture component remains with increasing the extrusion speed.

Furthermore to $< 10\bar{1}1 >$ pole, an additional component appears between the $< 0001 >$ and the $< 11\bar{2}0 >$ poles, i.e. the $< 11\bar{2}1 >$ pole at the extrusion of 300 °C, see figure 4.11b at 2.0 mm/s. With the following increase of extrusion speed, additionally to the $< 10\bar{1}1 >$ pole some orientations appear at the $< 11\bar{2}0 >$ pole.

In figure 4.11c, the crystallographic texture at the highest extrusion temperature, i.e., 400 °C, is shown. The most surprising aspect at this extrusion temperature is that the crystallographic texture evolved to a basal one at all the extrusion speeds. Clearly, the intensities are distributed between the $< 10\bar{1}0 >$ and the $< 11\bar{2}0 >$ poles.

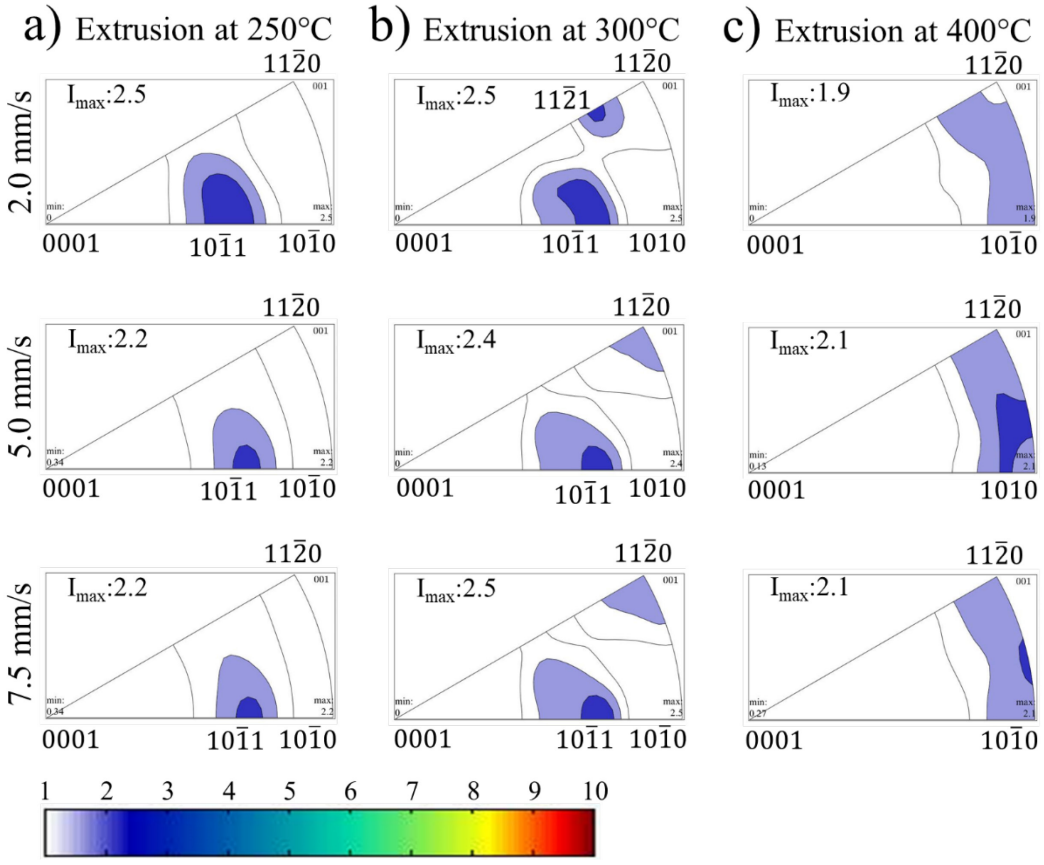

Figure 4.11. Inverse pole figures showing the crystallographic texture evolution of the ZX10 alloy extruded at a) 250°C, b) 300°C, and c) 400°C. Texture intensity is in m.r.d. The extrusion speed increases from top to bottom.

4.3.3 ZNd10 alloy

Figure 4.12 shows the crystallographic texture development on the ZNd10 alloy. In figure 4.12a the crystallographic texture evolution at the extrusion temperature of 250 °C in combination with the extrusion speed variation is shown. As can be seen, a fibre-type texture, which corresponds to the prismatic $< 10\bar{1}0 >$ pole is formed, here the prismatic planes are being mainly oriented perpendicular to the extrusion direction, figure 4.12a at 2.0 mm/s. As it is observed, the crystallographic texture consists of a strong prismatic texture. The $< 10\bar{1}0 >$ component is related with the presence of long elongated grains on the microstructure. Figure 4.12a also depicts that, in addition to the $< 10\bar{1}0 >$ component, the $< 11\bar{2}1 >$ pole is slightly visible. Increasing the extrusion speed, the crystallographic texture is weaker. The intensity of the single $< 10\bar{1}0 >$ component totally vanishes and the $< 11\bar{2}1 >$ pole dominates the texture. Figure 4.12b, shows the crystallographic texture development at 300 °C of extrusion temperature. The $< 10\bar{1}0 >$ component is still visible but its intensity decreases, figure 4.12b at 2.0 mm/s. Moreover, the $< 11\bar{2}1 >$ pole gains intensity and a further pole, i.e., the $< 20\bar{2}3 >$ pole develops between the $< 0001 >$ pole and the $< 10\bar{1}0 >$ pole. With a further increase of extrusion speed, the texture intensity decreases more. Then, an arc is formed between the poles $< 11\bar{2}1 >$ and $< 20\bar{2}3 >$ and dominates the crystallographic texture.

At the extrusion temperature of 400 °C, the $< 11\bar{2}1 >$ pole is established and dominates the texture at 2.0 mm/s and 5.0 mm/s, see figure 4.12c. With the further increase of extrusion speed, the arc is formed between the poles $< 11\bar{2}1 >$ and $< 20\bar{2}3 >$.

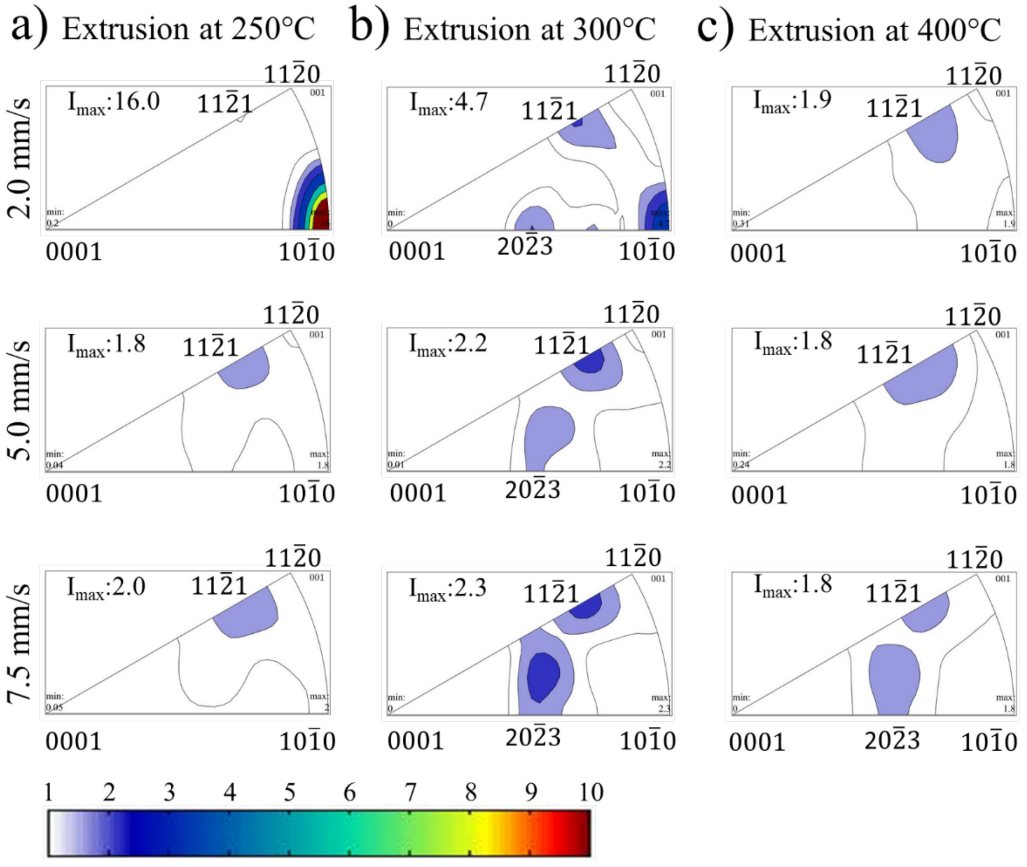

Figure 4.12. Inverse pole figures showing the crystallographic texture evolution of the ZNd10 alloy extruded at a) 250°C, b) 300°C, and c) 400°C. Texture intensity is in m.r.d. The extrusion speed increases from top to bottom.

4.4 Mechanical properties

4.4.1 Z1 alloy

Figure 4.13 shows the stress-strain curves of the alloy tested in tension and in compression. The graphs on the left side correspond to the tension tests while the graphs on the right side correspond to the compression tests.

At the extrusion temperature of 250 °C and varying the extrusion speed, the figure 4.13a displays that the tensile yield stress (TYS) of the alloy decreases with the increment of extrusion speed. Furthermore, the ultimate tensile stress (UTS) is higher at 2.0 mm/s, while it is quite comparable at 5.0 and 7.5 mm/s. A reduction of the fracture strain is observed with the increment of the extrusion speed. On the other hand, in compression (right side in figure 4.13a) the characteristic sigmoidal hardening (S-shape) is visible when a material is tested in compression. The stress-strain curves show a reduction of the compressive yield stress (CYS) with the increment of extrusion speed. As can be seen, the ultimate compressive stress (UCS) and the fraction strain are comparable at all the extrusion speeds.

Figure 4.13b shows the stress-strain curves of the alloy at the extrusion temperature of 300 °C. The TYS is higher at 2.0 mm/s but comparable at 5.0 and 7.5 mm/s. The UTS and fracture strain both decrease with the increment of the extrusion speed. A similar trend is observed in the material tested in compression. Clearly, there is a reduction of the CYS and UCS as the extrusion speed increases. The lowest fracture strain is observed in the material extruded at 2.0 mm/s.

In figure 4.13c the stress-strain curves of the alloy extruded at 400 °C are presented. The lowest TYS and UTS are observed at 7.5 mm/s. The fracture strain is slightly reduced with the increment of extrusion speed from 2.0 mm/s to 5.0 mm/s. The highest reduction is observed at the highest extrusion speed. Finally, in compression, with the increase of extrusion speed from 2.0 mm/s to 5.0 mm/s, the CYS is reduced, then, it increases with the further increase of the extrusion speed. The UCS shows a slight increase. The fracture strain is reduced as the extrusion speed increases.

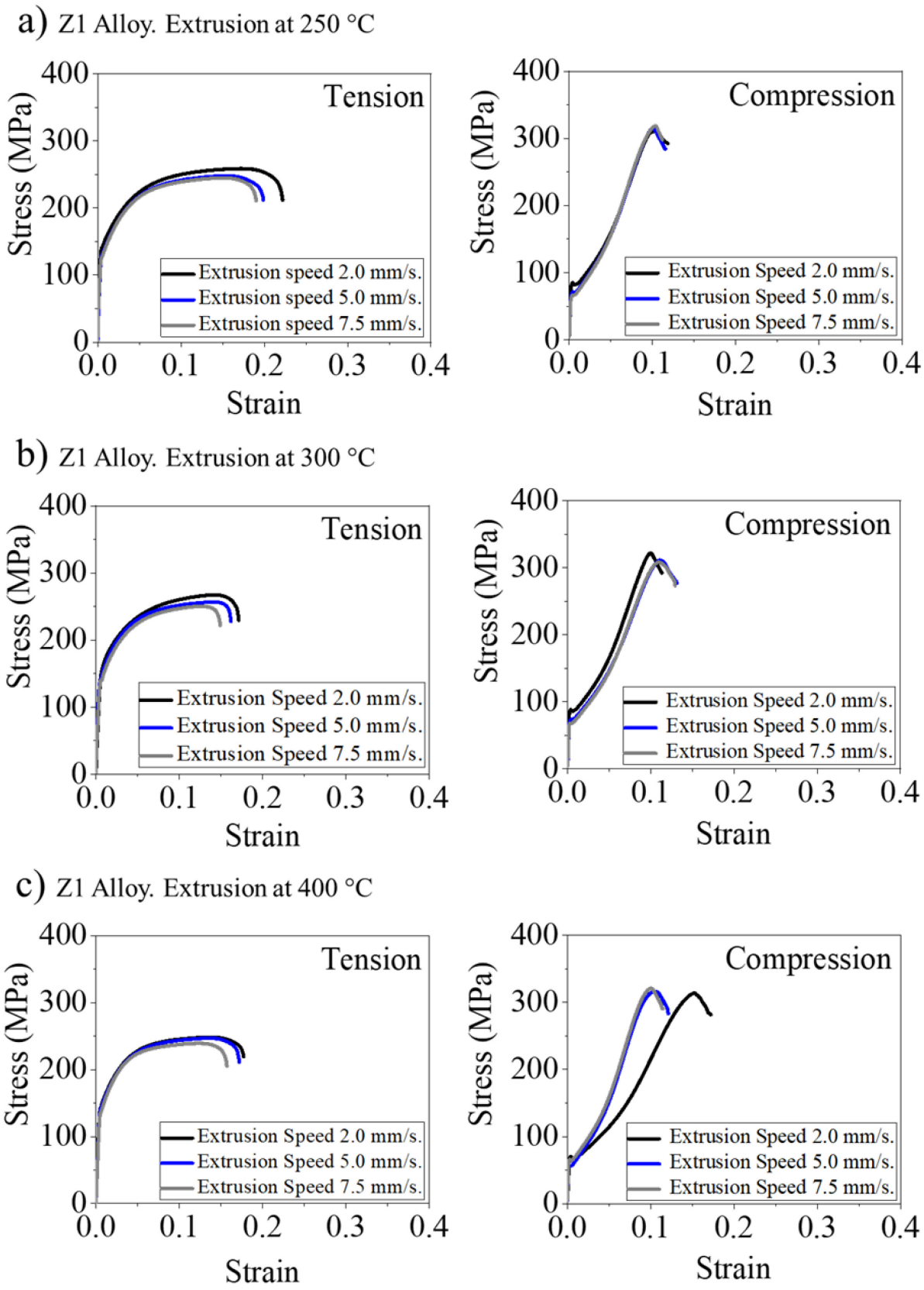

Figure 4.13. Tension and compression stress-strain curves of Z1 alloy extruded at a) 250 °C, b) 300 °C, and c) 400 °C. Tested at room temperature.

In table 4.1, the mechanical properties of the Z1 alloy are summarized.

Table 4.1. Tension and compression properties of the Z1 alloy measured parallel to the extrusion direction.

Extrusion temperature (°C)	Extrusion speed (mm/s)	TYS (MPa)	UTS (MPa)	Fracture strain	CYS (MPa)	UCS (MPa)	Fracture strain
250	2.0	141.0±1.1	254.0±0.1	0.22±0.01	84.1±1.1	312.0±2.1	0.12±0.01
	5.0	130.0±0.6	245.0±0.2	0.19±0.01	71.0±0.1	316.0±3.0	0.11±0.01
	7.5	127.0±0.5	241.0±1.0	0.18±0.01	67.0±0.5	318.0±1.0	0.11±0.01
300	2.0	151.0±1.0	261.1±1.0	0.17±0.01	88.0±0.2	322.3±1.0	0.11±0.01
	5.0	141.0±2.0	251.0±0.1	0.15±0.01	74.0±0.3	311.0±1.0	0.13±0.01
	7.5	140.0±1.0	246.0±4.0	0.17±0.01	68.0±0.1	307.0±2.0	0.13±0.01
400	2.0	145.0±1.0	244.0±1.0	0.16±0.01	71.0±0.3	330.0±1.0	0.12±0.01
	5.0	142.0±0.5	241.0±1.0	0.15±0.01	58.0±0.1	316.0±0.5	0.12±0.01
	7.5	135.5±0.5	238.0±1.5	0.16±0.01	66.0±0.5	323.0±2.0	0.12±0.01

Tensile and compressive properties of the extruded alloy Z1 as a function of extrusion speed are shown in figure 4.14. Figure 4.14a suggests that after extrusion at 250 °C, the TYS reduces approximately 11.0 MPa from 2.0 mm/s to 5.0 mm/s of extrusion. With the further increase of extrusion speed, from 5.0 to 7.5 mm/s, there is still a reduction of 3.0 MPa. The UTS also decreases; 9.0 MPa from 2.0 mm/s to 5.0 mm/s and 4.0 MPa from 5.0 mm/s to 7.5 mm/s. The fracture strain decreases a total amount of 0.04, where the maximum reduction (0.03) is observed from 2.0 mm/s to 5.0 mm/s. The CYS decreases 13.0 MPa and 4.0 MPa when the alloy is extruded from 2.0 mm/s to 5.0 mm/s and from 5.0 mm/s to 7.5 mm/s, respectively. However, the UCS increases a total amount of 6.0 MPa, where the highest increase, i.e. 4.0 MPa is observed from 2.0 mm/s to 5.0 mm/s. The fracture strain does not show significant changes.

From figure 4.14b, at extrusion temperature of 300 °C, the TYS reduces 10.0 MPa (2.0 mm/s to 5.0 mm/s). With the further increase of extrusion speed to 7.5 mm/s, there is only a reduction of 1.0 MPa. The UTS decreases 10.0 MPa (2.0 mm/s to 5.0 mm/s) and 5.0 MPa (5.0 mm/s to 7.5 mm/s). The fracture strain first decreases 0.02 (2.0 mm/s to 5.0 mm/s), then increases. On the other hand, the CYS decreases 14.0 MPa (2.0 mm/s to 5.0 mm/s) and 6.0 MPa (5.0 mm/s to 7.5 mm/s). The UCS decreases a total amount of 15.0 MPa, i.e., 11.0 MPa from 2.0 mm/s to 5.0 mm/s and 4.0 MPa from 5.0 mm/s to 7.5 mm/s. The fracture strain increases 0.02.

Figure 4.14c shows the mechanical properties at extrusion temperature of 400 °C. First, the TYS reduces 3.0 MPa (2.0 mm/s to 5.0 mm/s) and 7.0 MPa (5.0 mm/s to 7.5). Secondly, the UTS is reduced 3.0 MPa at each extrusion speed increment. The fracture strain is quite comparable. The CYS decreases 13.0 MPa (2.0 mm/s to 5.0 mm/s) but increases 8.0 MPa (5.0 mm/s to 7.5 mm/s). A similar tendency is observed in the UCS; it decreases 14.0 MPa (2.0 mm/s to 5.0 mm/s) but increases 7.0 MPa (5.0 mm/s to 7.5). The fracture strain is practically the same.

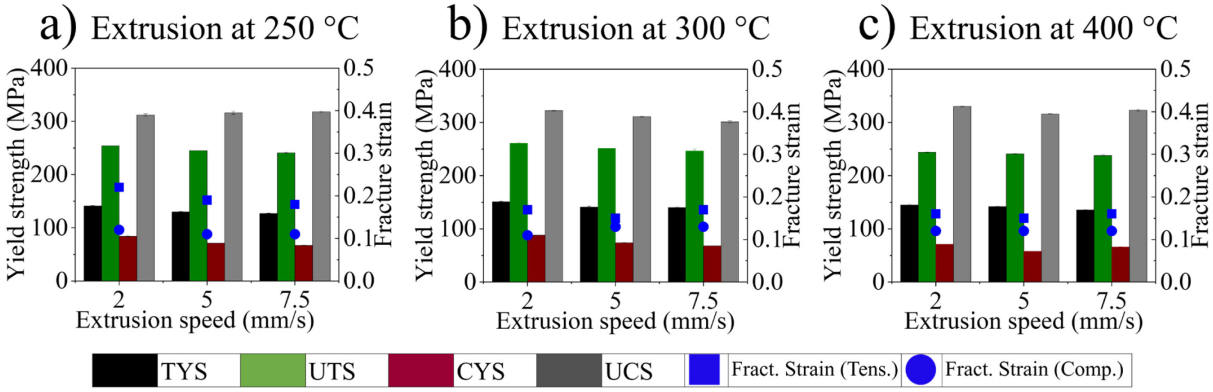

Figure 4.14. Mechanical properties of Z1 alloy at different extrusion speeds and temperature; a) 250 °C, b) 300 °C, c) 400 °C.

4.4.2 ZX10 alloy

The stress-strain curves obtained from the tension and compression tests of ZX10 alloy are shown in figure 4.15.

The stress-strain curves of the alloy at the extrusion temperature of 250 °C are shown in figure 4.15a. The TYS of ZX10 alloy decreases with the increment of extrusion speed. Furthermore, the highest UTS is observed at 2.0 mm/s, while at 5.0 and 7.5 mm/s it is comparable. The fracture strain is comparable at each extrusion speed.
In compression, the CYS is highest at 2.0 mm/s. It seems that at 5.0 mm/s and 7.5 mm/s the CYS is similar. The UCS follows a similar tendency with the increment of extrusion speed. As can be seen, the fraction strain is quite comparable at all the extrusion speeds.

In figure 4.15b the stress-strain curves at the extrusion temperature of 300 °C is shown. As can be seen, the TYS decreases with the increment of extrusion speed. The highest TYS corresponds to the material extruded at 2.0 mm/s; at 5.0 mm/s and 7.5 mm/s such feature is comparable. The UTS behaves similarly to TYS with the increment of extrusion speed. It seems that the fracture strain is quite comparable at all the extrusion speeds. On the other hand, the highest UCS corresponds to the material extruded at 2.0 mm/s. This property is reduced at the extrusion speed of 5.0 mm/s and is maintained at 7.5 mm/s. In reference to the fracture strain, it seems that is kept constant with the increment of extrusion speed.

The stress-strain curves at the extrusion temperature of 400 °C are displayed in figure 4.15c. It seems that increasing the extrusion speed, the TYS and the UTS are quite comparable. The lowest fracture strain is observed on the alloy extruded at 2.0 mm/s. Then, it slightly increased with increasing the extrusion speed. In compression, it seems that the CYS is slightly higher at 2.0 mm/s of extrusion speed. At 5.0 mm/s and 7.5 mm/s the CYS is quite comparable. Clearly, the highest UCS corresponds to the alloy extruded at 2.0 mm/s. This property is reduced with the further increment of the extrusion speed at 5.0 mm/s. Then, it is conserved at 7.5 mm/s. The lowest fracture strain is observed at 2.0 mm/s of extrusion speed and increases with the increment of extrusion speed.

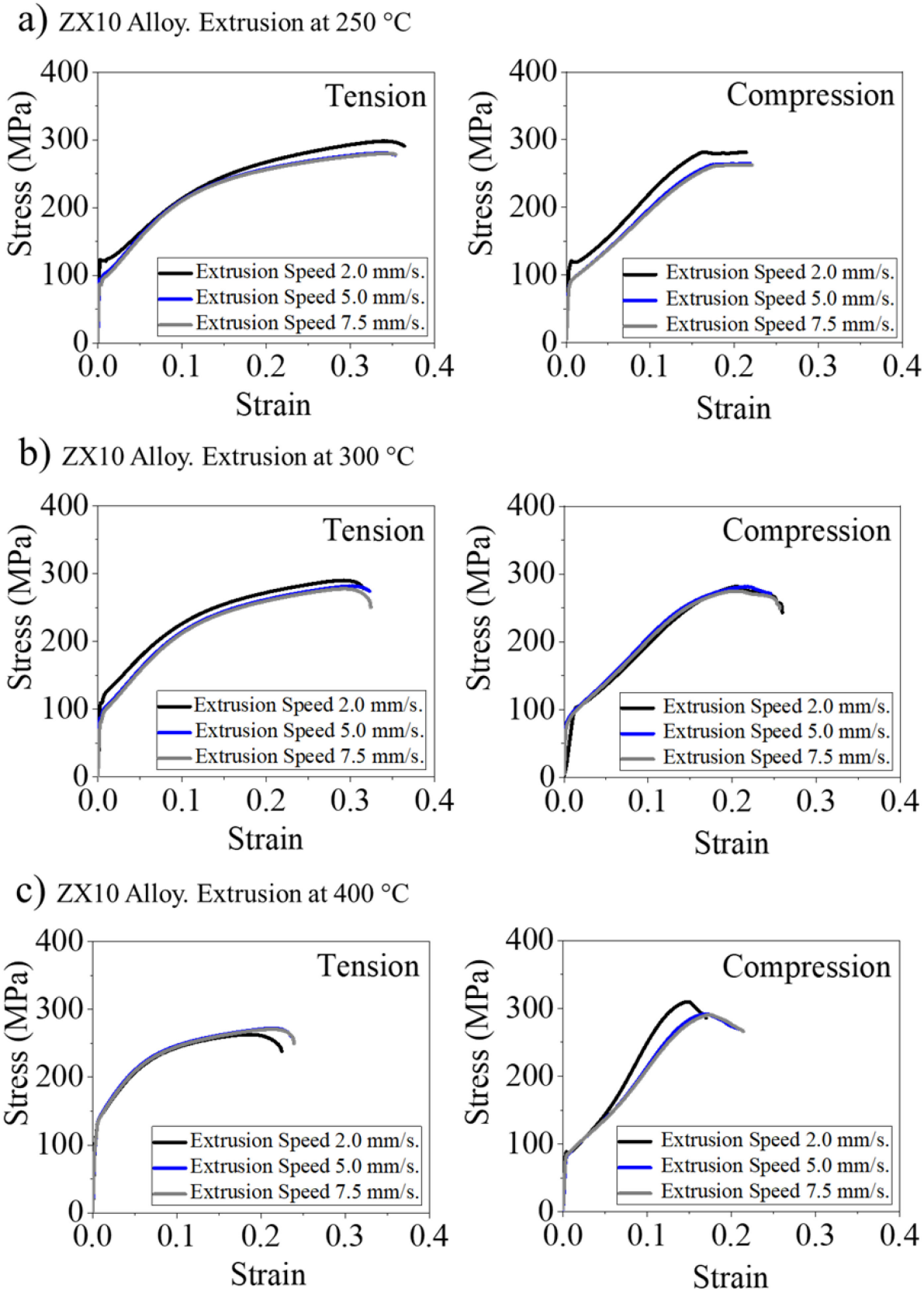

Figure 4.15. Tension and compression stress-strain curves of ZX10 alloy extruded at a) 250 °C, b) 300 °C, and c) 400 °C. Tested at room temperature.

The mechanical properties of this ZX10 alloy are summarized in table 4.2.

Table 4.2. Tension and compression properties of the ZX10 alloy measured parallel to the extrusion direction.

Extrusion temperature (°C)	Extrusion speed (mm/s)	TYS (MPa)	UTS (MPa)	Fracture strain	CYS (MPa)	UCS (MPa)	Fracture strain
250	2.0	124.0±1.0	276.0±3.0	0.37±0.01	121.0±0.3	284.0±3.0	0.27±0.01
	5.0	94.0±1.0	265.5±0.2	0.36±0.01	92.0±0.5	262.0±1.0	0.27±0.01
	7.5	87.0±1.0	258.0±1.0	0.36±0.01	86.0±0.1	269.0±1.0	0.26±0.03
300	2.0	109.0±1.0	272.0±0.5	0.32±0.02	106.0±1.0	277.0±4.0	0.24±0.01
	5.0	89.0±0.2	256.5±0.2	0.32±0.01	88.0±0.3	266.0±0.5	0.23±0.01
	7.5	83.0±2.0	256.0±0.5	0.31±0.01	84.0±1.0	277.0±3.5	0.25±0.01
400	2.0	140.1±1.0	254.0±1.0	0.23±0.01	89.0±0.2	308.0±2.0	0.17±0.01
	5.0	136.5±1.0	264.0±1.5	0.23±0.01	87.0±0.5	292.0±1.0	0.21±0.01
	7.5	138.0±1.0	262.0±0.5	0.23±0.01	87.0±0.2	292.0±2.0	0.21±0.01

Tensile and compressive properties of the extruded ZX10 alloy are presented in figure 4.16. Figure 4.16a depicts that after extrusion at 250 °C while the extrusion speed varies, the TYS reduces 30.0 MPa (2.0 mm/s to 5.0 mm/s). With the further increase of extrusion speed, the TYS decreases 7.0 MPa (5.0 to 7.5 mm/s). The UTS also decreases; 10.5 MPa (2.0 mm/s to 5.0 mm/s) and 7.5 MPa (5.0 mm/s to 7.5 mm/s). The fracture strain decreases 0.01 (2.0 mm/s to 5.0 mm/s) and it is maintained with the further increases of extrusion speed. A reduction is also observed, approximately 29.0 MPa and 6.0 MPa when the alloy is extruded from 2.0 mm/s to 5.0 mm/s and from 5.0 mm/s to 7.5 mm/s, respectively. The UCS decreases 22.0 MPa (2.0 mm/s to 5.0 mm/s) but increases 7.0 MPa (5.0 mm/s to 7.5 mm/s). The fracture strain is similar at 2.0 mm/s and 5.0 mm/s but decreases 0.01 from 5.0 mm/s to 7.5 mm/s.

Figure 4.16b displays that at the extrusion temperature of 300 °C; the TYS reduces 26.0 MPa in total, i.e. 20.0 MPa (2.0 mm/s to 5.0 mm/s) and 6.0 MPa (5.0 mm/s to 7.5 mm/s). The UTS decreases 15.5 MPa (2.0 mm/s to 5.0 mm/s) and only 0.5 MPa (5.0 mm/s to 7.5 mm/s). The fracture strain decreases only 0.01 at the highest extrusion speed. On the other hand, the CYS decreases 18.0 MPa (2.0 mm/s to 5.0 mm/s) and 4.0 MPa (5.0 mm/s to 7.5 mm/s). The UCS decreases 11.0 MPa (2.0 mm/s to 5.0 mm/s) but increases also 11.0 MPa (5.0 mm/s to 7.5 mm/s). The fracture strain decreases 0.01 (2.0 mm/s to 5.0 mm/s) but increases 0.02 (5.0 mm/s to 7.5 mm/s).

Figure 4.16c shows the mechanical properties at the constant extrusion temperature of 400 °C. Clearly, the TYS is higher at these extrusion conditions if compared with the previously observed ones. However, it is also modified as an effect of the extrusion speed variation. First, the TYS reduces 3.6 MPa (2.0 mm/s to 5.0 mm/s), then increases 1.5 MPa (5.0 mm/s to 7.5). The UTS increases 10.0 MPa (2.0 mm/s to 5.0 mm/s) but decreases 2.0 MPa (5.0 mm/s to 7.5). The fracture strain is practically the same at all extrusion speeds. The CYS decreases 2.0 MPa (2.0 mm/s to 5.0 mm/s), then it is maintained from 5.0 mm/s to 7.5 mm/s. A similar trend is observed in the UCS; it decreases 16.0 MPa (2.0 mm/s to 5.0 mm/s), then is maintained from 5.0 mm/s to 7.5 mm/s. The fracture strain increases 0.04 from 2.0 mm/s to 5.0 mm/s and preserved at the highest extrusion speed.

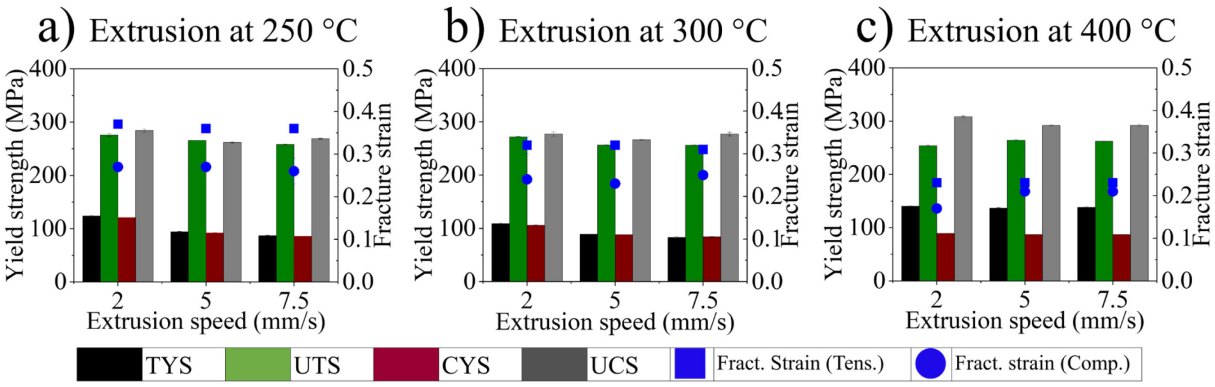

Figure 4.16. Mechanical properties of ZX10 alloy at different extrusion speeds and temperature; a) 250 °C, b) 300 °C, c) 400 °C.

4.4.3 ZNd10 alloy

Figure 4.17 displays the stress strain curves in tension and in compression of the alloy ZNd10.

Figure 4.17a shows the stress-strain curves at the extrusion temperature of 250 °C. As it is observed, the TYS shows a significant reduction from 2.0 mm/s to 5.0 mm/s of extrusion speed. The TYS still decreases with the increase of extrusion speed at 7.5 mm/s. The UTS follows a similar trend as the extrusion speed increases. Clearly, the fracture strain increases as the extrusion speed increases. The higher fracture strain increment is observed when the alloy is extruded at 5.0 mm/s. In compression, the alloy has the characteristic sigmoidal shape when is tested. Such a characteristic is maintained at the three extrusion speeds. The increment of the extrusion speed represented a reduction of the CYS as well as the UCS. The compression fracture strain is increased as the extrusion speed increases.

The stress-strain curves of the alloy extruded at 300 °C are illustrated in figure 4.17b. As can be seen from the graph, the TYS decreases as the extrusion speed increases. The highest reduction is observed from 2.0 mm/s to 5.0 mm/s of extrusion speed and still some reduction is observed at 7.5 mm/s. The fracture strain is increased with the increment of the extrusion speed. The highest corresponds to 5.0 mm/s and 7.5 mm/s extrusion speeds. In compression, the CYS also shows a reduction as the extrusion speed increases. The UCS follows a different trend, first decreases (2.0 mm/s to 5.0 mm/s) and then increases with the further extrusion speed increment. The fracture strain is quite comparable at all the extrusion speeds.

Figure 4.17c presents the stress-strain curves of the alloy extruded at 400 °C. A reduction in the TYS is observed while the UTS first decreases and then increases with the increase of the extrusion speed. It is observed that the highest fracture strain corresponds to the alloy extruded at 7.5 mm/s. As can be seen, the increment of the extrusion speed reduces the CYS. In reference to the UCS, it shows first a decrease and then an increase as an effect of the extrusion speed increment. It seems that the fracture strain decreases as the extrusion speed increases.

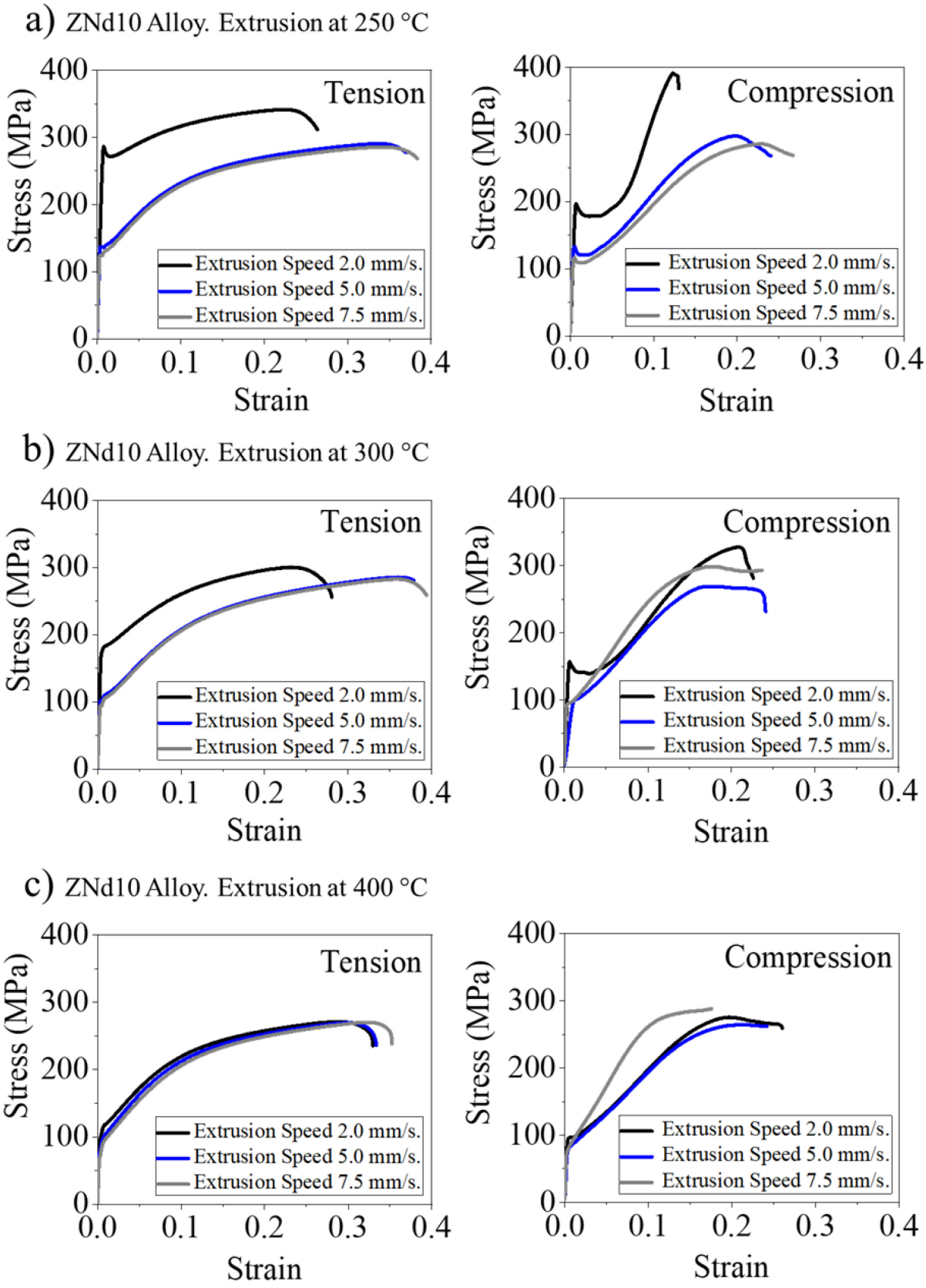

Figure 4.17. Tension and compression stress-strain curves of ZNd10 alloy extruded at a) 250 °C, b) 300 °C, and c) 400 °C. Tested at room temperature.

Table 4.3 summarizes the mechanical properties of the ZNd10 alloy.

Table 4.3. Tension and compression properties of the ZNd10 alloy measured parallel to the extrusion direction.

Extrusion temperature (°C)	Extrusion speed (mm/s)	TYS (MPa)	UTS (MPa)	Fracture strain	CYS (MPa)	UCS (MPa)	Fracture strain
250 °C	2.0	286.0±1.0	333.0±1.0	0.27±0.01	196.0±0.5	395.0±5.0	0.13±0.01
	5.0	137.0±1.0	273.0±1.0	0.38±0.01	133.0±0.1	296.0±2.5	0.24±0.01
	7.5	124.0±0.5	267.0±1.0	0.39±0.01	116.0±1.0	283.0±2.0	0.28±0.01
300 °C	2.0	183.0±7.0	282.0±3.0	0.28±0.03	157.0±0.5	317.0±1.0	0.23±0.01
	5.0	101.0±2.0	262.0±2.0	0.40±0.02	101.0±1.0	268.0±1.0	0.23±0.01
	7.5	94.5±0.5	261.0±0.5	0.37±0.01	95.0±0.1	299.0±1.0	0.22±0.01
400 °C	2.0	117.5±0.1	256.0±1.0	0.34±0.01	98.0±0.5	277.0±2.0	0.27±0.01
	5.0	100.0±0.1	249.0±1.0	0.34±0.01	83.0±0.1	264.0±0.5	0.22±0.01
	7.5	91.5±1.0	253.5±1.0	0.34±0.02	86.5±0.2	282.0±1.0	0.18±0.01

Figure 4.18 displays the tension and compression properties of ZNd10 alloy. Figure 4.18a shows the mechanical properties after extrusion at 250 °C. It can be observed that the TYS reduces by 149.0 MPa (2.0 mm/s to 5.0 mm/s). With the further increase of extrusion speed, the TYS decreases by 13.0 MPa (5.0 to 7.5 mm/s). The UTS also decreases; 60.0 MPa (2.0 mm/s to 5.0 mm/s) and 6.0 MPa (5.0 mm/s to 7.5 mm/s). The fracture strain increases, first 0.11 (2.0 mm/s to 5.0 mm/s) and then 0.01 (5.0 mm/s to 7.5 mm/s). The CYS decreases 63.0 MPa (2.0 mm/s to 5.0 mm/s) and then 17.0 MPa (5.0 mm/s to 7.5 mm/s). In reference to the UCS, it decreases 99. MPa (2.0 mm/s to 5.0 mm/s) and 13.0 MPa (5.0 mm/s to 7.5 mm/s). The fracture strain increases 0.11 (2.0 mm/s to 5.0 mm/s) and then 0.04 (5.0 mm/s to 7.5 mm/s).

Figure 4.18b shows that at the extrusion temperature of 300 °C, the TYS reduces 82.0 MPa (2.0 mm/s to 5.0 mm/s) and 6.5 MPa (5.0 mm/s to 7.5 mm/s). As can be seen, the UTS decreases 20.0 MPa (2.0 mm/s to 5.0 mm/s) and only 1.0 MPa (5.0 mm/s to 7.5 mm/s). The fracture strain increases 0.12 (2.0 mm/s to 5.0 mm/s) and decreases 0.03 (5.0 mm/s to 7.5 mm/s). On the other hand, the CYS decreases 56.0 MPa (2.0 mm/s to 5.0 mm/s) and 6.0 MPa (5.0 mm/s to 7.5 mm/s). The UCS decreases 49.0 MPa (2.0 mm/s to 5.0 mm/s) but increases 31.0 MPa (5.0 mm/s to 7.5 mm/s). At the highest extrusion speed, the fracture strain decreases 0.01.

Figure 4.18c exhibits the mechanical properties at extrusion temperature of 400 °C. Clearly, the TYS reduces 17.5 MPa (2.0 mm/s to 5.0 mm/s), then 8.5 MPa (5.0 mm/s to 7.5). The UTS decreases 7.0 MPa (2.0 mm/s to 5.0 mm/s) but increases 4.5 MPa (5.0 mm/s to 7.5). The fracture strain is practically the same at all extrusion speeds. The CYS decreases 15.0 MPa (2.0 mm/s to 5.0 mm/s), then increases 3.5 MPa from 5.0 mm/s to 7.5 mm/s. As can be seen, the UCS decreases 13.0 MPa (2.0 mm/s to 5.0 mm/s), then is increases 18.0 MPa from 5.0 mm/s to 7.5 mm/s. The fracture strain decreases 0.05 from 2.0 mm/s to 5.0 mm/s and 0.04 from 5.0 mm/s to 7.5 mm/s.

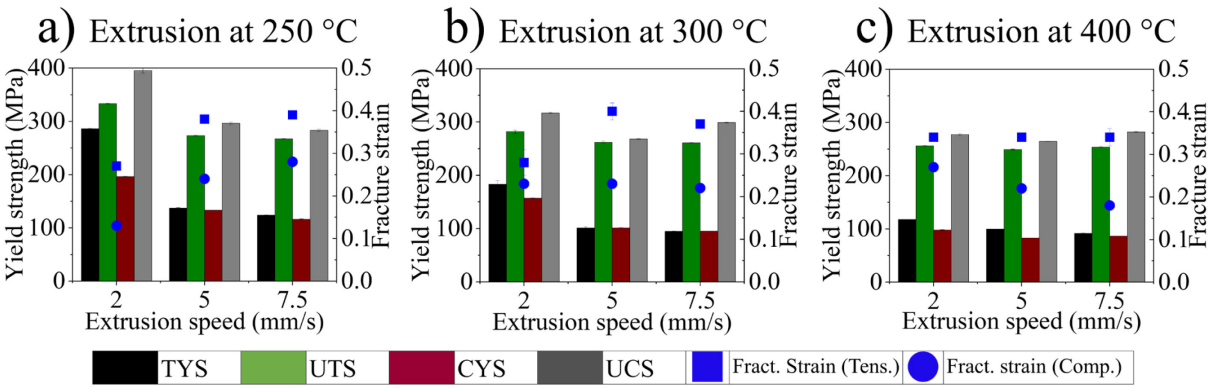

Figure 4.18. Mechanical properties of ZNd10 alloy at different extrusion speeds and temperature; a) 250 °C, b) 300 °C and c) 400 °C.

4.5 Yield asymmetry on the extruded bars

In this section, the tension-compression yield asymmetry of the extruded bars is analyzed. Such yield asymmetry is presented as a function of the extrusion speed, see figure 4.19. The extrusion temperature is constant.

Figure 4.19a displays the yield asymmetry in the Z1 alloy. The alloy shows the well know yield asymmetry where the TYS is significantly higher compared to the CYS. At the extrusion temperature of 250 °C (black dotted line) and 300 °C (blue dotted line), the yield asymmetry shows a similar trend. The alloy displays an increment of the yield asymmetry as the extrusion speed increases. At extrusion temperature of 400 °C (gray dotted line), the modification of the extrusion speed shows an increment of the yield asymmetry (2.0 mm/s to 5.0 mm/s). Then, at 7.5 mm/s, it reduces.

Figure 4.19b shows the yield asymmetry in the ZX10 alloy. From the graph, it can be seen that at the extrusion temperature of 250 °C (black dotted line) and 300 °C (blue dotted line) the yield asymmetry decreases. Clearly, the highest yield asymmetry is observed at the extrusion temperature of 400 °C (gray dotted line). At this extrusion temperature, the yield asymmetry is quite comparable at all extrusion speeds.

Figure 4.19c provides the yield asymmetry in the ZNd10 alloy. At 250 °C of extrusion temperature, the yield asymmetry reduces when the material is extruded from 2.0 mm/s to 5.0 mm/s (black dotted line). There is observed a slight increment with the further increase of extrusion speed. A similar tendency is observed when the material is extruded at 300 °C (blue dotted line). The yield asymmetry is quite similar at the extrusion speed of 2.0 mm/s and 5.0 mm/s, while the lowest is observed at 7.5 mm/s. At the extrusion temperature of 400 °C (gray dotted line), the yield asymmetry is quite similar at the extrusion speed of 2.0 mm/s and 5.0 mm/s, while the lowest is observed at 7.5 mm/s.

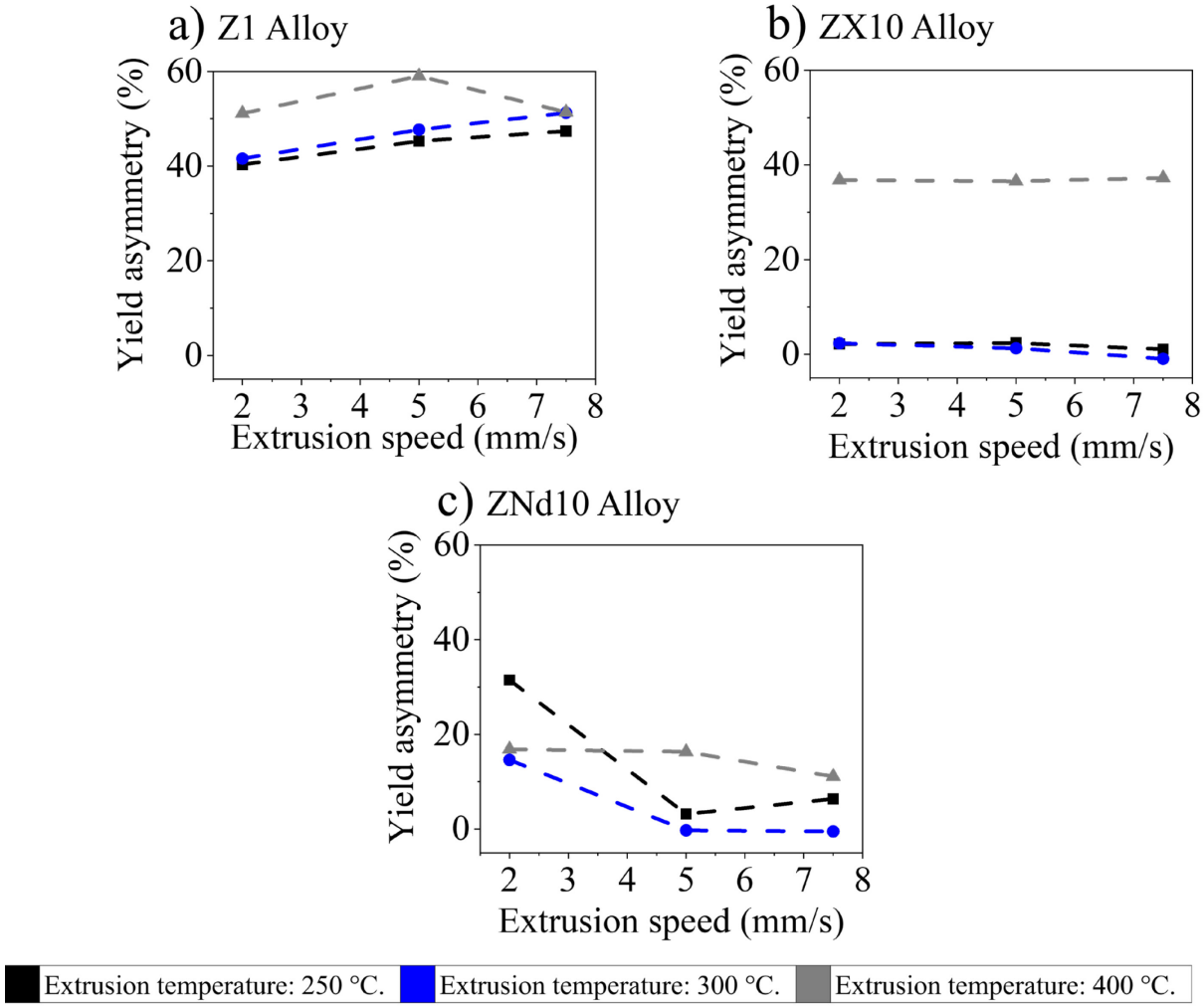

Figure 4.19. Variation of the tension-compression yield asymmetry as a function of extrusion speed for a) Z1 alloy, b) ZX10 alloy, and c) ZNd10 alloy. The extrusion temperature is constant; 250 °C (black dotted line), 300 °C (blue dotted line) and 400 °C (gray dotted line).

5. Discussion

5.1 The importance of the alloy composition on the extrusion processing

The alloy composition plays an important role in the flow metal during the extrusion processing. The force resulted during processing determines the characteristics of the resulting profiles.

The peak force reached of each alloy is quite different. Taken from the diagram of extrusion force vs ram displacement (figures 4.1 to 4.3 of section results); the figure 5.1 displays the progressive evolution of peak force during processing of each alloy. Figure 5.1a displays the peak force of the alloy Z1. The peak force follows a similar trend at all constant extrusion temperature. It increases slightly as the extrusion speed increases. The lowest peak forces on the Z1 alloy are at the extrusion temperature of 400 °C (gray dotted line).

Figure 5.1b exhibits the peak force in the ZX10 alloy. The drop in the peak force of the ZX10 alloy at the extrusion temperature of 250 °C can be correlated with the activation of a softening mechanism (black dotted line). At the extrusion temperature of 300 °C (blue dotted line), the peak force is maintained constant. However, at 400 °C (gray dotted line) a reversed effect occurs, the peak force increases with the increment of extrusion speed.

Figure 5.1c shows the peak force in the ZNd10 alloy. In general, in the Nd containing alloy the peak force is quite constant at all the extrusion temperature modifying the extrusion speed. The lowest peak forces are observed at the extrusion temperature of 400 °C (gray dotted line).

In summary, the highest peak force reached varies in each alloy, as can be seen in figure 5.1. It is quite clear that the maximum peak force achieved during processing is higher in the alloys with Ca and Nd additions. In contrast, the Z1 alloy, which is the base alloy, i.e. with the lower alloying concentration, is softer during extrusion. It has been reported that the increment of the alloying content increases the hot working flow stress and thus the extrusion load [1, 109]. In this regard, the findings in this work are consistent with results previously reported.

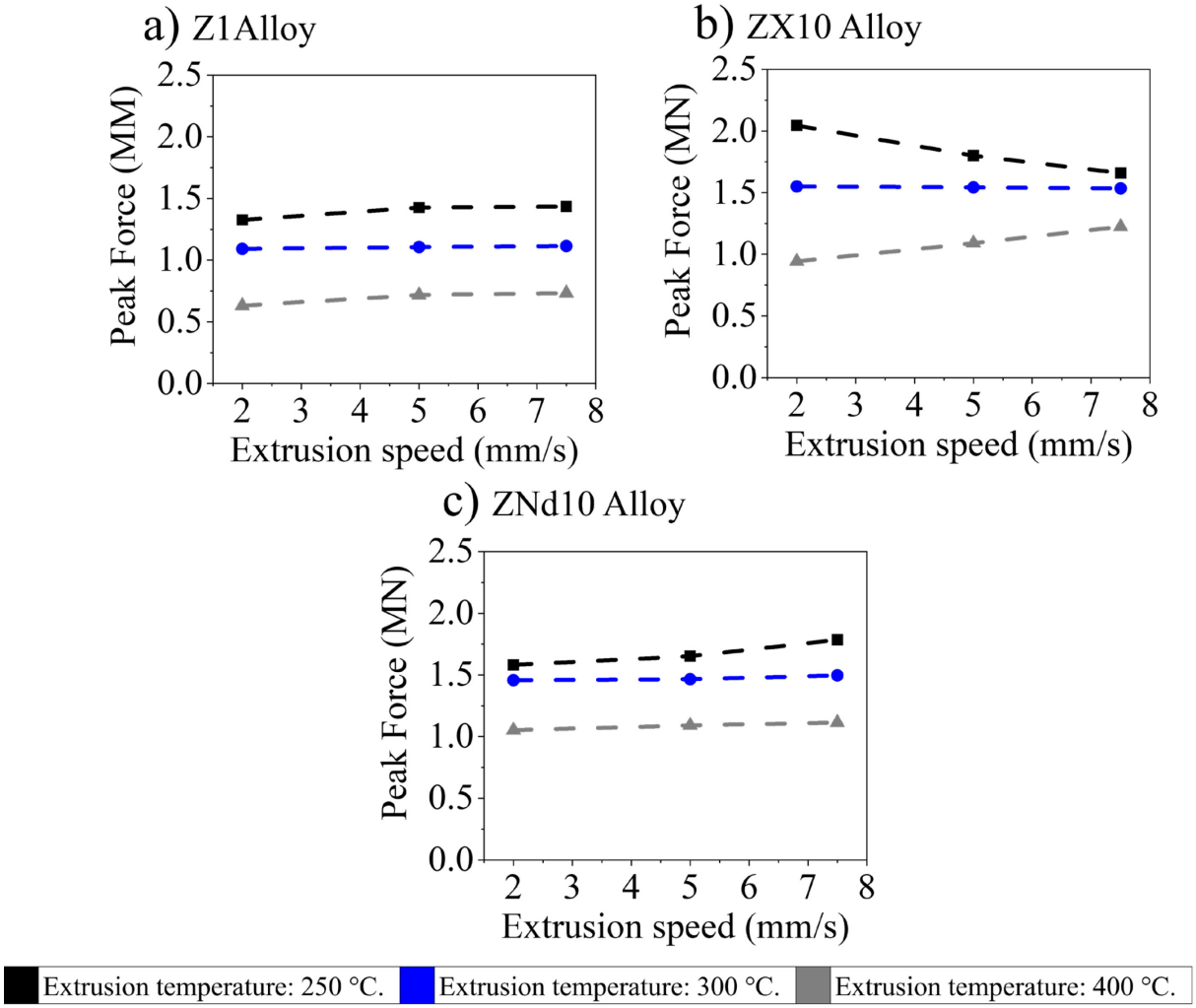

Figure 5.1. Variation of peak force reached during extrusion processing as a function of extrusion speed for a) Z1 alloy, b) ZX10 alloy, and c) ZNd10 alloy. In each plot, the black dotted line represents the temperature of 250 °C; the blue dotted line denotes the temperature 300 °C while the gray dotted line stands for the temperature of 400 °C.

The surface of the extruded bars was visually examined to determine the effect of the applied extrusion parameters, figures 4.4 to 4.6. At some extrusion parameters in the alloys was reached an eventual condition, in such a way that produced the visibility of some striations perpendicular to the ED. Those striations could be considered as micro cracks. Such micro cracks can be consistent with the hot cracking phenomenon as observed previously [62]. However, in the alloys of the present work, such a phenomenon is not so severe. Then, the surface quality of the bars is not so affected. According to the extrusion limit diagrams, the extrusion of the alloys in this work have been done near to the press limit (left side of figure 2.9). In the case of a material with good extrudability, it can be extruded with low extrusion load, having a good surface finish [11]. Then, it can be considered that the alloys of this work show a good extrudability. Through the observation of the bars' surface, some lines parallel to the extrusion direction are also perceived. The extrusion dies used could have caused the appearance of these lines on the surface of the extruded bars.

5.2 Effect of extrusion conditions on the microstructure and texture evolution.

Due to the applied extrusion parameters, each alloy developed different microstructures and crystallographic textures. Thus, in this section, the microstructure and texture evolution are discussed as a function of the extrusion temperature or extrusion speed.

From the micrographs of the longitudinal sections after extrusion with varied extrusion speed or temperature, it is possible to analyze the recrystallization process on the three alloys. The recrystallization process on the binary alloy Z1 is completed at any extrusion condition. Then, this binary alloy shows a completely recrystallized microstructure. In comparison to the Z1 alloy, single additions of Ca or Nd into the Mg-Zn based alloy have a significant effect on the microstructure development during extrusion. The recrystallization process is delayed in the presence of Ca or Nd. The retardation of the recrystallization process is more pronounced in the Nd containing alloy rather than the Ca containing alloy. This is observable due to the presence of large elongated grains, especially at the lowest extrusion temperature combined with the lowest extrusion speed (figure 4.7 on the section results). Once the recrystallized process is finalized, the grain growth starts. Figures 5.2 and 5.3 depicted the evolution of the average grain size as a function of the extrusion temperature and extrusion speed, respectively.

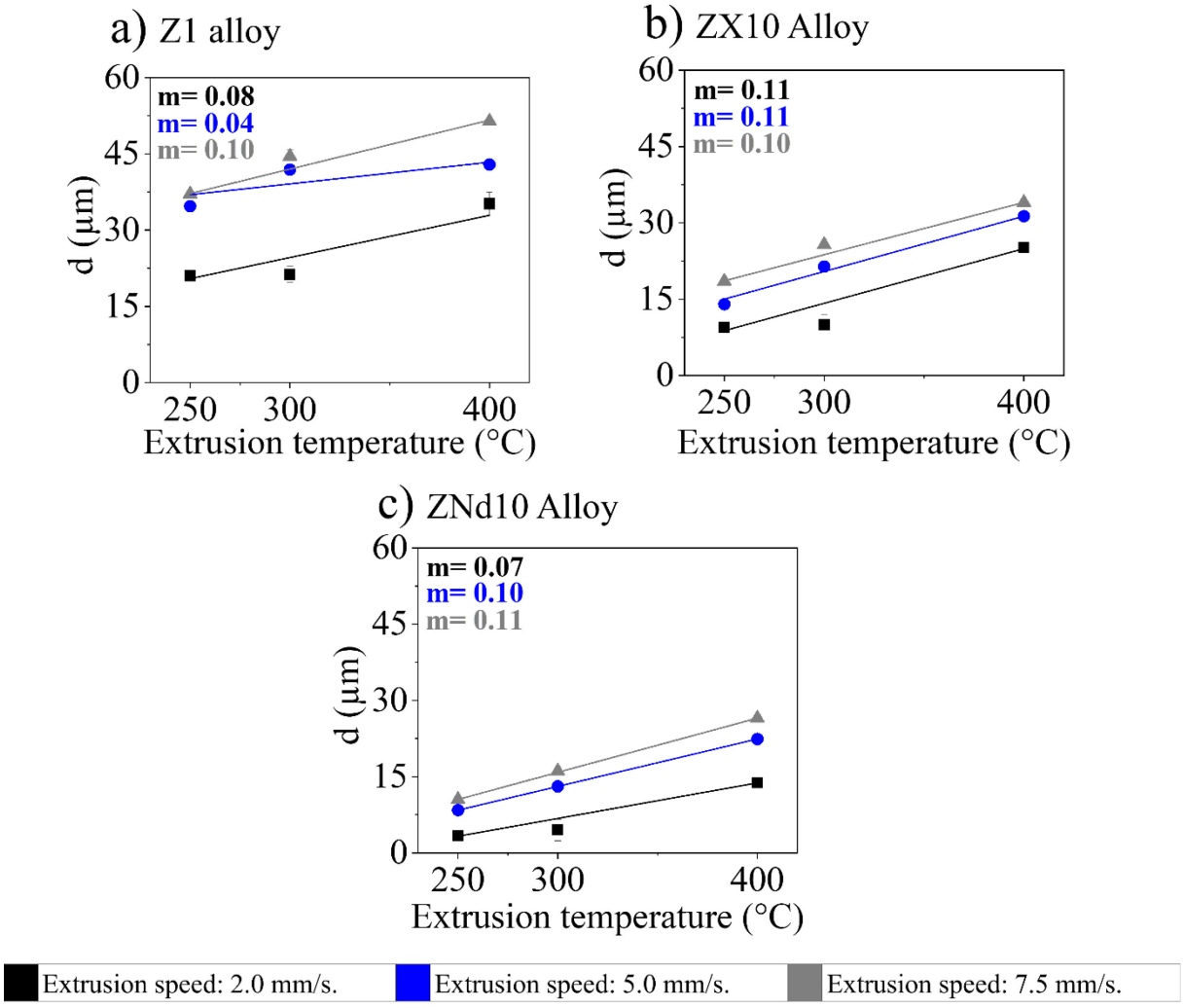

Figure 5.2. Variation of the average grain size (d) as a function of extrusion temperature; a) Z1 alloy, b) ZX10 alloy, and c) ZNd10 alloy. The letter (m), represents the slope of each curve, and is differentiated by black, blue and gray colors. The extrusion speed is constant.

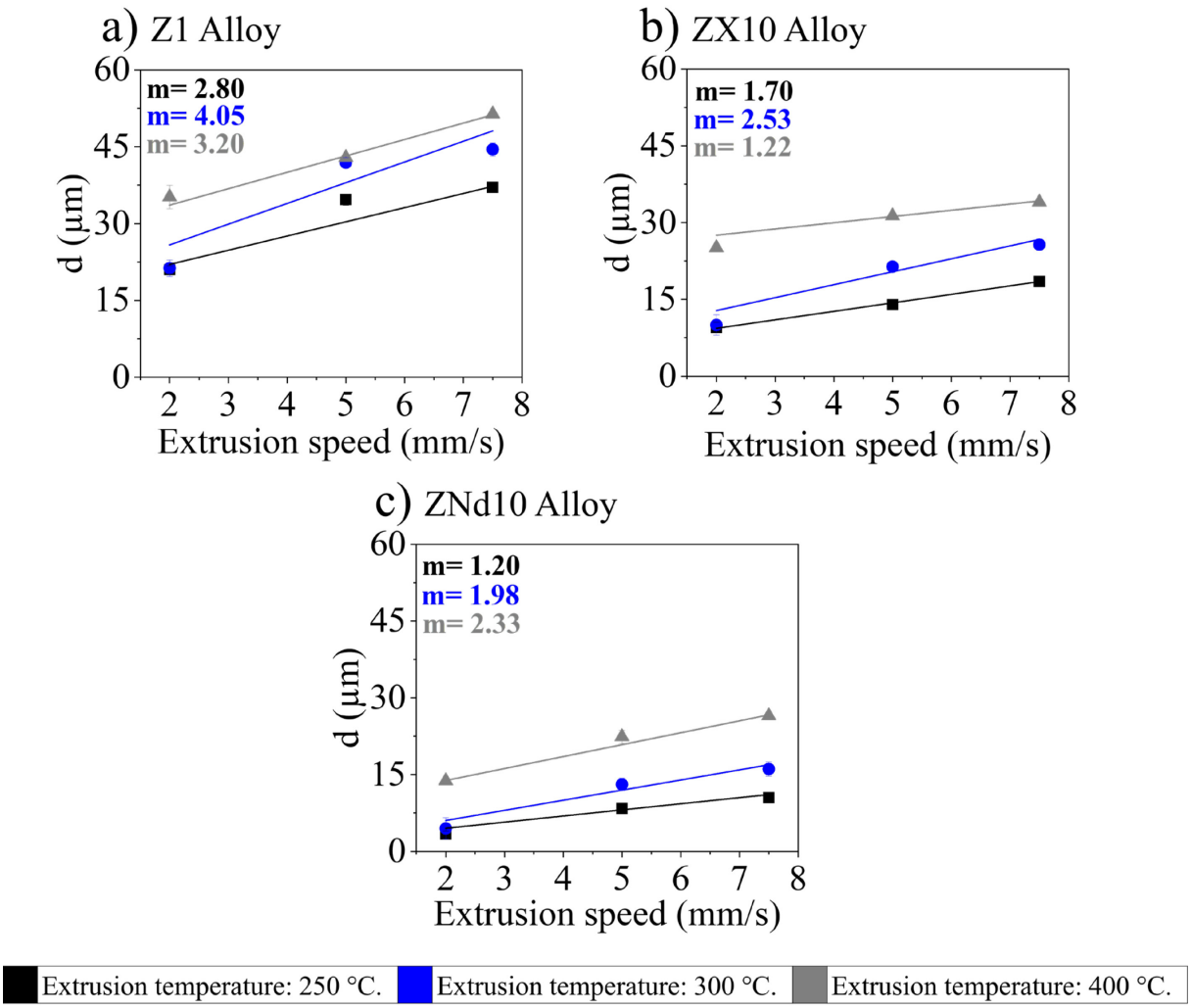

Figure 5.3. Variation of the average grain size (d) as a function of extrusion speed; a) Z1 alloy, b) ZX10 alloy, and c) ZNd10 alloy. The letter (m), represents the slope of each curve, and is differentiated by black, blue and gray colors. The extrusion temperature is constant.

As is depicted, the grain coarsening in the three alloys is affected in a similar way (figures 5.2 and 5.3). There is an increment of the average grain size (d) as the extrusion temperature or speed is increased. However, the grain growth in the binary Z1 alloy is more pronounced. The grain growth kinetics decreases substantially in the Ca and Nd containing alloys compared with the Z1 alloy. Furthermore, from the tendency displayed in the previous pictures, the grain growth is more retarded in the presence of Nd rather than Ca. This is visible even at the highest extrusion temperature or extrusion speed.

Regarding the evolution of the grain growth, investigations have proved that by increasing the extrusion temperature [110, 111] or the extrusion speed [4, 31, 95] there is an increase on the average size of dynamically recrystallized grains. The observed grain growth during the increment of extrusion speed is associated with the deformation related heating. This can lead to a temperature difference between the initial billet temperature and processing temperature [112]. Furthermore, it has been suggested that the net result in temperature increase is a linear function of the logarithmic ram speed [113]. Consequently, the deformation modes, DRX and the subsequent grain growth are affected by the temperature, thus influencing the grain size [112].

According to the findings, the grain coarsening velocity is much more pronounced when the extrusion speed is modified rather than when the extrusion temperature is modified.

The generated extrusion crystallographic textures during the application of the different extrusion parameters are shown in the section results, figures 4.10 to 4.12. The developed texture in the Z1 alloy is a classical texture where the basal planes are located between the prismatic planes. This result in such an alloy is present at any modification of extrusion speed or temperature tested. Although there is a spread between the prismatic planes, the highest intensities are found at the $< 11\bar{2}0 >$ pole. This kind of texture orients basal planes mostly parallel to the extrusion direction and has often been reported for fully recrystallized extruded bars of magnesium alloys such as AZ31 [114].

Different features in the texture evolution are observed in the ZX10 and ZNd10 alloys. The intensities observed at the $< 10\bar{1}0 >$ component in the ZNd10 alloy, also orients the basal planes parallel to the extrusion direction. Such a fibre texture has been associated with the non-recrystallized fraction of the microstructure [4]. In both ternary alloys, a component is established with intensity in the vicinity of the $< 11\bar{2}1 >$ pole. Such $< 11\bar{2}1 >$ component is often observed in rare earth or calcium containing alloys and it is normally known as "rare earth component" [40]. This component tilts the basal planes out of the ED. The crystallographic texture in ZX10 and ZNd10 alloys is rather weak and the main texture component changes. In the ZX10 alloy, an intensity seems to concentrate close to the $< 10\bar{1}1 >$ pole, thus maintaining the same tilt of basal planes out of the ED compared to the $< 11\bar{2}1 >$ "rare earth" component, but with a rotation up to 30° around the c-axis. Figure 5.4 displays a schematic representation of such rotation.

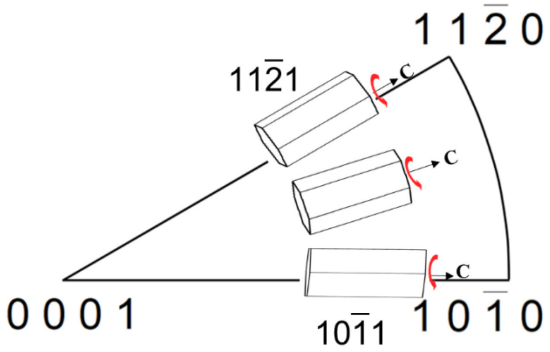

Figure 5.4. Schematic representation of the rotation around the *c*-axis.

5.3 Recrystallization on the extruded alloys

The recrystallization is a process that has a direct influence on the microstructure-texture and therefore on the mechanical properties of the extruded products. It has been observed in the results section that depending on the extrusion parameters it is possible to obtain a variety of microstructures. In that regard, the alloys were extruded at very low extrusion speed to achieve partly recrystallized microstructures to study the impact of specific fractions of the microstructure on the crystallographic texture. In figure 5.5, the EBSD-IPF maps of the partially recrystallized microstructure of the three alloys extruded at 300 °C and 0.1 mm/s are depicted. The microstructure consists of large elongated, un-recrystallized grains surrounded by newly formed recrystallized grains. In the Z1 alloy the classical texture where the basal planes are between the $< 11\bar{2}0 >$ and $< 10\bar{1}0 >$ prismatic poles were observed.

On the other side, the texture of the ternary alloys was dominated by the $< 10\bar{1}0 >$ and $< 11\bar{2}1 >$ components. A separation of the recrystallized and un-recrystallized fractions of grains is assisted based on the consideration of the internal orientation spread of grains, the grain orientation spread (GOS) [4, 74, 115]. It is assumed that recrystallized grains exhibit low in-grain misorientations because of a lattice free of dislocations, which are an important source of such misorientations. On the other hand, grains that underwent plastic deformation and experienced active slip modes would result in higher GOS. These recrystallized and un-recrystallized fractions were separated to observe possible hints of the origin of the observed texture components. Arbitrarily, a GOS value of 1° as a separator is considered in this work.
This analysis revealed that the fraction of the microstructure corresponding to the recrystallized grains (GOS<1°) in the Z1 alloy have a clear orientation tendency to develop the $< 11\bar{2}0 >$ pole while the ZX10 and ZNd10 alloys show a relatively weak texture, although they preserve their orientations mainly at the prismatic $< 10\bar{1}0 >$ pole (figures 5.5 a-c). According to this analysis, the component $< 10\bar{1}0 >$ is associated to the un-recrystallized grains in all alloys (GOS>1°), besides, this component is significantly more pronounced.

One interesting finding here is that in the ZX10 alloy, the rare earth texture component at the $< 11\bar{2}1 >$ pole is revealed in the un-recrystallized fraction (GOS >1°) of the microstructure but not in the fraction of recrystallized grains (GOS <1°), see Figure 5.5b. On the other side, in ZNd10, both fractions include grains with such orientation, i.e.,$< 11\bar{2}1 >$, (Figure 5.5c). It is believed that the element segregation modifies the grain growth kinetics, which changes the components in the texture. This is the case for the Nd containing alloy, where the component $< 11\bar{2}1 >$ in the deformed condition with small DRX grains remain and preserve a certain grain growth uniformity. Such grain growth restrictions have been also linked with the appearance of the "rare-earth texture" in conventional AZ31 Mg alloys [116]. In AZ31 the grains with the basal planes parallel to ED normally grow unless a mechanism is active that changes the growth kinetics e.g., particles that restrict the grain growth. The grain growth tendency can be changed by particles in a way, that in recrystallized microstructures of AZ31 the $< 11\bar{2}1 >$ pole component can also be observed. On the contrary, in the Ca containing alloy there is not such a strong restriction to recrystallization and grain growth.

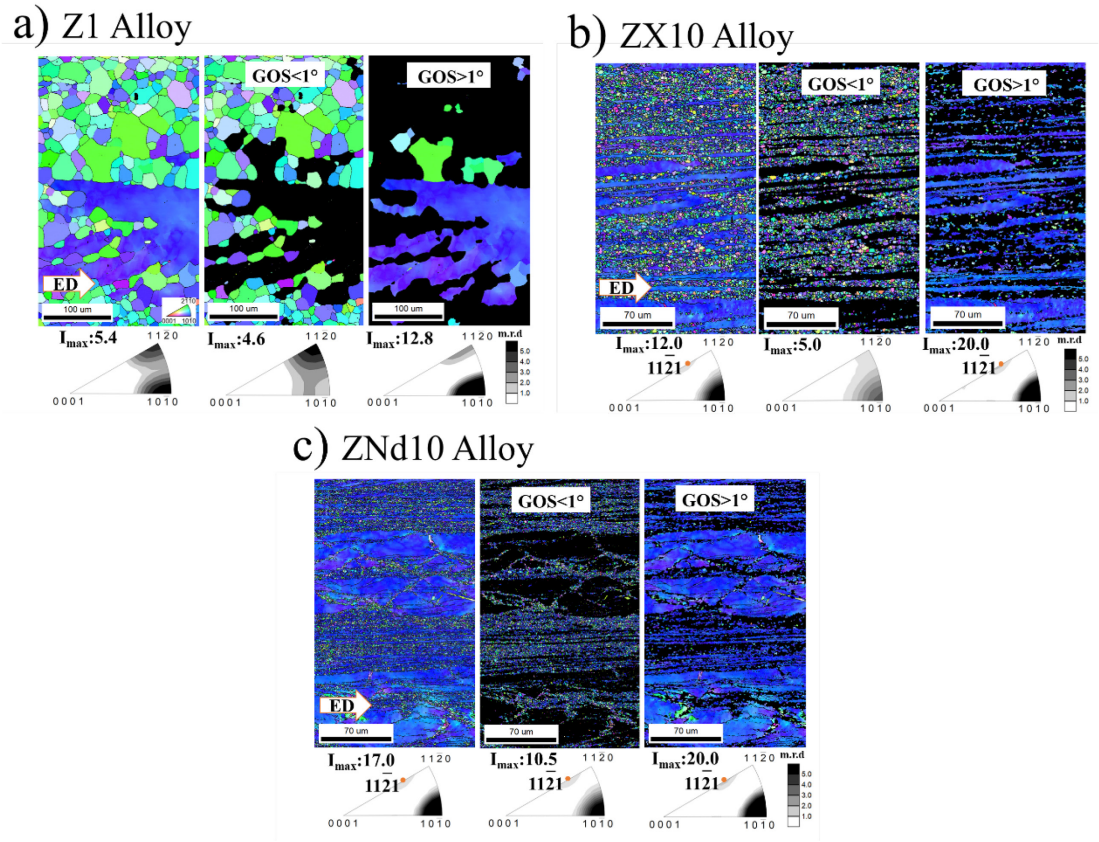

Figure 5.5. IPF maps corresponding to partly recrystallized microstructure in a) Z1 alloy, b) ZX10 alloy and c) ZNd10 alloy extruded at 0.1 mm/s and 300 °C [95].

The grain growth plays a key role in the determination of the final texture of a thermo-mechanically processed product. Grain growth is regarded as the migration of grain boundaries taking place during the recrystallization process [117]. Two types of recrystallization are considered in the grain growth of a processed material, i.e. dynamic and static recrystallization. Therefore, in the following two sections, is discussed the effect of dynamic (DRX) and static recrystallization (SRX) processes on the texture of the alloys.

5.3.1 Effect of dynamic recrystallization on the texture

In order to differentiate the effect of different fractions and grain dependence of dynamically recrystallized microstructures on the texture, the fractions of dynamically recrystallized grains developed at low and intermediate extrusion speeds were evaluated. The average grain size of dynamically recrystallized grains (d_{rec}) has been considered as a limit to determine the effect of grain growth on the orientation development of such grains, thus separating small and large recrystallized grains.

In figures 5.6a and 5.6b the recrystallized fraction of the microstructures of Z1 extruded at 0.1 mm/s and 0.6 mm/s, is shown respectively. The picture that emerges from the analysis at these extrusion conditions is that in this alloy both fraction of the grains show a spread between the $<10\bar{1}0>$ and the dominant $<11\bar{2}0>$ components. However, there is a subtle trend to strengthen the $<11\bar{2}0>$ component as grain coarsening takes place. Figures 5.6c and 5.6e exhibit the recrystallized fraction of microstructures and respective textures after slow extrusion (0.1 mm/s) of the ZX10 and ZNd10 alloys.

According to the same criterion, i.e., the consideration of average grain size, it revealed a slight change compared to the deformation component in figure 5.6 for ZNd10 and ZX10 alloys. In ZX10 alloy, the main orientation at the $< 10\bar{1}0 >$ pole is maintained; however it seems to be more pronounced in the smaller grains, this is observed in the texture in figure 5.6c, d <3.0 μm. In contrast, in the d >3.0 μm, potentially those grains with a growth advantage during recrystallization, an angular spread towards the $< 0001 >$ pole (and therefore towards the $< 10\bar{1}1 >$ pole) is found. Different to the previous alloy, ZNd10 was shown not to have such a grain size dependence. Both intensities at the $< 10\bar{1}0 >$ pole, and the $< 11\bar{2}1 >$ pole, remain comparable, see Figure 5.6e. It has been observed that increasing the extrusion temperature or speed there is an increment of the grain growth (section results); therefore, a detailed analysis of the effect of grain coarsening on the texture is done. For that analysis, the effect of grain coarsening as a function of increasing the extrusion speed for ZX10 (2.0 mm/s) and ZNd10 (5.0 mm/s) alloy was used which is depicted in figures 5.6d and 5.6f, respectively.

With grain coarsening by increasing the extrusion speed, the separation of grains applying the average grain size criterion, both alloys tend to develop intensity along the arc between the $< 10\bar{1}1 >$ and the $< 11\bar{2}1 >$ poles, which establishes a rotation of 30° around the *c*-axis of the hcp structure. For ZX10, in the small grain size, there is no clear dominance between the intensities at $< 10\bar{1}1 >$ and $< 11\bar{2}1 >$ poles, see texture in figure 5.6d, d <11.0 μm. However, for the d > 11.0 μm (Figure 5.6d) the $< 10\bar{1}1 >$ pole is stronger. This indicates the importance of grain coarsening in the formation of the $< 10\bar{1}1 >$ component in the ZX10 alloy. For ZNd10, in the d < 9.8 μm (figure 5.6f), it seems that the intensity at the $< 10\bar{1}1 >$ pole is somewhat higher, while with the d >9.8 μm the $< 11\bar{2}1 >$ pole is more pronounced. Thus, the preference of grain orientations changes with the extrusion speed and the concomitant grain coarsening of recrystallized grains.

In each alloy, the texture evolution due to the grain growth during the DRX recrystallization process is different. In Z1 alloy, the grains are principally spread between the prismatic poles $< 10\bar{1}0 >$ and $< 11\bar{2}0 >$. The latter one is strengthened as grain growth of recrystallized grains takes place. Such behavior is modified if Ca or Nd is added to the Mg–Zn alloy systems. The $< 10\bar{1}1 >$ becomes more dominant in the Ca containing alloy as grain growth takes place, while in the Nd containing alloy the coarse grains are mostly oriented towards the $< 11\bar{2}1 >$ component.

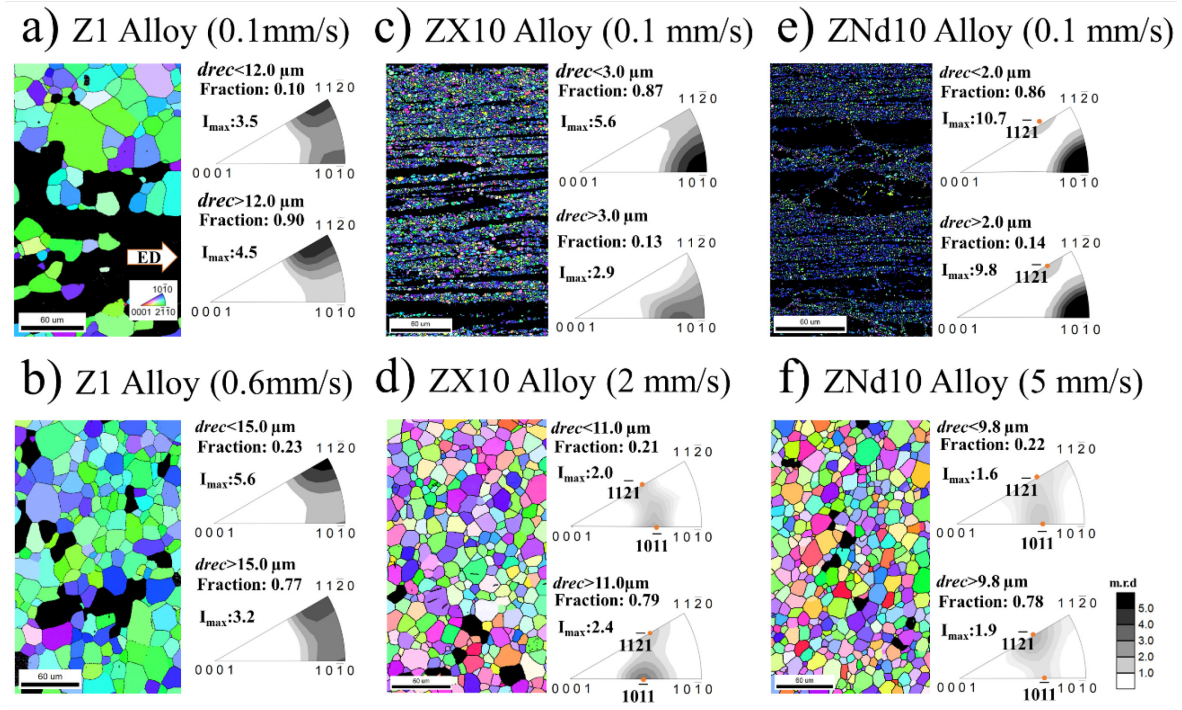

Figure 5.6. Recrystallized grains: a) Z1, c) ZX10, e) ZNd10 alloy extruded at 0.1 mm/s and b) Z1 extruded at 0.6 mm/s, d) ZX10 extruded at 2.0 mm/s and f) ZNd10 extruded at 5.0 mm/s using 300 °C of extrusion temperature [95].

5.3.2 Effect of static recrystallization on the texture

After extrusion, the remaining heat during cooling down of the extruded bars is affecting the microstructure and texture, i.e. SRX is already activated but in an uncontrolled way. Such a change can be better explained using samples with partially recrystallized microstructures subjected to subsequent annealing. Then, to systematically determine the role of SRX on the texture development, partly recrystallized of samples from ZX10 and ZNd10 extruded bars at 0.1 mm/s were annealed. It is important to note that in all the applied extrusion parameters on Z1 alloy of this study, the microstructure is completely recrystallized. Therefore, the analysis of Z1 is not presented because no changes in the texture were found after SRX because of the high fraction of recrystallized.

On the other hand, the microstructures of samples from the ZX10 and ZNd10 alloys were tailored so the grain structure of the SRX samples could be compared to grain structures of DRXed samples, i.e., samples extruded at 2.0 mm/s for ZX10 alloy and 5.0 mm/s for ZNd10 alloy. The annealed microstructures of the ternary alloys revealed visible texture changes.
Figure 5.7 shows that after static recrystallization at 400 °C for 3.0 min in the case of ZX10 (figure 5.7a) and 30 min for ZNd10 alloy (figure 5.7b) the texture is remarkably different to the counterparts dynamically recrystallized microstructures, ZX10 alloy (figure 4.11) and ZNd10 alloy (figure 4.12) extruded at 300 °C. During SRX of the two alloys, intensity along the arc between $< 10\bar{1}0 >$ and $< 11\bar{2}0 >$ poles is maintained. In ZX10, there are orientations with tilt out of the $< 10\bar{1}0 >$ pole, e.g., to the $< 20\bar{2}1 >$ pole, which also leaves basal planes with a tilt out of the extrusion direction, figure 5.7a.

A stronger alignment of basal planes along the arc between $< 10\bar{1}0 >$ and $< 11\bar{2}0 >$ poles after static recrystallization is also visible on the ZNd10 alloy, figure 5.7b. Besides, there are orientations with varied tilt angle (e.g., at $< 20\bar{2}3 >$ pole).

The static recrystallization weakens the texture of the partly recrystallized samples but in essence, the grains maintain their orientation in the surrounding of the $< 10\bar{1}0 >$ pole in Ca and along the arc between the $< 10\bar{1}0 >$ - $< 11\bar{2}0 >$ poles in the Nd containing alloy. This means that they inherit the orientation of the dominant deformation texture component with the concomitant stronger recrystallization texture compared to the DRXed textures. At the end of static recrystallization, the basal planes remain aligned parallel to the ED. Although the $< 11\bar{2}1 >$ RE component is present in the partly recrystallized microstructure (initial condition, figures 5.5b and 5.5c), in both alloys such a component is suppressed after SRX.

These results reflect those of Imandoust et al. [118] who also found that the RE grains disappear after the SRX process of an Mg-Zn-Al-Mn-Y alloy. It was explained that such behavior could be attributed to an isotropic grain growth process due to a grain boundary co-segregation effect that decreases the anisotropy in grain boundary energy and mobility. It is hypothesized in the context of the modification of extrusion speed that the change of the balance of active deformation mechanisms as the temperature is increased as the extrusion speed increases. The importance of certain deformation mechanisms along with rapid coarsening of recrystallized grains could also influence the dominance of the RE-texture component.

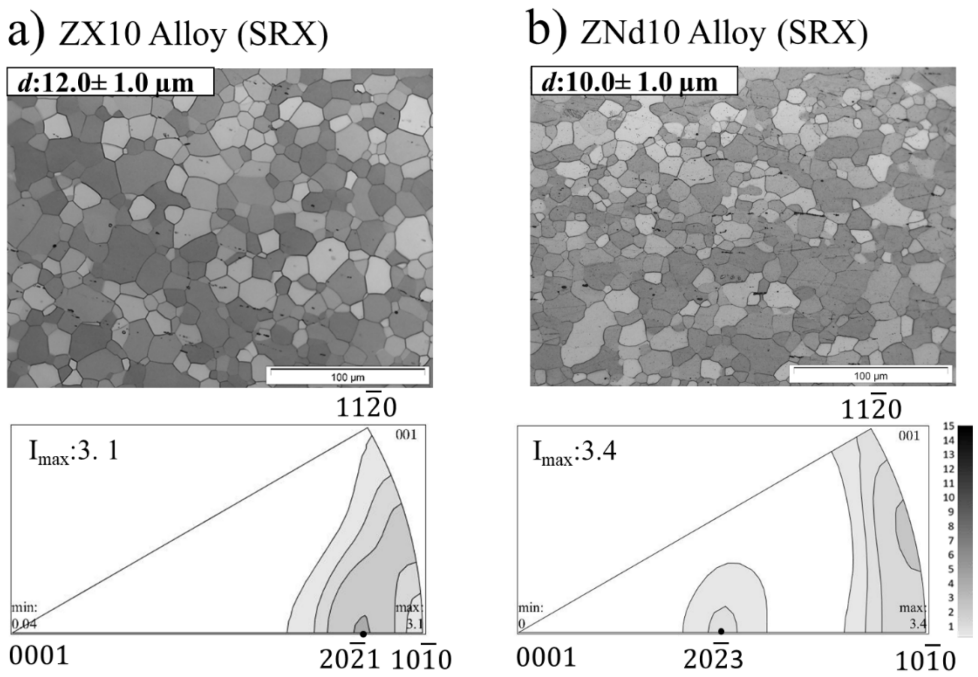

Figure 5.7. Microstructure and texture after static recrystallization (SRX) at 400 °C; a) ZX10 alloy for 3.0 min and b) ZNd10 alloy for 30 min. The inset (*d*) represents the average grain size [95].

5.4 Correlation between microstructure and mechanical properties

The mechanical properties of magnesium alloys, such as yield strength, yield asymmetry and strain to fracture are strongly influenced by grain size and texture. It is well known that the strength increases based on the grain refinement.

In that sense, the dependence of the yield strength with respect to the grain size is principally governed by the Hall-Petch relationship:

$$\sigma_y = \sigma_0 \ + \ k_y \, d^{-1/2} \qquad \text{(Eq. 9)}$$

Where σ_y corresponds to the yield stress, σ_0 is the friction stress when the dislocations move on the slip plane, *d* refers to the average grain size and k_y is the stress concentration factor. The micro mechanism could be understood in terms of pile-up of dislocations in the vicinity of the grain boundary [119].

In this section, the effect of grain size on the yield stress on tension and compression is analyzed. The considered grain size variation is from the extruded materials at constant temperature with different extrusion speed. Considering the previous extrusion parameters, the average grain size (*d*) varies in the range from 21 to 51 µm for the Z1 alloy, while in the ZX10 alloy; (*d*) has a range from 9.5 to 35 µm and from 3.5 to 26.5 µm for the ZNd10 alloy. Figures 5.8 to 5.10 and table 5.1 displays the dependence of the CYS and TYS on the grain size. It was evaluated according to the Hall-Petch relationship. The results are shown separately for each alloy. The slope of the curves in each plot refers to the *k* value, which represents the grain boundary as an obstacle to slip across the grain boundaries.

In the present analysis of the Z1 alloy (figure 5.8), the slope of the curves (*k* value) of the material extruded at the different extrusion temperature and tested in compression is slightly bigger than in tension, see table 5.1a. This is observed in the alloy extruded at 250 and 300 °C, while at 400 °C there is an inverse relation. The bigger *k* value in compression rather than in tension agrees with previous studies [2, 120, 121]; this can be considered as an indicator that during deformation, the tensile twinning is more sensitive to grain refinement than crystallographic slip.

On the other hand, the ZX10 alloy (figure 5.9 and table 5.1b) and ZNd10 alloy (figure 5.10 and table 5.1c) alloys behave in a different way. The slope of the Hall-Petch plots, i.e., the *k* value, is greater in tension than in compression. This observed in all the analyzed cases. Such behavior can be attributed to the texture effect. As it is observed in the section of crystallographic texture evolution, these alloys developed textures where the main components are tilted out of the extrusion direction. Then, it can be suggested that in these two alloys the *k* value is not only affected by the grain size but also by the crystallographic texture. Here, there is observed a certain effect in the *k* values where such effect can be attributed to the crystallographic texture that modifies the balance of deformation modes. It is considered in [122] that when the texture development due to the mechanical processing makes the activation of basal slip during deformation easier; the k value would be reduced.

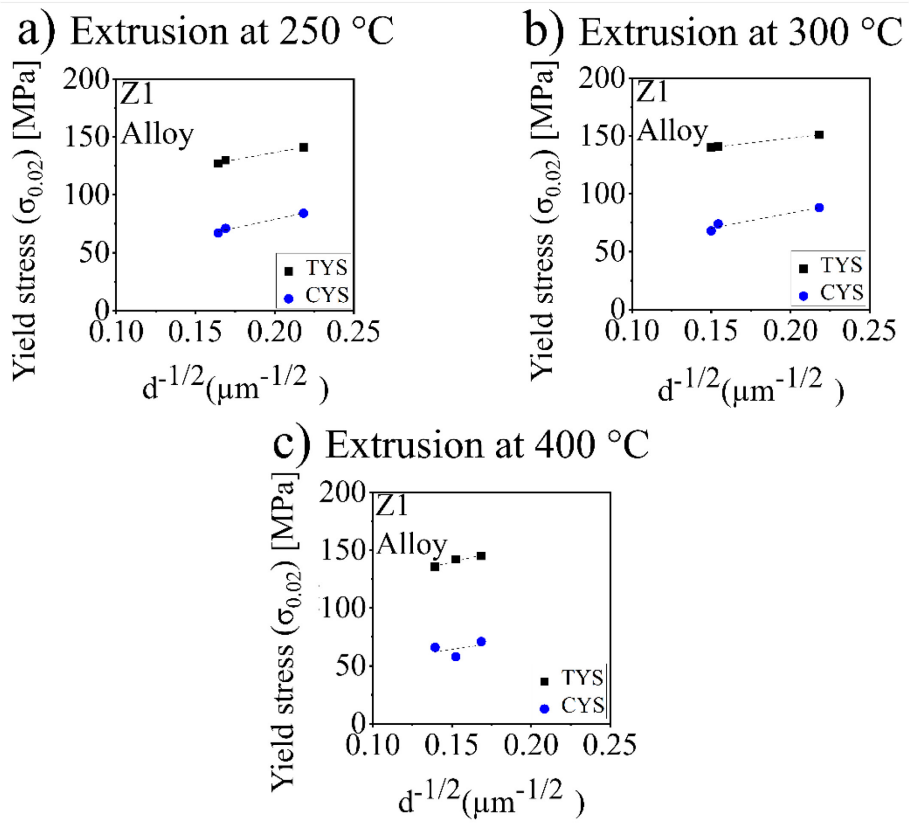

Figure 5.8. Variation of the tensile and compressive yield strength against $d^{-1/2}$ for the Z1 alloy extruded at a) 250 °C, b) 300 °C and c) 400 °C.

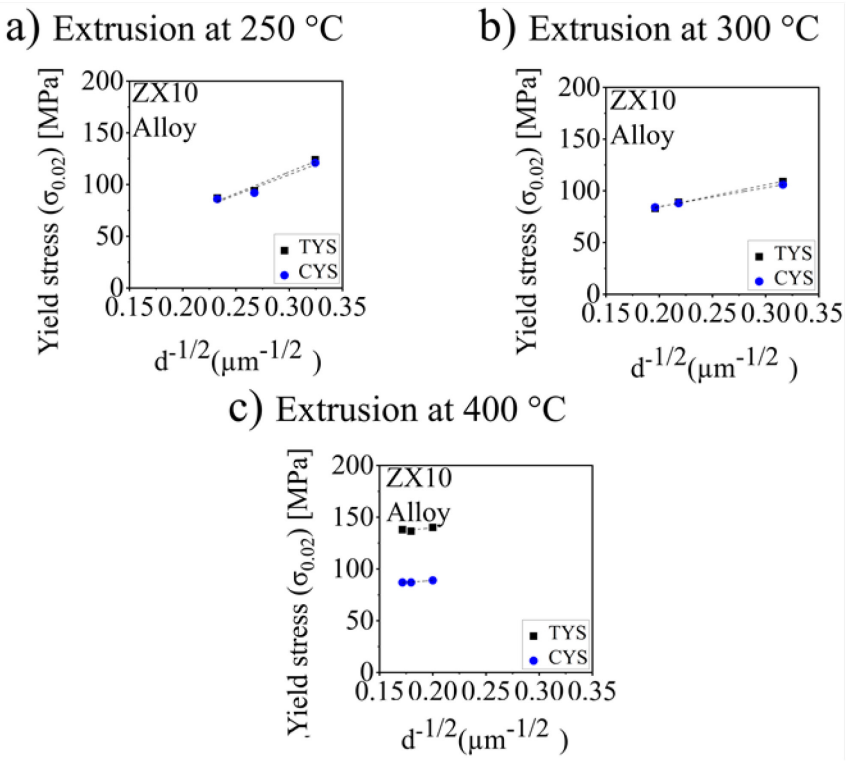

Figure 5.9. Variation of the tensile and compressive yield strength against $d^{-1/2}$ for the ZX10 alloy extruded at a) 250 °C, b) 300 °C and c) 400 °C.

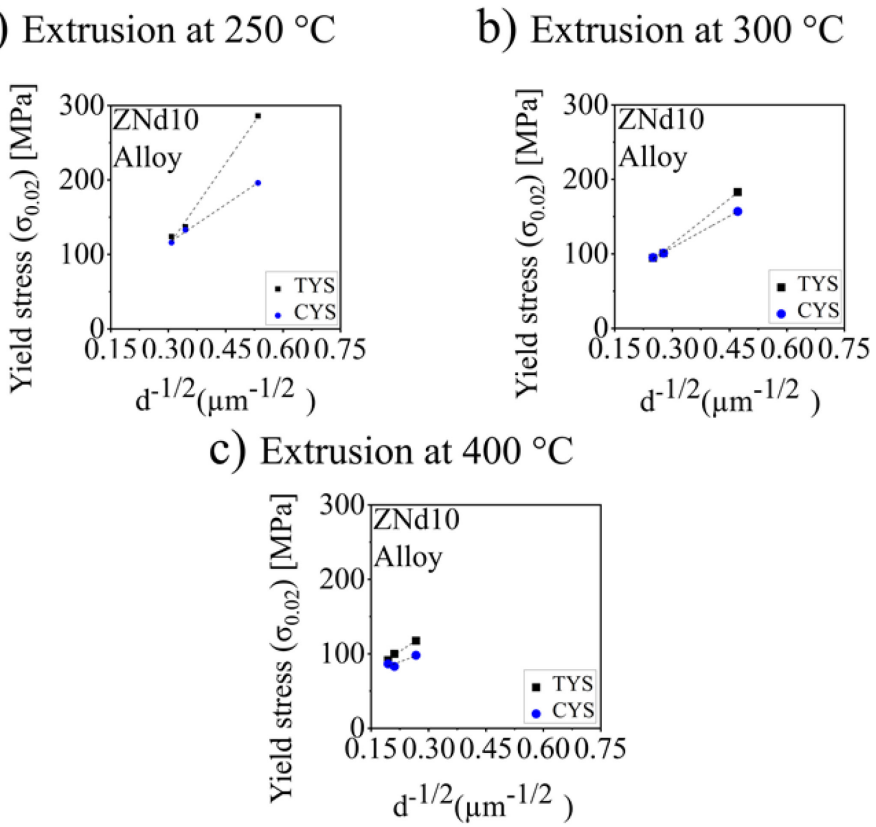

Figure 5.10. Variation of the tensile and compressive yield strength against $d^{-1/2}$ for the ZNd10 alloy extruded at a) 250 °C, b) 300 °C and c) 400 °C.

Table 5.1. Macroscopic Hall-Petch parameters for a) Z1 alloy, b) ZX10 alloy, c) ZNd10 alloy tested under tension and compression.

Extrusion temperature (°C)		a) Z1 alloy		b) ZX10 alloy		c) ZNd10 alloy	
		k (MPa $\mu m^{-1/2}$)	σ_0	k (MPa $\mu m^{-1/2}$)	σ_0	k (MPa $\mu m^{-1/2}$)	σ_0
250 °C	TYS	245	88	415	-12	740	-110
	CYS	297	20	393	-8	347	11
300 °C	TYS	159	116	213	42	408	-10
	CYS	261	31	183	48	283	23
400 °C	TYS	320	92	94	121	344	26
	CYS	194	35	76	74	185	48

5.5 Plastic deformation of the extruded alloys

As was previously shown, the addition of Ca or Nd modifies the microstructure and crystallographic texture and subsequently the mechanical properties of the Mg-Zn alloys. Therefore, in the following section, is analyzed the role of Ca and Nd additions on the activation of deformation modes in the Mg-Zn alloys and, furthermore, the development of deformation texture. To do so, experimental and simulation results are analyzed at different deformation strains. In figure 5.11 the optical micrographs and the crystallographic textures of the considered extruded bars are shown. The stress-strain curves obtained at room temperature in tension and in compression have been simulated using the VPSC model. During the simulation, the basal <a>, prismatic <a>, pyramidal <a>, pyramidal I <c+a> and pyramidal II <c+a> as

well as tensile twinning $(10\bar{1}2) < 10\bar{1}\,\bar{1} >$ and compressive twinning $(10\bar{1}1) < 10\bar{1}\,\bar{2} >$ were considered. The results from the VPSC simulations (crystallographic texture and hardening behavior) are then compared with experimental results.

As observed, materials with similar grain structure but different texture were employed. The average grain size (*d*) of each material for this study is observed in figure 5.11. A typical basal texture in Z1 alloy is observed, figure 5.11a. On the ZX10 alloy, the texture is dominated by the $< 10\bar{1}1 >$ pole, which is tilted out of the extrusion direction (figure 5.11b). The $< 11\bar{2}1 >$ pole, i.e., the rare earth texture component, dominates the texture in the ZNd10 alloy (figure 5.11c). Since the average grain size is comparable; then, its effect on the deformation behavior can be discarded. Therefore, the observed deformation behavior is entirely considered as an effect of the crystallographic texture. The different crystallographic texture in each alloy allows studying the activation of different deformation modes due the modification of its CRSS owing to the addition of alloying elements (Ca or Nd).

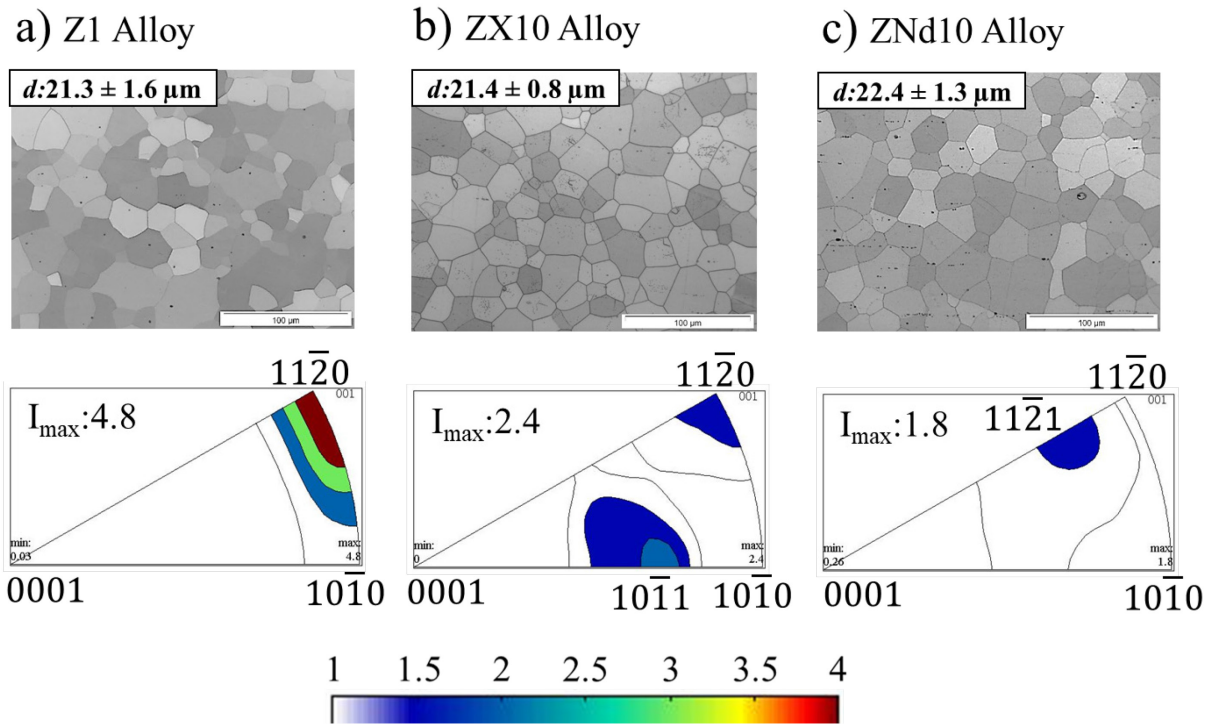

Figure 5.11. Optical micrographs and crystallographic texture of the a) Z1 alloy extruded at 300 °C and 2.0 mm/s, b) ZX10 alloy extruded at 300 and 5.0 mm/s and c) ZNd10 alloy extruded at 400 °C and 5.0 mm/s.

5.5.1 Microstructure evolution during tension and compression

In the following section, the evolution of the microstructure at the different analyzed deformation including the IPF maps together with and the IPF textures and the Image Quality (IQ) maps are shown. The IPF maps (colorful figures) show the microstructure evolution, while the IQ maps (gray figures) display the twinning structures formed during the deformation. At the bottom section of figures 5.12, 5.13 and 5.14 is displayed an inserted table, which shows the cumulative fraction of twinning.

During the deformation, in tension or compression, there is usually observed a characteristic grain rotation which is directly correlated with the activation of different deformation mechanisms. Then, applying the technique of EBSD the microstructure was analized. The microstrucutre does not experience a significant change during the tension of the Z1 alloy, see IPF maps of figure 5.12a. As the deformation proceeds from 0 to 0.12, the microstructure grain orientation is quite comparable. The IQ maps of this Z1 alloy under tension show that few twins nucleate at strain of 0.03, and the twin fraction is still low at larger tension strains. With the increment of strain, there is observed an increment of cumulative fraction of twinning (see inserted table at the bottom of figure 5.12a and b).

On the other hand, in compression the observed grain rotation (IPF maps in figure 5.12b) is attributed to the high twining activation. This is confirmed in the IQ maps (figure 5.12b). It is clear that in compression the fraction twinning is much more pronounced than in tension. The major fraction of twinning in compression rather than in tension is due to the basal texture which is formed during the extrusion process.

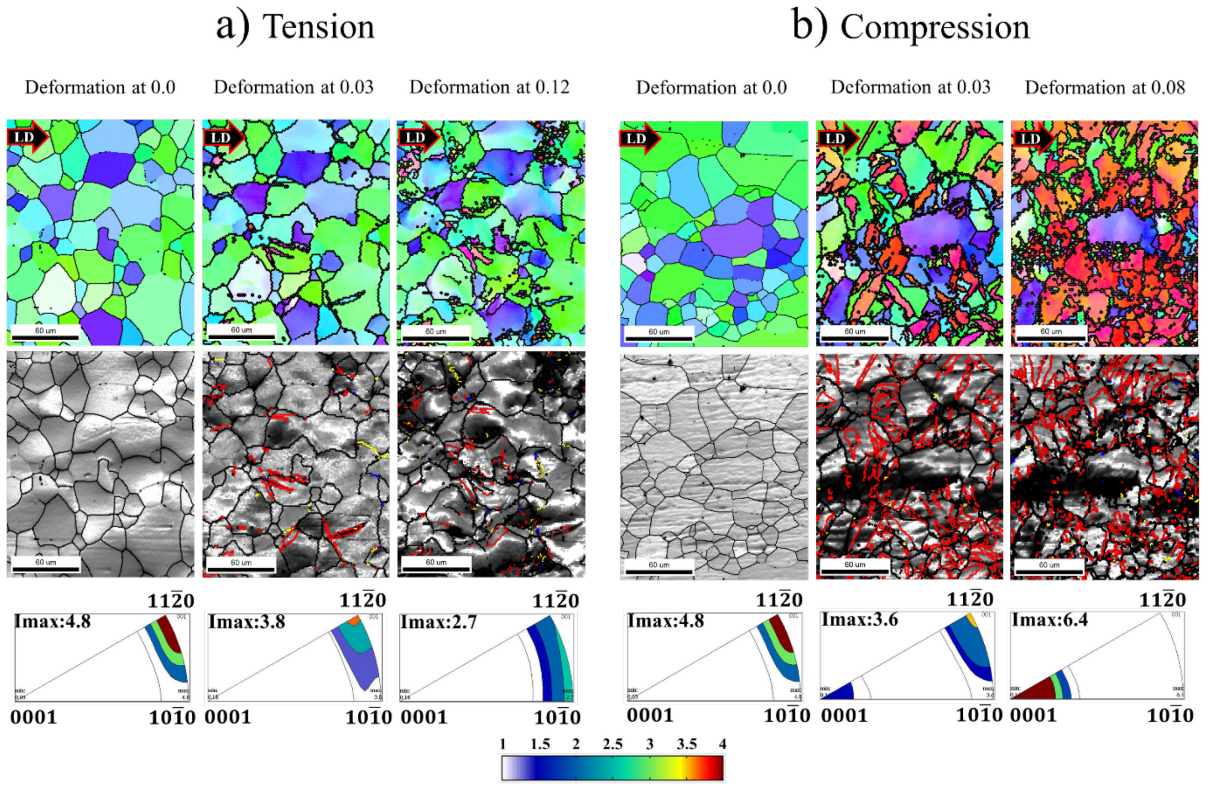

Twining type	(°)	Fraction at 0.03 deformation	Fraction at 0.12 deformation
Tension twin	86°	0.023	0.039
Compression twin	56°	0.002	0.006
Double twin	38°	0.001	0.004

Twining type	(°)	Fraction at 0.03 deformation	Fraction at 0.08 deformation
Tension twin	86°	0.112	0.194
Compression twin	56°	0.001	0.004
Double twin	38°	0.001	0.002

Figure 5.12. IPF maps (colorful figures) and IQ maps (gray figures) of Z1 alloy deformed in a) tension and b) compression. The twins are labeled in the IQ maps. The twinning fraction at each deformed microstructure is differentiated by red, blue and yellow colors. The black arrow indicates the load direction (LD).

In figure 5.13a the deformed microstructure of ZX10 alloy tested in tension is shown. The captured microstructure at each deformation stage shows an increment of twinning fraction.

In tension, traces of compresion and double twins are observed at 0.12. During the deformation in compression, twins first apear at 0.03 of strain and such twinning structures are also observed with the further deformation at 0.12 of strain, figure 5.13b. Altough the major fraction corresponds to the tensile twinning, the compression and double twins are also observed at such deformation stage.

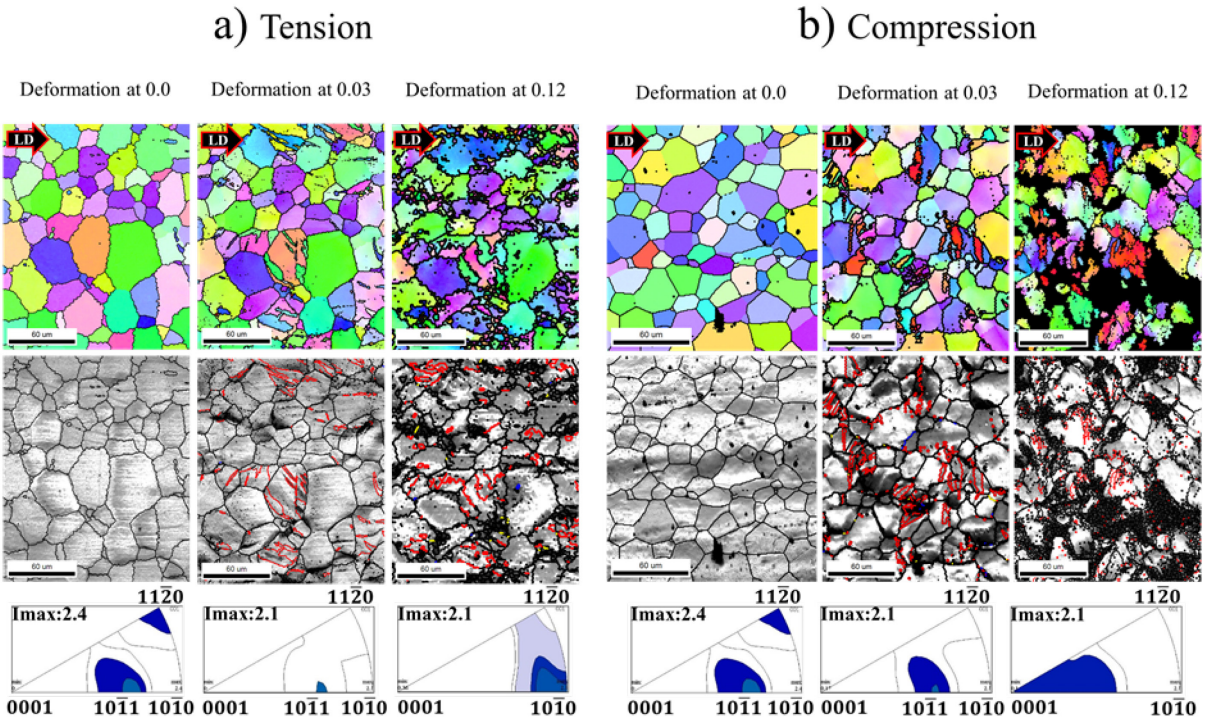

Twining type	(°)	Fraction at 0.03 deformation	Fraction at 0.12 deformation
Tension twin	86°	0.033	0.063
Compression twin	56°	0.003	0.006
Double twin	38°	0.001	0.002

Twining type	(°)	Fraction at 0.03 deformation	Fraction at 0.12 deformation
Tension Twin	86°	0.056	0.081
Compression twin	56°	0.001	0.005
Double twin	38°	0.001	0.003

Figure 5.13. IPF maps (colorful figures) and IQ maps (gray figures) of ZX10 alloy deformed in a) tension and b) compression. The twins are labeled in the IQ maps. The twinning fraction at each deformed microstructure is differentiated by red, blue and yellow colors. The black arrow indicates the load direction (LD).

The twinning evolution in the ZNd10 alloy in tension and compression is observed in figure 5.14. In tension, the activation of twinning is clearly observed at 0.03, figure 5.14a. From the activated fraction, the most activated corresponds to the tensile twin. According to the EBSD analysis, the cumulative fraction increases at 0.12 of deformation. On the other hand, when the alloy is tested in compression, the activation of twinning is observed since a low deformation, i.e., 0.03 (figure 5.14b). With the increment of strain up to 0.12, an increment is observed according to the cumulative fraction. A very low fraction of compression and double twins are also observed.

In the preceding figures, it is observed that the twinning mechanism is activated in the three alloys either in tension or in compression. However, the twinning activity is more pronounced in compression than in tension.

Moreover, from the considered three types of twinning, i.e., tensile twin, compression twin and double twin, the most activated consists on the tensile twinning.

Figures 5.12, 5.13 and 5.14 display the twin evolution in the three alloys as deformation proceeds. Fewer twins were seemingly detected at high deformation strains compared with low deformation strains (IQ maps). This could be explained due to the coalescence of twins or the vanishing of twin boundaries. As the deformation proceeds, there is a merging of pre-existing extension twins or the disappearance of twin boundaries [123, 124].

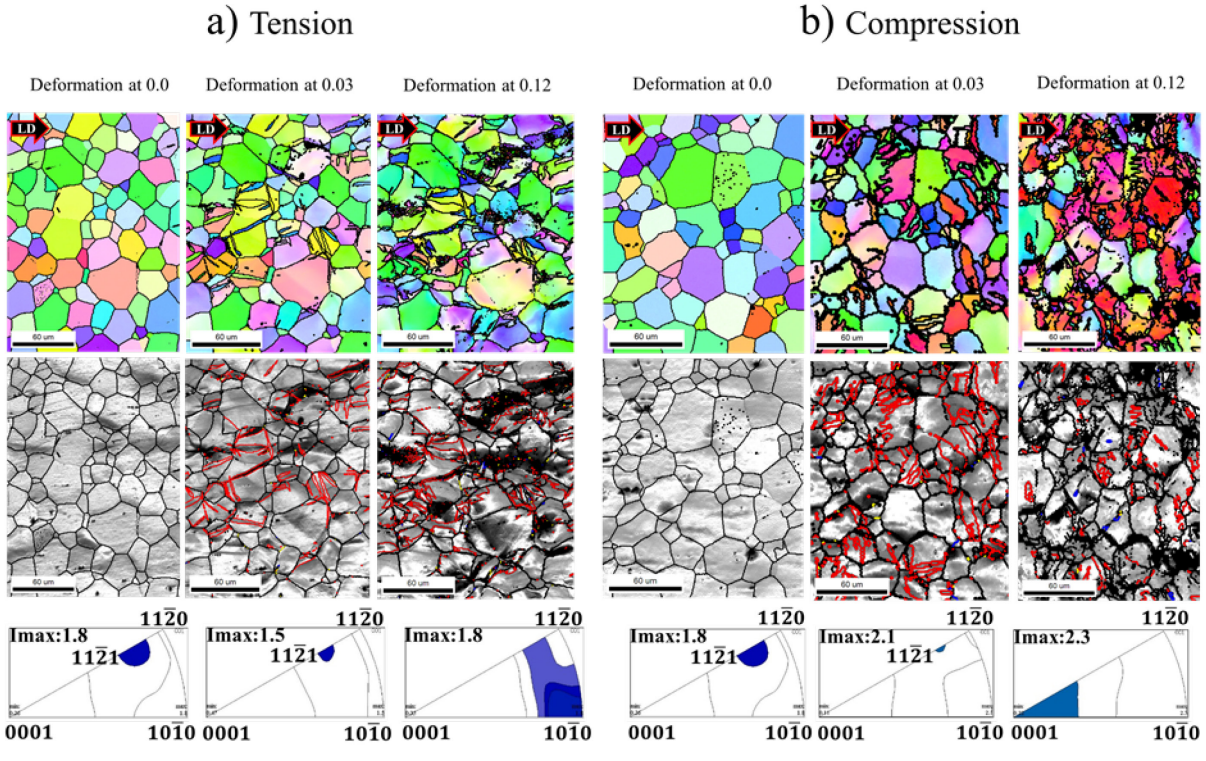

Twining type	(°)	Fraction at 0.03 deformation	Fraction at 0.12 deformation
Tension twin	86°	0.051	0.090
Compression twin	56°	0.001	0.002
Double twin	38°	------	0.001

Twining type	(°)	Fraction at 0.03 deformation	Fraction at 0.12 deformation
Tension twin	86°	0.075	0.111
Compression twin	56°	0.002	0.005
Double twin	38°	0.001	0.002

Figure 5.14. IPF maps (colorful figures) and IQ maps (gray figures) of ZNd10 alloy deformed in a) tension and b) compression. The twins are labeled in the IQ maps. The twinning fraction at each deformed microstructure is labeled by red, blue and yellow colors. The black arrow indicates the load direction (LD).

As with the previously observed evolution of the microstructure, an evolution of the crystallographic texture is also observed. Such texture evolution is shown in the subsequent figures.

Tested in tension, the Z1 alloy does not show a significant change in the crystallographic texture, this can be observed in figure 5.15a. Such a texture maintains its orientations located between $< 11\bar{2}0 >$ and $< 10\bar{1}0 >$ poles. Although there is a slight activation of twinning, that deformation mechanism did not produce big changes even at the deformation of 0.12.

Nevertheless, there is a slight tendency of some of the deformed grains to show orientations towards the $< 10\bar{1}0 >$ pole. M.T Perez Prado et al. [125] also observed the alignment of the crystal orientations towards the $< 10\bar{1}0 >$ pole during the tension of an AZ31 alloy.

On the other hand, during the uniaxial compression there is a major effect on the texture evolution, figure 5.15b. Here, a rotation of the HCP structure towards the $< 0001 >$ pole occurs. With the further deformation at 0.08, the basal planes are accommodated perpendicular to the direction of the applied force. This is because of the high activation of tensile twin since 0.03 of deformation (figure 5.12b). Amit Pandey et al. [126] reports similar findings in an AZ31 alloy tested in compression.
Thus, the observed difference in the crystallographic texture evolution of the Z1 alloy in this work, tested in tension or compression, is correlated to the easy activation of twinning in compression rather than in tension.

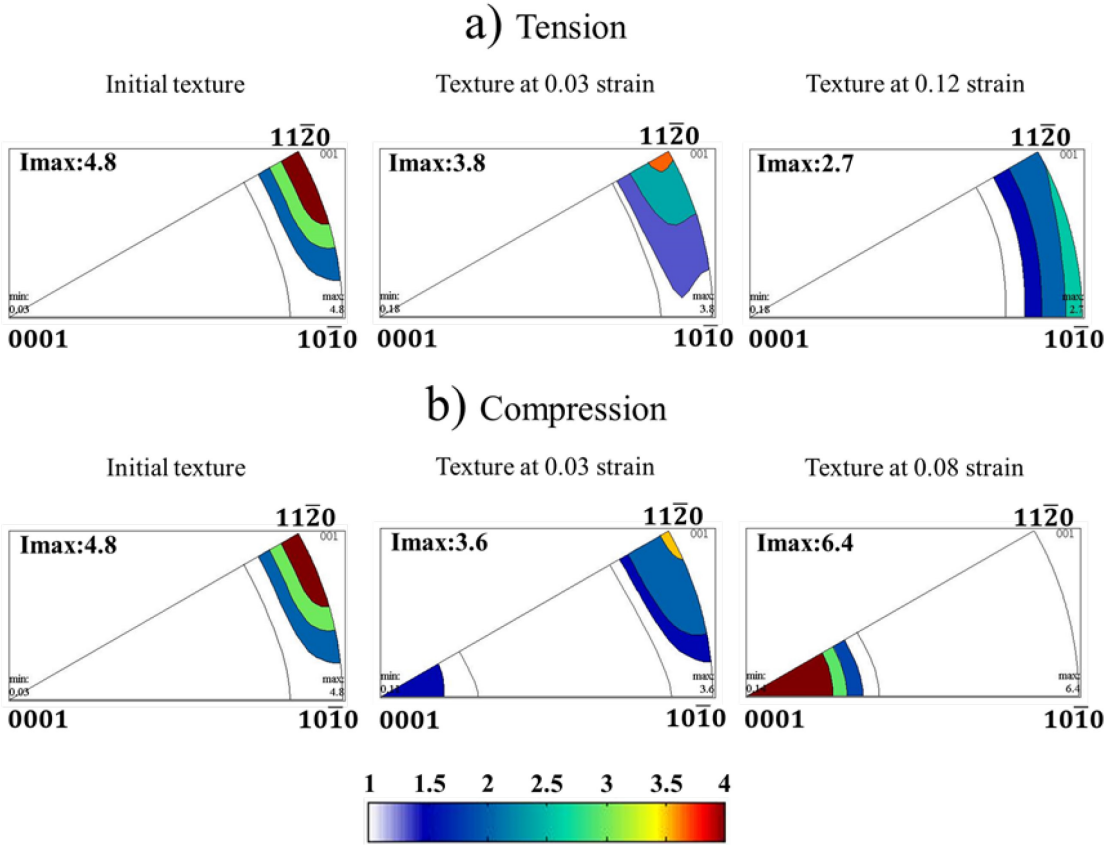

Figure 5.15. Inverse pole figures showing the crystallographic texture evolution in Z1 alloy tested in a) tension and b) compression. The texture intensity in the inverse pole figures is in the unit of m.r.d.

Twinning is also activated in the ZX10 alloy tested in tension, (as was displayed in figure 5.13a). Compared with the Z1 alloy, the fraction of twinning is slightly higher in the ZX10 alloy. Although there is observed the activation of twinning, it did not produce a marked effect on the crystallographic texture at low deformation of 0.03 (figure 5.16a). However, as the deformation increases to 0.12, there is a rotation towards the $< 10\bar{1}0 >$ pole (figure 5.16a). Then, there is a high tendency of the basal planes to be aligned parallel to the direction of the applied load. In compression, the activation of twinning is highly activated since 0.03 of deformation; however, the texture is quite comparable to the one without deformation, see

figure 5.16b. The compression up to 0.12 changes the orientation of the grains and most of them are aligned perpendicular to the applied load.

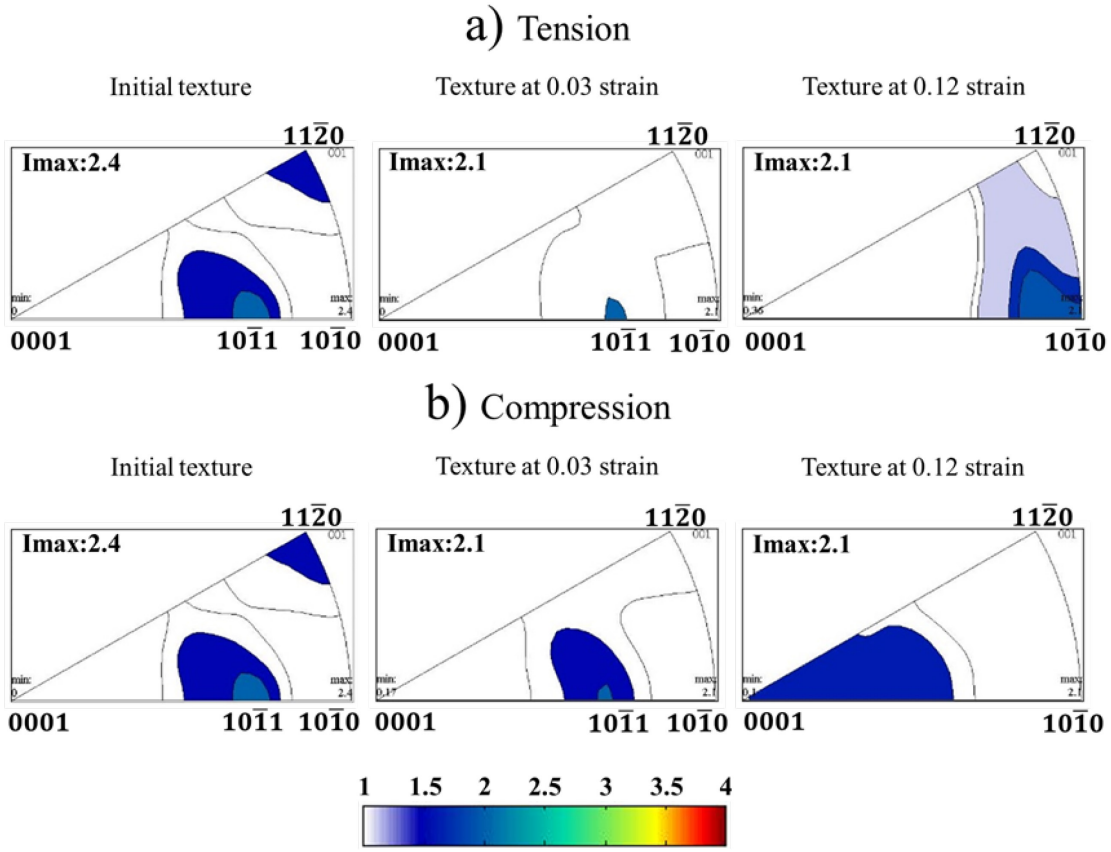

Figure 5.16. Inverse pole figures showing the crystallographic texture evolution in ZX10 alloy tested in a) tension and b) compression. The texture intensity in the inverse pole figures is in the unit of m.r.d.

Although at low fraction, during the deformation of ZNd10 alloy in tension, the twining mechanism is activated, (as was depicted in figure 5.14a). Nevertheless, the texture at 0.03 is similar to the initial one. Such twinning activation is not enough to modify the texture, i.e., the main texture component $< 11\bar{2}1 >$ remains at 0.03, figure 5.17a. The increment of applied load up to 0.12 produces a more visible texture modification. As in the ZX10, in the ZNd10 alloy, the grains are mainly orientated at the $< 10\bar{1}0 >$ pole. This can be correlated with the observed twinning activity at 0.12 of strain. Changing the direction of the applied load, i.e., in compression, although there is a high twinning activity, the main texture component $< 11\bar{2}1 >$ remains at 0.03, see figure 5.17b. The texture is highly modified at a strain of 0.12. There is a rotation towards the basal $< 0001 >$ pole.
In summary, tested in tension, both ternary alloys (ZX10 and ZNd10) have a similar behavior with the tendency to develop the prismatic $< 10\bar{1}0 >$ pole as the deformation proceeds. This also is in good agreement with earlier observations [127, 128], which showed the strengthening of $< 10\bar{1}0 >$ pole during the deformation under tension. This differs from the Z1 alloy where such a component is not clearly developed. In compression, the three alloys show a comparable crystallographic texture development, there is a trend for the basal $< 0001 >$ pole to be formed. In accordance with the present results, previous studies [123, 126, 128] have also shown the rotation towards the $< 0001 >$ pole.

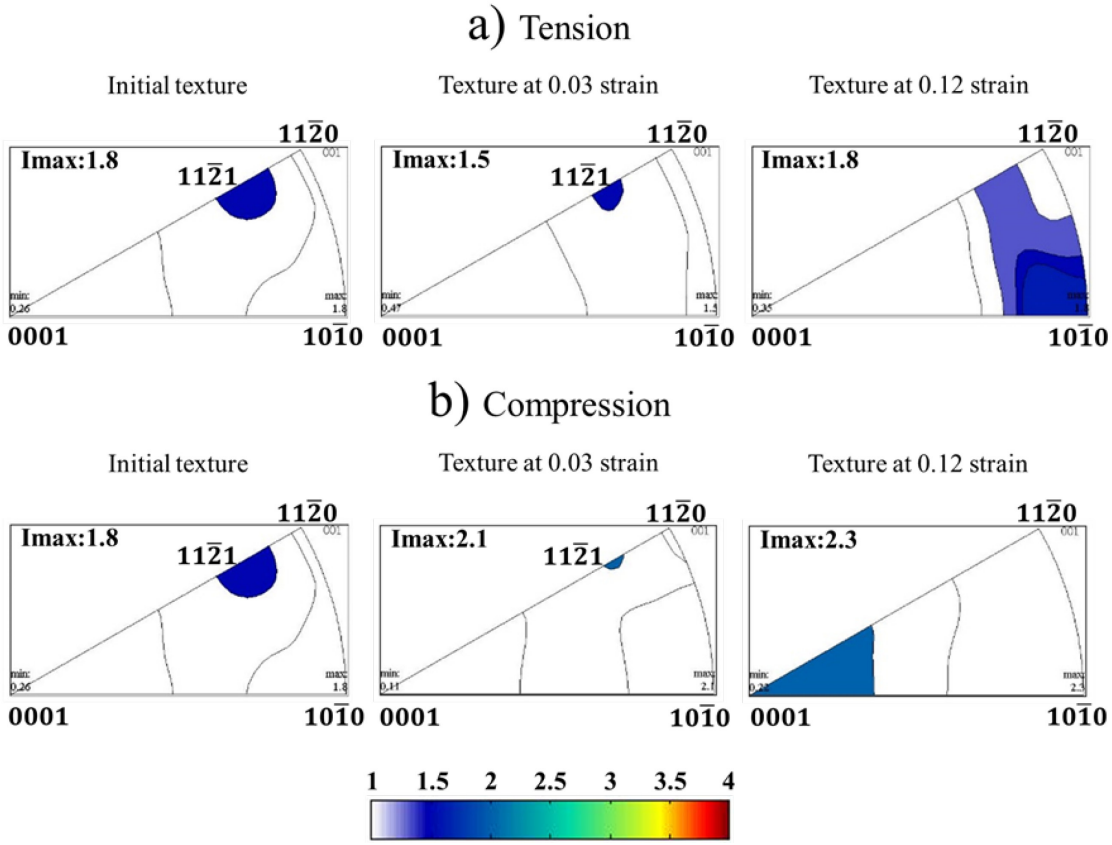

Figure 5.17. Inverse pole figures showing the crystallographic texture evolution in ZNd10 alloy tested in a) tension and b) compression. The texture intensity in the inverse pole figures is in the unit of m.r.d.

5.5.2 Experimental and VPSC modelling

In this section, experimental and simulated results are analyzed. The use of the VPSC model gives the possibility to associate the plastic behavior and the texture evolution during the deformation. Using the initial crystallographic texture of each alloy and applying the CRSS of each slip system in combination with the Voce parameters shown in tables 5.2 to 5.4 it is possible to simulate the hardening behavior in tension and compression as well as the corresponding crystallographic texture evolution. The experimental results and the VPSC simulations are compared in the following figures. The relative activities obtained during the simulation are also shown.

Table 5.2. CRSSs and strain hardening parameters of slip and twin systems considered in the simulation of Z1 alloy under tension and compression loading.

Slip mode	CRSS	τ_{sat}	θ_0	θ_1
Basal <a>	5.00	1.75	50.00	6.23
Prismatic <a>	13.05	5.11	200.00	6.53
Pyramidal <a>	75.22	47.28	495.65	0.43
Pyramidal I <c+a>	67.07	39.13	353.26	0.35
Pyramidal II <c+a>	33.04	39.24	3.37	0.05
Tensile twin $(10\bar{1}2)<10\bar{1}\,\bar{1}>$	5.43	0.00	0.00	0.00
Compressive twin $(10\bar{1}1) < 10\bar{1}\,\bar{2} >$	115.0	0.00	0.00	0.00

Table 5.3. CRSSs and strain hardening parameters of slip and twin systems considered in the simulation of ZX10 alloy under tension and compression loading.

Slip mode	CRSS	τ_{sat}	θ_0	θ_1
Basal <a>	5.00	6.85	12.28	50.10
Prismatic <a>	13.37	4.46	10.33	3.59
Pyramidal <a>	54.35	64.13	3.72	1.68
Pyramidal I <c+a>	22.28	53.26	2.61	0.22
Pyramidal II <c+a>	22.61	53.70	2.93	0.43
Tensile twin $(10\bar{1}2)<10\bar{1}\,\bar{1}>$	11.40	0.00	0.00	0.00
Compressive twin $(10\bar{1}1) < 10\bar{1}\,\bar{2} >$	112.0	0.00	0.00	0.00

Table 5.4. CRSSs and strain hardening parameters of slip and twin systems considered in the simulation of ZNd10 alloy under tension and compression loading.

Slip mode	CRSS	τ_{sat}	θ_0	θ_1
Basal <a>	5.00	9.78	14.30	55.87
Prismatic <a>	11.96	4.89	10.76	3.80
Pyramidal <a>	47.17	65.22	3.39	1.36
Pyramidal I <c+a>	21.20	52.72	2.35	0.23
Pyramidal II <c+a>	22.28	53.26	2.72	0.45
Tensile twin $(10\bar{1}2)<10\bar{1}\,\bar{1}>$	12.59	0.00	0.00	0.00
Compressive twin $(10\bar{1}1) < 10\bar{1}\,\bar{2} >$	109.0	0.00	0.00	0.00

The experiments and simulations carried out give an understanding of the active deformation modes that take place during tension and compression. According to the VPSC simulation in tension, at the onset of deformation of the Z1 alloy (figure 5.18c), the deformation is dominated by basal slip up to roughly 0.027 of strain. As the deformation proceeds, basal <a> slip decreases and the prismatic <a> slip begins to dominate the deformation up to 0.12. Tensile twinning is also activated right at the beginning. This is also observed in the IQ map in figure 5.12a. The findings regarding the relative activities in tension of this Z1 alloy agree with the reported results by [129] in which a rolled sheet of Z1 was tested in tension along the rolling direction.

In compression, the tensile twinning mode dominates at the onset of the deformation; figure 5.18d. In this case, the twinning takes much more relevance during this kind of deformation; this is confirmed with the observed on the IPF map (figure 5.12b). At higher strains, the twinning activity decreases and basal <a> slip becomes dominant. In reference to the non-basal deformation modes, there is a low activation of the prismatic <a> slip and pyramidal II <c+a> at the end of the deformation. In a extruded AZ31 alloy, with a basal texture comparable to the observed in the Z1 alloy, Ebeling et al. [105] reported a similar behavior with respect to tensile twining and basal slip like the one reported in this work. However, the observed activity of pyramidal mode in this work, contrasts with the observed inactivity reported by Ebeling's work.

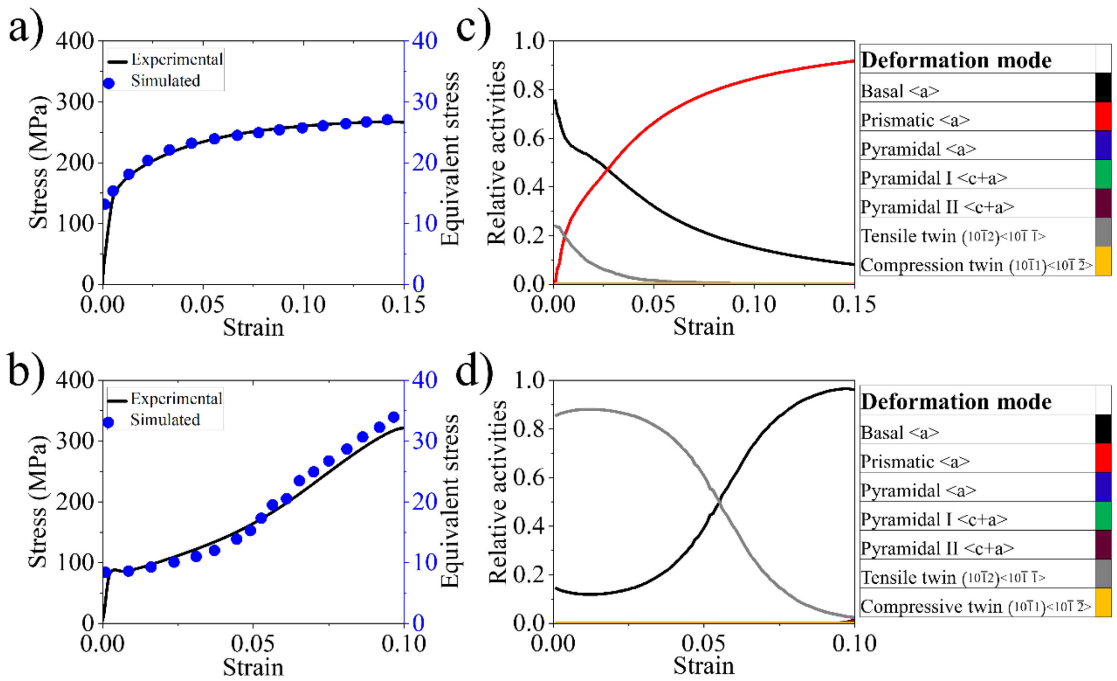

Figure 5.18. Experimental and simulated uniaxial a) tension and b) compression curves for Z1 alloy. Estimated relative activities of the seven deformation modes considered during c) tension and d) compression simulations.

The activity of deformation modes observed in the ZX10 alloy differs from tension to compression. For this alloy, both, basal <a> and prismatic <a> slip dominate the deformation in tension (figure 5.19c). A slight tensile twining activity is also observed. This agrees with the low twinning fraction determined by the EBSD analysis (figure 5.13a). In this ZX10 alloy, the lower twinning mode activity could be attributed to the non-basal texture that promotes more activation of non-basal modes. The simulation findings shown in this work demonstrate the activation of non-basal slip, e.g., prismatic <a> slip even at room temperature, this has been also reported previously [105, 129, 130]. Furthermore, the simulation in this work suggests the activity of pyramidal modes, where there is a higher activity of pyramidal <a> if compare with pyramidal <c+a> slip. Such deformation mode, i.e., pyramidal <a> is observed since a strain of 0.095 and slightly increases at the end of deformation. However, the pyramidal <a> slip activity in this work is lower than the reported for a binary Mg-Ca alloy [131].

On the other hand, in compression, the deformation is practically dominated by basal <a> slip, see figure 5.19d. In this case, the tensile twinning is activated since the beginning of deformation as well as its activation is pronounced. This is also observed on the EBSD analysis (figure 5.13b). The activation of prismatic slip is quite low, and it is slightly visible at the highest deformation. It was found that all the considered pyramidal modes are similarly activated. This was found particularly at high deformation. The inactivity of prismatic <a> slip at the onset of deformation in compression has been also observed in [105]. However, a difference arises in the present work, where such a deformation mode is activated especially at the end of deformation.

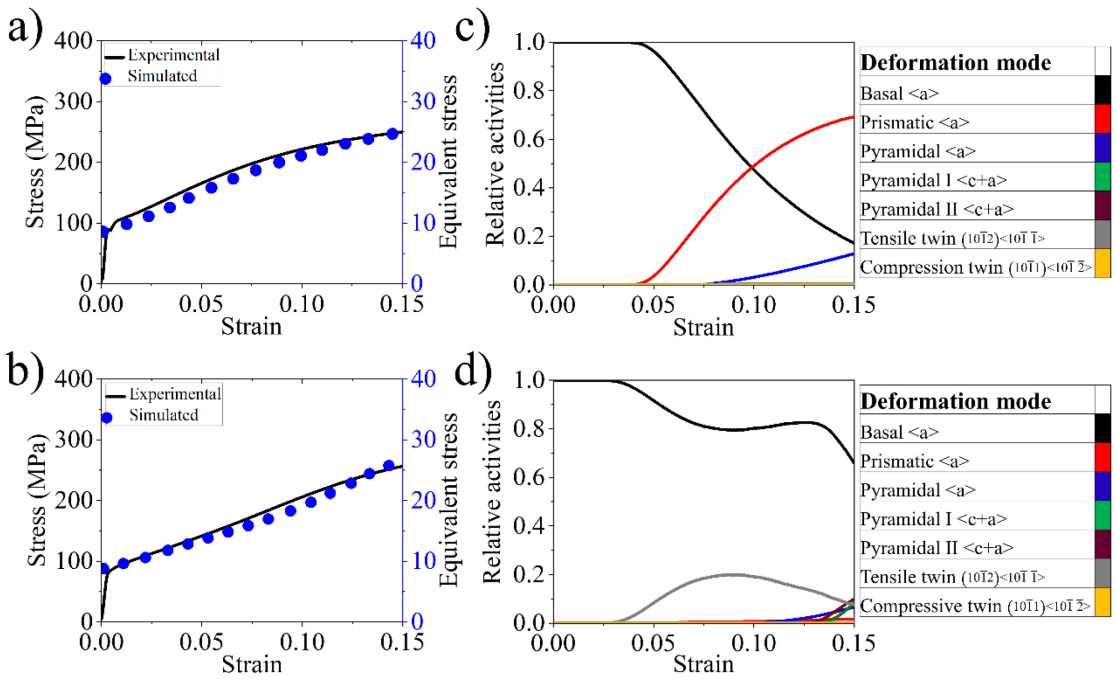

Figure 5.19. Experimental and simulated uniaxial a) tension and b) compression curves for ZX10 alloy. Estimated relative activities of the seven deformation modes considered during c) tension and d) compression simulations.

As in the previous alloy, in the ZNd10 alloy, the deformation under tension is dominated by basal <a> and prismatic <a> slip modes; see figure 5.20c. Although the basal <a> deformation mode is highly important at the start of deformation, it becomes less activated at around 0.080 of strain since the prismatic <a> mode starts to dominate the deformation. In this case, the considered tensile twinning is slightly more activated than in the ZX10 alloy. The pyramidal <a> slip is activated. Its activation is slightly higher than in the previous ZX10 alloy. The activation of basal <a> and prismatic <a> deformation modes in this study corroborates earlier findings published by Zhou et al. [129] for a similar alloy. As well in [129], the pyramidal II <c+a> mode is proposed as the one involved in the deformation along the *c*-axis, nevertheless in the present work, it is suggested that there is a higher activation of pyramidal <a> than of pyramidal II <c+a> slip. A higher activity of pyramidal <a> in comparison to pyramidal <c+a> mode was also found by Zeng et al. [131] for a binary Mg-Nd alloy.

In compression, the activity of the different deformation modes is quite different, especially the non-basal modes and the tensile twinning, figure 5.20d. Firstly, the basal <a> slip is activated from the start of deformation, which decreases as the deformation proceeds. The activation of tensile twinning is more pronounced in compression rather than in tension. Based on the relative activity of deformation modes, figure 5.20d, there is a clear activation of pyramidal <a> slip from roughly 0.070 of strain. At a strain of 0.12, the activation of pyramidal I and pyramidal II slip is quite comparable. In relation to the compression of a Mg-Li-Al alloy, Lentz et al. [132] suggest a deformation dominated by prismatic <a> slip followed by tensile twinning and to a smaller extent by basal <a> slip, this contrasts with the finding reported here (figure 5.20d). This discrepancy can be correlated with the non-basal texture observed this Mg-Zn-Nd alloy.

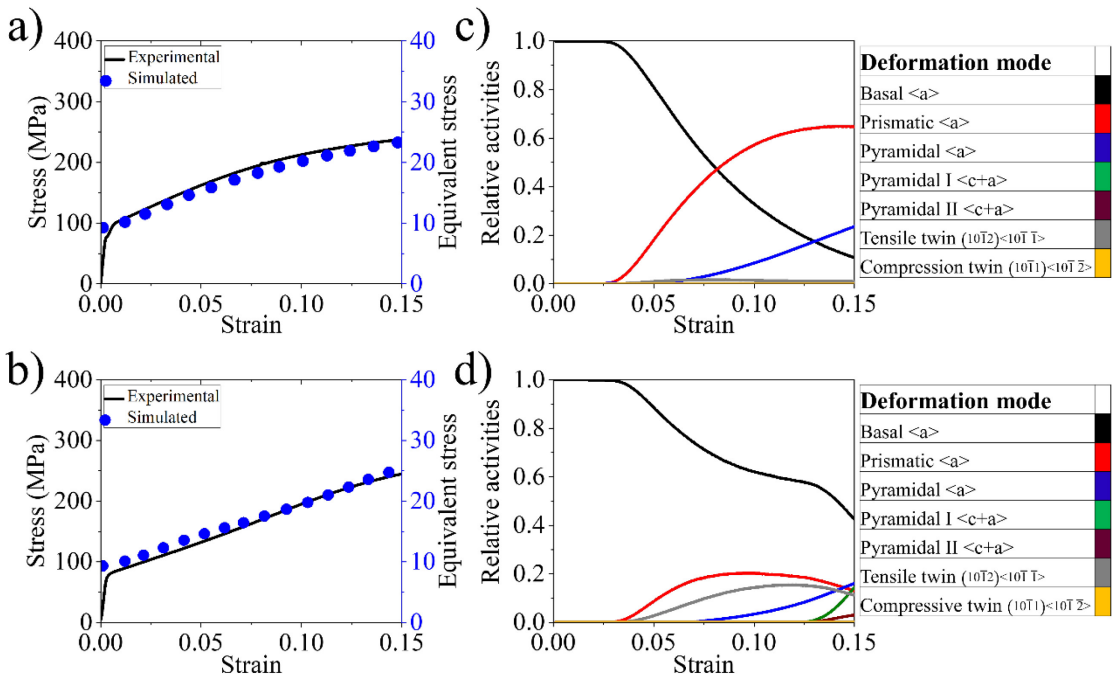

Figure 5.20. Experimental and simulated uniaxial a) tension and b) compression curves for ZNd10 alloy. Estimated relative activities of the seven deformation modes considered during c) tension and d) compression simulations.

5.5.3 Effect of Ca and Nd additions on the CRSS ratio of deformation modes

Figure 5.21 displays the ratio between the CRSS of each deformation mode considering the VPSC simulations. The addition of Ca or Nd into the Mg-Zn systems modifies the relation between the critical resolved shear stresses of the slip modes. Based on the VPSC simulation, the ratio between the $CRSS_{prismatic<a>}$ slip and the $CRSS_{basal<a>}$ slip is 2.61 in the Z1 alloy. Regarding to the ZX10 alloy, such ratio corresponds to 2.68. In reference to the ZNd10 alloy, the ratio between the $CRSS_{prismatic<a>}$ slip and the $CRSS_{basal<a>}$ slip is 2.40. The previous observed CRSS ratios show the relevance of the alloying elements on magnesium, where these values are lower than the reported for pure magnesium [133, 134].

The balance among the basal <a> and pyramidal modes is also modified. Then, the ratio between $CRSS_{pyramidal\ <a>}$ and $CRSS_{basal<a>}$ slip is 15.04, 10.90 and 9.43 for the Z1, ZX10 and ZNd10 alloy, respectively. The estimated $CRSS_{pyramidal\ <a>}/CRSS_{basal<a>}$ for the alloys in this work contrasts with Zeng et al. [131], where it was estimated a $CRSS_{pyramidal\ <a>}/CRSS_{basal<a>}$ of 18.0 for a AZ31 alloy, while 4.33 in an Mg-Ca alloy and 3.75 for a Mg-Nd alloy. Moreover, in the present work the ratio between $CRSS_{pyramidal\ I\ <c+a>}$ and $CRSS_{basal<a>}$ slip is evaluated in 13.41, 4.46, 4.24 for the Z1, ZX10 and ZNd10 alloy, respectively. A $CRSS_{pyramidal\ I<c+a>}/CRSS_{basal<a>}$ of 24.0, 5.33 and 4.75 were estimated for the AZ31, Mg-Ca and Mg-Nd alloys, respectively in [131].
The $CRSS_{pyramial\ II\ <c+a>}$ slip /$CRSS_{basal<a>}$ slip corresponds to 6.61, 4.52 and 4.46 for Z1, ZX10 and ZNd10 alloy, respectively. For the binary Z1 alloy, the CRSS ratio is slightly higher in comparison with the estimated from the work by Zhou et al. [129]. In the specific case of the Mg-Zn-Ca alloy, the CRSS ratio between the $CRSS_{pyramdial\ II\ <c+a>}$ and the $CRSS_{basal<a>}$ has not been assessed. The alloy that can be comparable corresponds to the Mg-Zn-Nd. Perez-Prado et al. [135] determined for a Mg-Zn-Nd alloy, a smaller CRSS ratio when compared with the

reported in this work. Furthermore, from the considered deformation twinning, the $CRSS_{tensile\text{-}twinning}$ is the most affected with respect to the $CRSS_{basal<a>}$. Then, the $CRSS_{tensile\text{-}twinning}/CRSS_{basal<a>}$ in the Z1 alloy corresponds to 1.10, such ratio is changed to 2.28 in the ZX10 alloy and to 2.52 in the ZNd10 alloy. The findings showed a similar trend in comparison with [131].

In figure 5.21 a summary of the ratio between the CRSS of non-basal slip and the CRSS of the extension twinning both with respect to CRSS of the basal is shown. The $CRSS_{prismatic}/CRSS_{basal<a>}$ increases with the addition of Ca into the Mg-Zn system but decreases with the addition of Nd. In the case of the pyramidal modes, all of them follow a similar behavior. Then, the $CRSS_{pyramidal\ <a>,\ I\ and\ II\ <c+a>}/CRSS_{basal<a>}$ reduces with the addition of Ca and is even lower with the addition of Nd. Regarding the $CRSS_{extension\text{-}twinning}/CRSS_{basal<a>}$, it follows an opposite trend, that means, the addition of Ca to the Z1 alloy increases the ratio and with the addition of Nd, the ratio is further increased.

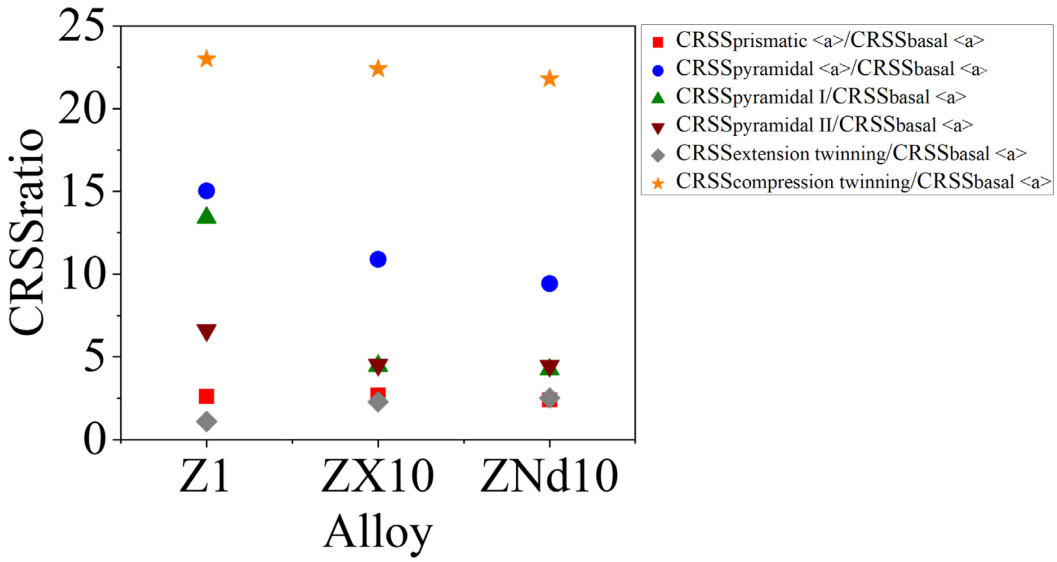

Figure 5.21. Ratio between the $CRSS_{non\text{-}basal}$ slip and $CRSS_{basal<a>}$ slip as well as the ratio between the $CRSS_{extension\ twinnig}$ and $CRSS_{basal<a>}$ slip based of the VPSC simulations.

5.5.4 Crystallographic texture evolution: Experimental and simulated

Figure 5.22 presents the experimental and simulated inverse pole figures for the Z1 alloy during the deformation under tension and compression. The compared experimental and simulated crystallographic texture are in good agreement either in tension or in compression (see figure 5.22). The simulation results in tension presented particularly the dominance of two deformation modes, that is, the decreasing activity of basal <a> slip combined with the increasing activity of prismatic <a> slip as the strain proceeds. The activity of these two deformation modes generates a suggested rotation around the *c*-axis of the HCP structure, which aligns the basal planes between the $< 11\bar{2}0 >$ and $< 10\bar{1}0 >$ pole with a high intensity in the surroundings of the $< 10\bar{1}0 >$ pole, see figure 5.22a. In a previous study, evaluating the texture evolution during plastic deformation by simulation in tension of AZ31 alloy [105] reported consistent results with the findings in this work. In addition, the higher texture intensity in comparison with the simulated texture has been also reported in Z1 alloy in [129]. On the other hand, in compression, most of the *c*-axes align perpendicular to the applied load. Such alignment favors the formation of basal $< 0001 >$ pole, figure 5.22b.

This texture component can be correlated with the dominance of basal <a> slip and tensile twinning, where the latter is highly activated since the onset of deformation. The extension twinning is an important deformation mechanism that leads to fast and quite clear texture developments. This finding broadly agrees the simulation work for an extruded AZ31 alloy [105], linking the activity, principally of extension twin and basal <a> deformation modes in compression with the texture development.

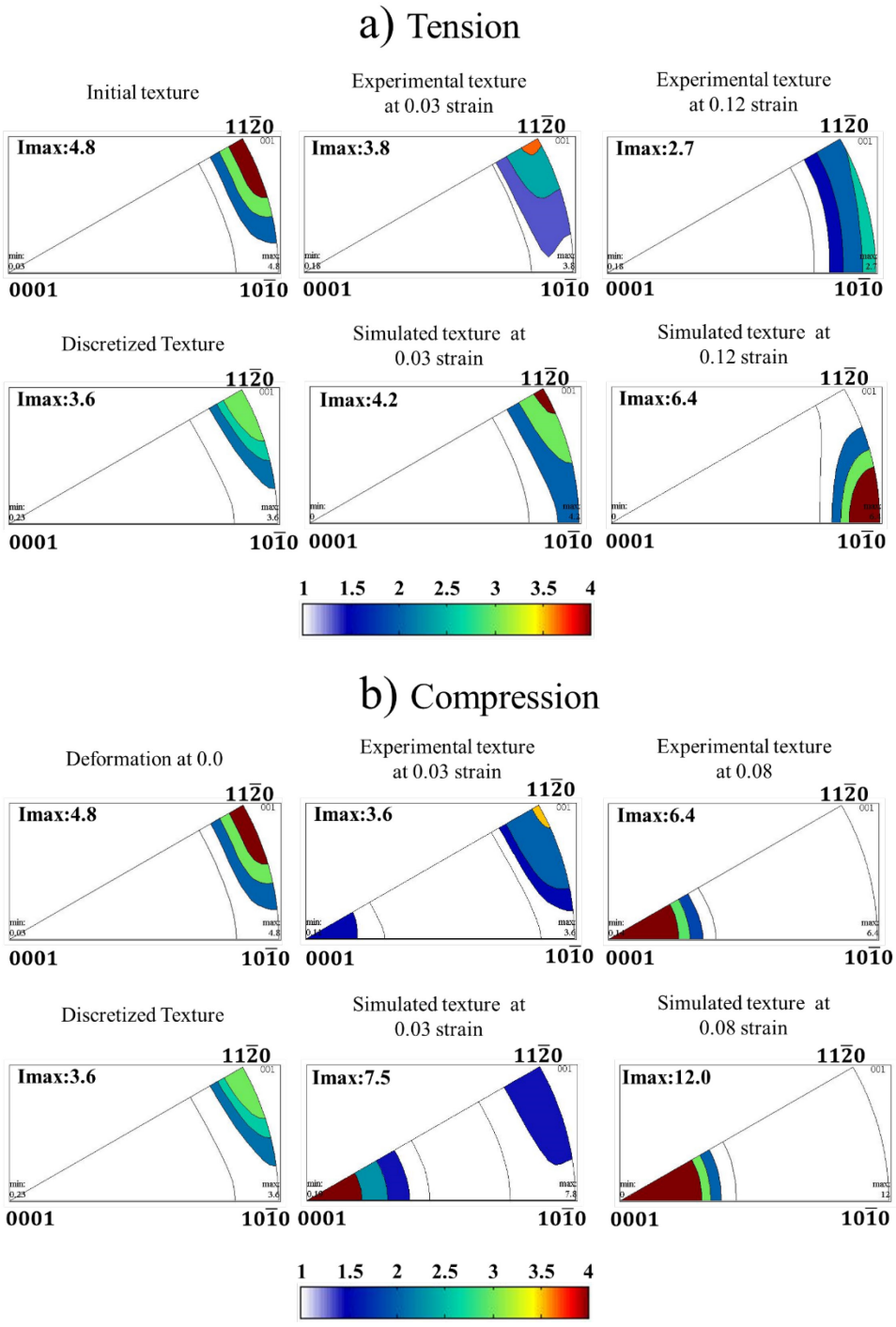

Figure 5.22. Inverse pole figures comparing the experimental and simulated crystallographic texture of Z1 alloy tested under a) tension and b) compression. The texture intensity is in the unit of m.r.d.

Figure 5.23 shows the crystallographic texture evolution of ZX10 observed experimentally and in simulation. Both, the experimental and simulated textures are in good agreement. As in the Z1 alloy, the basal <a> and prismatic <a> slip dominate the deformation when the alloy is tested in tension. However, the initial texture observed in the ZX10 alloy promotes the dominance of the basal <a> slip until a higher deformation strain (at roughly 0.10) compared with the Z1 alloy. Nevertheless, the prismatic <a> slip dominates the deformation particularly at the end of the deformation.
Additionally, the pyramidal <a> mode, it was slightly activated for this ZX10 alloy at the final strain stage. Therefore, in tension, the rotation of the component $< 10\bar{1}1 >$ towards the development of the prismatic $< 10\bar{1}0 >$ pole can be attributed to the prismatic <a> slip, that starts to dominate the deformation from 0.10 of strain, see figure 5.23a. Lentz et al. [132] also observed an enhancement of the prismatic texture component in an Mg-Zn-Al alloy during the deformation in tension, as a consequence of the predominant activation of prismatic <a> mode.

The texture evolution in compression (figure 5.23b) is determined by the distinct balance of deformation mechanisms, where such a balance is quite different if compare with tension.
Basal <a> slip and tensile twinning accomplish the deformation in compression predominantly. Therefore, the dominance of basal <a> slip in combination with a high activation of tensile twining mode leads to the rotation of the $< 10\bar{1}1 >$ pole towards the $< 0001 >$ pole.

Furthermore, regarding the non-basal deformation modes, it seems that the prismatic <a> slip is not activated while the pyramidal <a> slip is observed from approximately 0.10 of strain. The activation of the pyramidal <a> generates a rotation of the <c> axis towards the load compression [136]. Then, such rotation also contributes to the formation of the $< 0001 >$ pole. The rotation towards the formation of basal $< 0001 >$ pole in compression agrees with that determined for an AZ31 alloy [105], where the plastic deformation is predominantly accomplished by tensile twinning and basal <a> mode. However, in the present work, in addition to the activation of such deformation modes, the pyramidal mode family also influences to some extent the texture development.

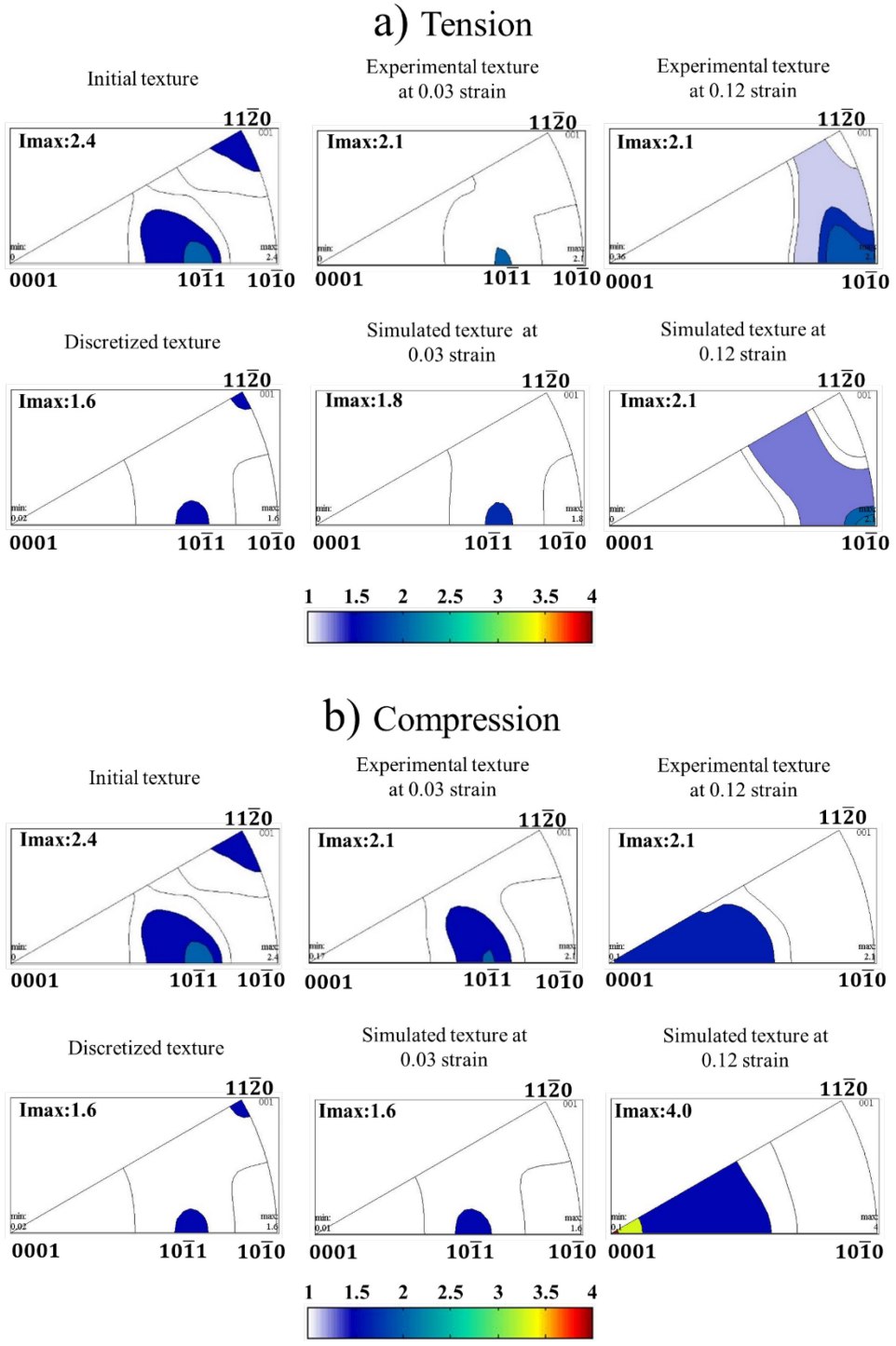

Figure 5.23. Inverse pole figures comparing the experimental and simulated crystallographic texture of ZX10 alloy tested under a) tension and b) compression. The texture intensity is in the unit of m.r.d.

There is a good agreement between the experimental and simulated crystallographic texture for the ZNd10 alloy as can be seen in figure 5.24. Figure 5.24a shows the rotation of the rare earth component $< 11\bar{2}1 >$ towards the prismatic $< 10\bar{1}0 >$ pole when the alloy is tested under tension. This is associated to the dominance of basal <a> and prismatic <a> modes.

Where the prismatic <a> slip starts to play a predominant role from approximately 0.08 until the end of the deformation. The initial texture as the one observed in the ZNd10 alloy, promotes the activation of tensile twinning (which is slightly higher than in ZX10 alloy) and pyramidal <a> slip as well. The activation of these two last deformation modes is also contributing to the formation of $< 10\bar{1}0 >$ pole.
According to the present results, in the ZNd10 alloy, the formation of the $< 10\bar{1}0 >$ pole requires a higher activity of prismatic <a> slip as well as a slightly higher activity of pyramidal <a> slip if compare with ZX10 alloy. This finding is also in agreement with earlier observations [137, 138], which showed the development of the prismatic component after tension, due to a high activity of prismatic <a> mode followed by basal <a> mode.

Figure 5.24b displays the experimental and simulated crystallographic texture of the alloy tested under compression. In compression, the basal <a> and prismatic <a> slip as well as extension twin are the most activated deformation modes. However, the activity of basal <a> slip drops down fast. It is well known that twinning produces a reorientation of the matrix, and such reorientation activates different deformation modes. Then, the observed activation of prismatic <a> slip and the relative activity of pyramidal <a> slip is associated with the high activation of extension twin, which is visible from the onset of deformation.

In addition, a small relative activity of pyramidal I <c+a> and pyramidal II <c+a> is predicted. Therefore, the formation of the basal $< 0001 >$ pole (figure 5.24b) which comes from the rotation of the $< 11\bar{2}1 >$ pole, it can be correlated to the activity of basal <a> slip in combination with prismatic <a> slip as well as a certain contribution of pyramidal <a> slip. The observed texture development in this work was also reported by Lentz et al. [137]. In that work, the texture evolution is associated predominantly to the activity of basal <a> mode, followed by tensile twin and prismatic <a> mode. As opposed to the results reported in [137], in the present work it is also suggested that a small activation of pyramidal I <c+a> and pyramidal II <c+a> modes also have a certain role in the texture formation.

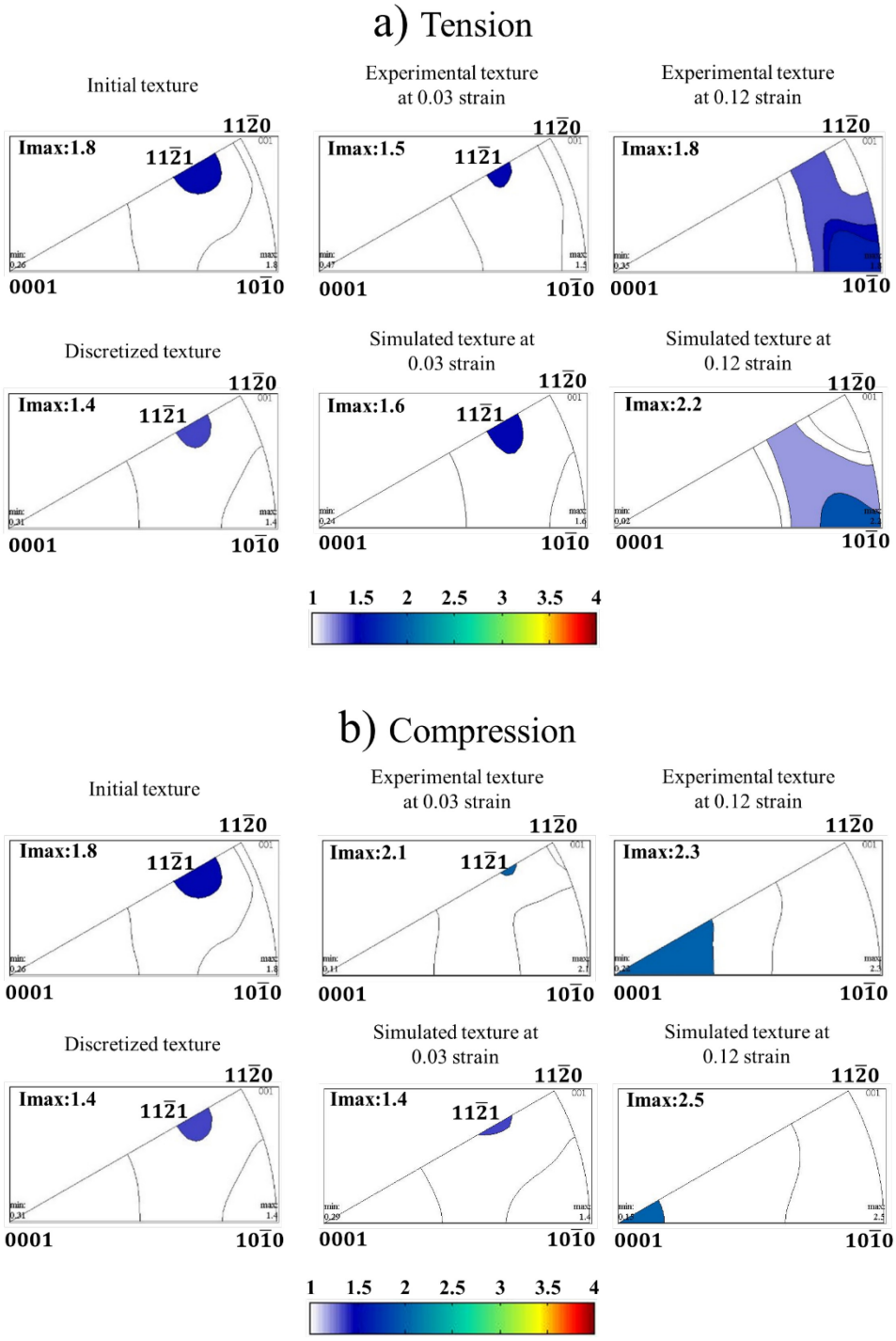

Figure 5.24. Inverse pole figures comparing the experimental and simulated crystallographic texture of ZNd10 alloy tested under a) tension and b) compression. The texture intensity is in the unit of m.r.d.

5.5.5 Ex-situ deformation

In this section, a detailed analysis of the possible deformation modes is given using *ex-situ* tension and compression tests. To develop this goal, slip trace analyses were done on ex-situ measurements. The slip traces are the result of high-localized slip activity. During the deformation either in tension or in compression, owing to slip on specific crystallographic planes, steps can be formed that appear as lines on the sample surface when it is observed in the SEM or LSM. In this work, pictures from LSM are used.

The estimation of the slip activity through this methodology sometimes disregards the observation of some deformation systems. Some facts complicate the visibility of the deformation modes. Those deformation systems with Burgers vector parallel to the sample surface will not develop visible traces [139]. Due to the nature of the constraints differing, the activity of deformation systems at the surface likely does not reflect the activity inside, and consequently, the activation of the different deformation modes is affected. Additionally, at small magnitudes of slip, the slip bands will not be developed. Therefore, it is probable that not all the slip traces will be visible, and consequently, not all the deformation modes can be detected. Even so, an effort has been made to distinguish the appearance of slip traces in as many grains as possible. The dislocation behavior in magnesium alloys has been studied previously by surface slip trace analysis [140-144].

In this work, the slip trace analysis has been performed under tension at 0.03 and 0.12 of strain in the three alloys. Under compression, the analysis was done at 0.03 and 0.08 of strain on the Z1 alloy, and at 0.03 and 0.12 on the ZX10 and ZNd10 alloys.

Figure A3 and A4 from appendix show examples of grains where slip lines are developed in the alloy Z1. In the aforementioned figures, example of each considered deformation mode during the tests in tension and in compression are shown. As an important parameter, the Schmid factor is frequently estimated to analyze the possibility of the activation of deformation modes. Table 5.5 displays the estimated Schmid factors of the considered slip systems for the exemplified grains that showed slip traces in Z1 alloy (figures A3 and A4 from appendix).

According to the table below, among the three basal slip systems the closest one to the slip line developed in tension is the $(0001) < 2\bar{1}\bar{1}0 >$ while in compression is the $(0001) < \bar{1}\bar{1}20 >$. From the prismatic slip systems, the $(10\bar{1}\bar{0}) < \bar{1}2\bar{1}0 >$ is activated in tension while the $(0\bar{1}10) < 2\bar{1}\bar{1}0 >$ is activated in compression. Regarding the pyramidal <a>, the $(01\bar{1}\bar{1}) < 2\bar{1}\bar{1}0 >$ is activated in tension and the $(0\bar{1}11) < 2\bar{1}\bar{1}0 >$ in compression. In reference to the pyramidal I <c+a>, the $(10\bar{1}\bar{1}) < \bar{2}113 >$ is activated in tension while the $(0\bar{1}11) < \bar{1}2\bar{1}3 >$ is activated in compression. Finally, from the pyramidal II <c+a>, the $(\bar{2}112) < \bar{2}11\bar{3} >$ is activated in tension and in compression the $(\bar{1}2\bar{1}2) < \bar{1}2\bar{1}3 >$.

Table 5.5. Estimated Schmid factors of the slip systems in exemplified grains showing slip traces in Z1 alloy. The Schmid factor of the activated slip systems are in bold for each grain.

Slip system number	Grains showing slip lines in tension					Slip system number	Grains showing slip lines in compression				
	Basal <a>	Prismatic <a>	Pyramidal <a>	Pyramidal I <c+a>	Pyramidal II <c+a>		Basal <a>	Prismatic <a>	Pyramidal <a>	Pyramidal I <c+a>	Pyramidal II <c+a>
1	**0.4833**	0.0667	0.1071	0.0559	0.0028	3	**0.4045**	0.3097	0.1030	0.0437	0.4441
4	0.2261	**0.4305**	0.3594	0.4215	0.4555	5	0.1245	**0.0652**	0.3510	0.0029	0.2433
11	0.1678	0.4009	**0.4551**	0.0091	0.0475	8	0.2727	0.2032	**0.4669**	0.0571	0.0171
14	0.3205	0.1124	0.1274	**0.4260**	0.0092	16	0.4744	0.4751	0.0318	**0.3971**	0.0168
27	0.1163	0.1266	0.1813	0.4189	**0.0012**	35	0.3035	0.3796	0.3511	0.4734	**0.2193**

Table 5.6 displays the estimated Schmid factors of the considered slip systems for the exemplified grains that showed slip traces in ZX10 alloy (figures A5 and A6 from appendix).

Among the basal slip systems, the slip line developed in tension and in compression is correlated to the activation of the slip system$(0001) < \overline{1}\overline{1}20 >$. In reference to the prismatic slip systems, the $(\overline{1}100) < \overline{1}\overline{1}20 >$ is activated both in tension and compression. The pyramidal <a>, i.e., the $(01\overline{1}\overline{1}) < 2\overline{1}\overline{1}0 >$ is activated in tension and in compression. In reference to the pyramidal I <c+a>, the $(01\overline{1}\overline{1}) < 1\overline{2}13 >$ is activated in tension while the $(10\overline{1}\overline{1}) < \overline{2}113 >$ is activated in compression. Finally, from the pyramidal II <c+a>, the $(\overline{2}112) < 2\overline{1}\overline{1}3 >$ is activated in tension and in compression the $(\overline{1}\overline{1}22) < \overline{1}\overline{1}2\overline{3} >$.

Table 5.6. Estimated Schmid factors of the slip systems in exemplified grains showing slip traces in ZX10 alloy. The Schmid factor of the activated slip systems are in bold for each grain.

Slip system number	Grains showing slip lines tension					Slip system number	Grains showing slip lines compression				
	Basal <a>	Prismatic <a>	Pyramidal <a>	Pyramidal I <c+a>	Pyramidal II <c+a>		Basal <a>	Prismatic <a>	Pyramidal <a>	Pyramidal I <c+a>	Pyramidal II <c+a>
3	**0.2935**	0.1005	0.3899	0.4382	0.1387	3	**0.4678**	0.0904	0.0711	0.2510	0.2258
6	0.0104	**0.1782**	0.2090	0.0425	0.2805	6	0.1736	**0.0590**	0.1378	0.3871	0.4317
11	0.4205	0.0090	**0.2115**	0.1534	0.0696	11	0.4121	0.2974	**0.4030**	0.0866	0.0608
22	0.0153	0.0079	0.0504	**0.4610**	0.0506	14	0.2739	0.2188	0.2424	**0.4393**	0.0438
28	0.1297	0.3953	0.0275	0.2404	**0.4508**	31	0.2106	0.2641	0.1124	0.0669	**0.1354**

Table 5.7 displays the estimated Schmid factors of the considered slip systems for the exemplified grains that showed slip traces in ZNd10 alloy (figures A7 and A8 from appendix). In this alloy, among the three basal slip systems, the slip line developed in tension is associated to the slip system $(0001) < \overline{1}2\overline{1}0 >$ while in compression is the $(0001) < \overline{1}\overline{1}20 >$. From the prismatic slip systems, the $(0\overline{1}10) < 2\overline{1}\overline{1}0 >$ is activated in tension while the $(\overline{1}100) < \overline{1}\overline{1}20 >$ is activated in compression. In relation to the pyramidal <a>, the $(\overline{1}101) < \overline{1}\overline{1}20 >$ is activated in tension and the $(0\overline{1}11) < 2\overline{1}\overline{1}0 >$ in compression. In reference to the pyramidal I <c+a>, the $(0\overline{1}11) < 11\overline{2}3 >$ is activated in tension while the $(1\overline{1}01) < \overline{1}2\overline{1}3 >$ is activated in compression. Finally, from the pyramidal II <c+a>, the $(11\overline{2}2) < 11\overline{2}3 >$ is activated in tension and in compression the $(1\overline{2}12) < 1\overline{2}1\overline{3} >$.

Table 5.7. Estimated Schmid factors of the slip systems in exemplified grains showing slip traces in ZNd10 alloy. The Schmid factor of the activated slip systems are in bold for each grain.

Slip system number	Grains showing slip lines tension					Slip system number	Grains showing slip lines compression				
	Basal <a>	Prismatic <a>	Pyramidal <a>	Pyramidal I <c+a>	Pyramidal II <c+a>		Basal <a>	Prismatic <a>	Pyramidal <a>	Pyramidal I <c+a>	Pyramidal II <c+a>
2	**0.4431**	0.1738	0.0474	0.3686	0.2760	3	**0.4740**	0.1889	0.0507	0.0395	0.4628
5	0.3498	**0.4832**	0.3654	0.0024	0.2753	6	0.1082	**0.4510**	0.0537	0.0025	0.0403
9	0.1450	0.2301	**0.4306**	0.1194	0.0962	8	0.0161	0.2860	**0.3896**	0.0349	0.1856
15	0.2327	0.1499	0.0058	**0.0170**	0.1923	24	0.3784	0.2045	0.2621	**0.4366**	0.2357
25	0.0006	0.0078	0.3563	0.3140	**0.0843**	29	0.1965	0.0430	0.2349	0.4596	**0.3780**

After tension and compression tests, the statistics of the identified grains with slip lines is reported for each alloy in the pictures 5.25 to 5.27 as well as in the tables 5.8 and 5.9.
The results on the slip trace analysis show a dominance of the basal <a> on the Z1 alloy since the beginning of the deformation either in tension or in compression see figure 5.25. The prismatic <a> slip is also important during the deformation. During tension, as the deformation proceeds, the amount of prismatic <a> slip increases, see figure 5.25a. In contrast, during the deformation in compression the amount of such slip mode is low, see figure 5.25b. Regarding to the activation of pyramidal <a>, pyramidal I <c+a> and pyramidal <c+a> II modes, it was

quite hard to be observed in this Z1 alloy during the deformation. Nevertheless, some grains were observed showing slip lines corresponding to the pyramidal slip family. The amount of this kind of deformation modes is rather low when the alloy is tested in tension, see figure 5.25a. In contrast, more grains are visible when is tested in compression, figure 5.25b.
Thus, under tension, the texture evolution previously observed (figure 5.15a) is attributed mainly to the activation of basal <a> and prismatic <a> slip (figure 5.31a), with a rather low activation of extension twinning (figure 5.12a). On the contrary, in compression, the basal texture (figure 5.15b) developed during the deformation is attributed to the high activation of extension twinning (figure 5.12b) combined with basal slip (figure 5.25b). With a comparable texture to the Z1 alloy, AZ31 alloy during tension [145] slip traces on grains were also observed, which were associated with basal <a>, prismatic <a> as well as pyramidal <a> slip. As opposed to that research, in the present work, in addition to the previously mentioned slip traces, a low number of grains showing slip lines associated to pyramidal I <c+a> and pyramidal II <c+a> were also present. This discrepancy could be attributed to the fact that the slip trace analysis in the present work was performed at higher deformation strain.

The summary of the slip trace analysis performed during the deformation in tension and in compression of the ZX10 alloy is illustrated in figure 5.26. In tension, there is a high activation of basal <a> followed by prismatic <a> slip, figure 5.26a. Both slip modes play an important role since the start of the deformation. At 0.12 of strain, the activation of pyramidal slip mode family is shown. From these pyramidal modes, the most activated correspond to the pyramidal <a>. In reference to the pyramidal I <c+a> and pyramidal II <c+a> its activation is quite comparable, figure 5.26a.
In compression, the deformation is dominated principally by basal <a> slip, figure 5.26b. In this case, a low activation of prismatic <a> slip is remarkable. Grains showing slip lines of pyramidal <a>, pyramidal I <c+a> and pyramidal II <c+a> were observed at 0.12 of deformation. From these deformation modes, the high activation corresponds to the pyramidal <a>. Therefore, from the previously observed, the crystallographic texture evolution in tension (figure 5.16a) is mainly attributed to the activation of basal <a> and prismatic <a> slip (figure 5.26a) as well as the extension twin activation since 0.03 of strain (figure 5.13a).
On the other hand, the texture in compression (figure 5.16b) is developed due to the dominance of basal <a> slip (figure 5.26b) with a pronounced activation of extension twinning (figure 5.13b). Basal <a>, prismatic <a>, pyramidal <a> and pyramidal II <c+a> slip traces reported in this work were also observed for a binary Mg-Ca alloy tested in tension [145]. In contrast, some slip lines associated to pyramidal I <c+a> were detected in the present research work (figure. 5.26a), but not in [145]. These results show the importance of Ca addition to the magnesium alloys to promote the activity of non-basal modes, especially, those ones belonging to the pyramidal mode family which are harder to be activated at room temperature.

The results on the estimation of slip traces in the ZNd10 alloy are shown in figure 5.27. Like in the previous alloys, the basal <a> and prismatic <a> slips take relevance in the early stage of deformation. As the deformation proceeds in tension, the activity of prismatic <a> slip increases, see figure 5.27a. At 0.12 of strain, the activation of pyramidal <a> is higher in comparison with pyramidal I and II <c+a>. On the other hand, in compression, basal <a> and prismatic <a> slips play an important role from the beginning of deformation, see figure 5.27b. The activation of the pyramidal slip family is observed at the deformation of 0.12. Again, the pyramidal <a> has a higher activity if compared to the pyramidal I and II <c+a>, figure 5.27b.

Thus, the deformation in tension was dominated by basal <a> and prismatic <a> slip (figure 5.27a) with a pronounced activation of extension twins (figure 5.14a) that can be consider the responsible in the texture evolution in tension (figure 5.17a).

However, in compression the activity of basal <a> slip dominates the deformation (figure 5.27b), in combination with a profuse activation of extension twin (figure 5.14b) which contribute to the texture development (figure 5.17b).

It is known that the addition of rare earth elements to Mg and its alloys increases the activity of non-basal slip. At a deformation of 4% in tension of a Mg-Nd alloy [145], basal <a> and prismatic <a> slip traces were detected; this in in agreement with the findings in the present work, at least until 0.03 of strain (figure 5.27a). With the further increase of strain, grains with slip traces associated with the pyramidal <a>, pyramidal I <c+a> and pyramidal II <c+a> modes were also detected.

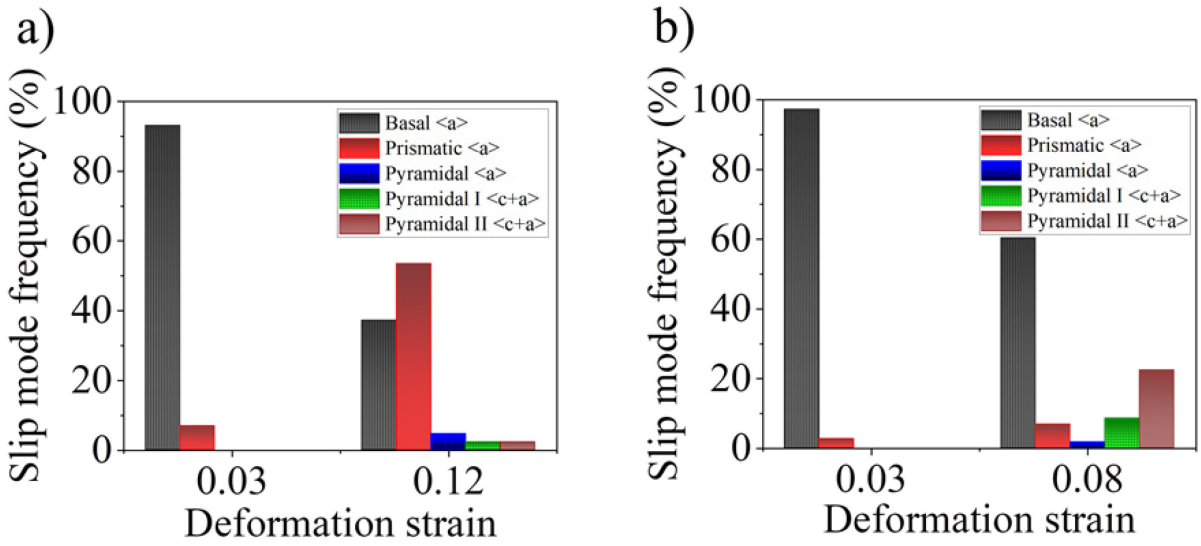

Figure 5.25. Statistics of the identified slip activity at different strains for the Z1 alloy tested in a) tension and b) compression.

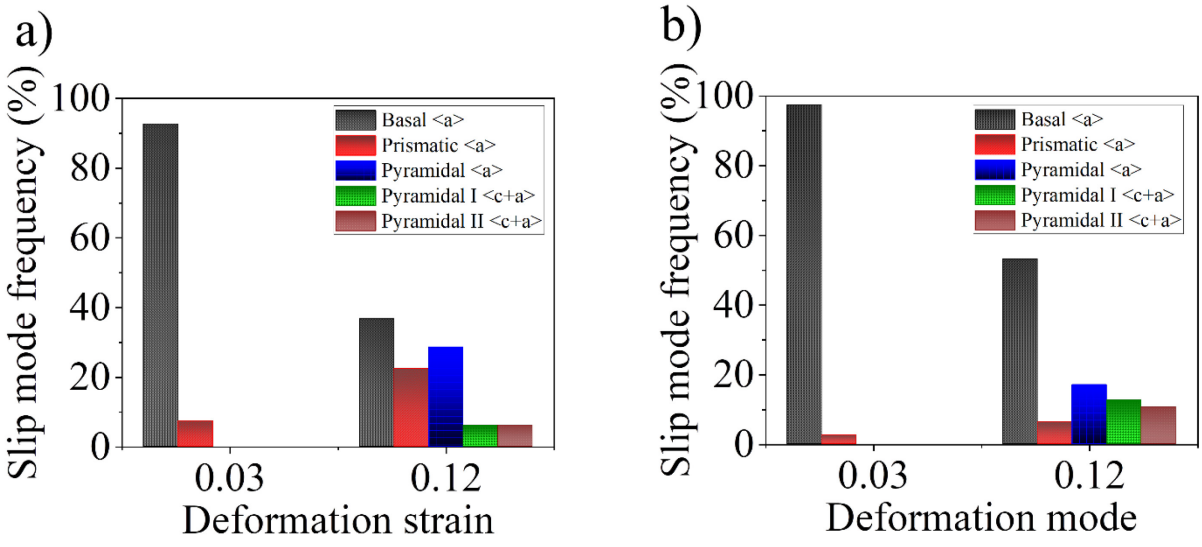

Figure 5.26. Statistics of the identified slip activity at different strains for the ZX10 alloy tested in a) tension and b) compression.

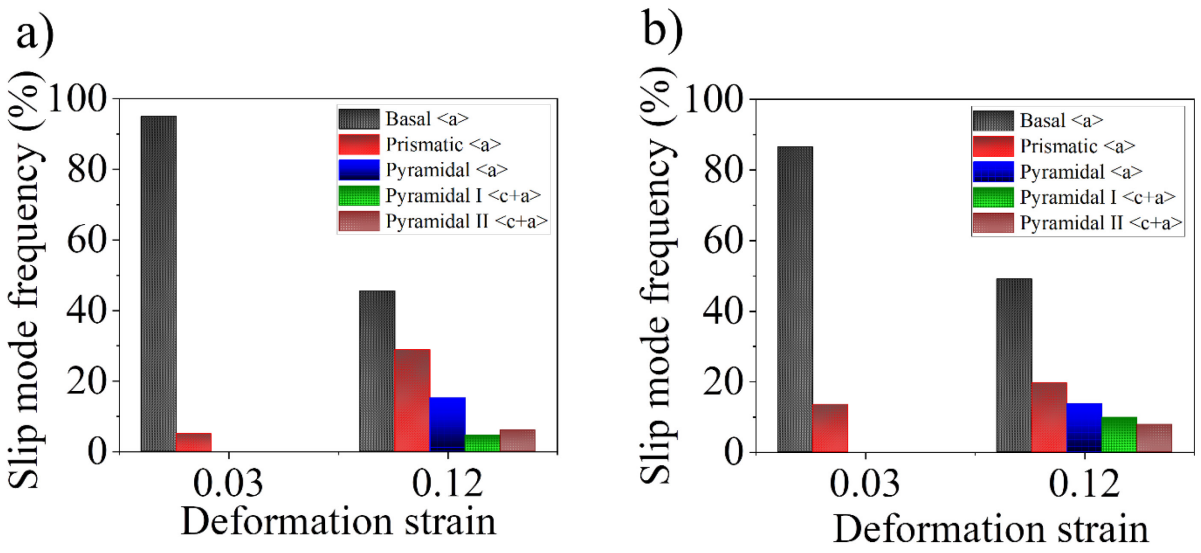

Figure 5.27. Statistics of the identified slip activity at different strains for the ZNd10 alloy tested in a) tension and b) compression.

Table 5.8. Identified slip activities in each alloy tested in tension.

Alloy	Strain	Slip traces									
		Basal <a>		Prismatic <a>		Pyramidal <a>		Pyramidal I <c+a>		Pyramidal II <c+a>	
		Number	Fraction	Number	Fraction	Number	Fraction	Number	Fraction	Number	Fraction
Z1	0.03	27	93.10 %	2	6.90 %	0	0.00	0	0.00	0	0.00
	0.12	16	37.21 %	23	53.48 %	2	4.65 %	1	2.33 %	1	2.33 %
ZX10	0.03	38	92.68 %	3	7.32 %	0	0.00	0	0.00	0	0.00
	0.12	18	36.70 %	11	22.46 %	14	28.60 %	3	6.12 %	3	6.12 %
ZNd10	0.03	38	95.00 %	2	5.00 %	0	0.00 %	0	0.00	0	0.00
	0.12	30	45.45 %	19	28.80 %	10	15.15 %	3	4.54 %	4	6.06 %

Table 5.9. Identified slip activities in each alloy tested in compression.

Alloy	Strain	Slip traces									
		Basal <a>		Prismatic <a>		Pyramidal <a>		Pyramidal I <c+a>		Pyramidal II <c+a>	
		Number	Fraction	Number	Fraction	Number	Fraction	Number	Fraction	Number	Fraction
Z1	0.03	36	97.30 %	1	2.70 %	0	0.00	0	0.00	0	0.00
	0.08	35	60.36 %	4	6.89 %	1	1.72 %	5	8.62 %	13	22.41%
ZX10	0.03	37	97.37 %	1	2.63 %	0	0.00	0	0.00	0	0.00
	0.12	25	53.19 %	3	6.38 %	8	17.03%	6	12.76 %	5	10.64%
ZNd10	0.03	32	86.49 %	5	13.51 %	0	0.00	0	0.00	0	0.00
	0.12	25	49.03 %	10	19.60 %	7	13.73 %	5	9.80 %	4	7.84 %

6. Conclusions and summary

Conclusions

Throughout this work a systematic study of the effect of alloying elements, extrusion parameters, microstructure and crystallographic texture development, mechanical properties as well as the deformation behavior of Mg-Zn based alloys was performed. The applied different extrusion parameters gave several microstructures that allowed the investigation of the grain size and crystallographic texture as well as its effects on the mechanical properties and the plastic deformation of the alloys. The effect of single additions of Ca and Nd on the activation of deformation mechanisms was experimentally studied and these results were compared with simulation results, which involved the application of the crystal plasticity model, i.e., the VPSC model. In a deeper analysis, ex-situ tests to observe and determine the activation of the different deformation modes were accomplished to corroborate the simulation results.

In the following, the conclusions are stated.

Z1 alloy

- The Z1 alloy shows a characteristic extrusion behavior with low extrusion pressures. These reached pressures are even lower with increasing the extrusion temperature.

- In this binary alloy, the recrystallization process is not greatly affected at any applied extrusion condition tested. The most altered feature is the average grain size, which increases at each increment of extrusion temperature or extrusion speed.

- The different extrusion parameters applied to the Z1 alloy, give rise to the formation of basal textures, where the basal planes of the HCP structure are parallel to the extrusion direction. That means there is a conventional development of the classical $< 11\bar{2}0 >$ - $< 10\bar{1}0 >$ texture independent of modification of extrusion speed or extrusion temperature.

- The DRX process, which takes place during the extrusion process of the Z1 alloy allowed the observation that the dynamically recrystallized grains tend to orient to the $< 11\bar{2}0 >$ pole. This texture component is strengthened as grain growth takes place. Due to the high fraction of dynamically recrystallized grains founded in the alloy at any extrusion condition, not changes in the texture were observed after SRX process.

- The mechanical properties are influenced by the initial texture and grain size. The basal texture like the one that is observed in this alloy Z1 results in the well-known yield asymmetry. This is attributed to a higher activation of twinning in compression.

- The VPSC model successfully predicted the flow curves as well as the texture evolution, either in tension or in compression. The crystal plasticity simulations using the VPSC model suggest that the prismatic <a> and basal <a> slip dominate the deformation in tension. On the other hand, the basal <a> slip and extension twinning dominate the deformation in compression.

- The slip trace analysis at room temperature confirms the activation of basal <a> and prismatic <a> slip during the deformation in tension. Scarce activation of pyramidal <a>, pyramidal I <c+a> and pyramidal II <c+a> are observed at large strains. In

contrast, slip traces of basal <a> slip is highly observed in compression. Among the pyramidal slip systems, the pyramidal <a> is the most active but also at large deformation.

ZX10 alloy

- The pressure reached during extrusion processing of ZX10 alloy is higher than that observed in the Z1 alloy owing to a higher alloy content, i.e., the addition of Ca to the Mg-Zn base alloy. Some micro cracks are visible perpendicular to the extrusion direction. However, such micro cracks do not affect severely the surface quality.

- In this ZX10 alloy, the different processing conditions give rise to a distinct microstructure and crystallographic texture. The DRX process is affected due to the addition of Ca into the binary system. The grain growth is delayed when Ca is added. This is manifested with a smaller average grain size if compare with the average grain size revealed in the Z1 alloy.

- The crystallographic texture is modified in such a way that the main component becomes the $< 10\bar{1}1 >$ pole when the alloy is extruded at 250 and 300 °C. With the grain growth, the orientations are spread between the $< 11\bar{2}0 >$ and $< 10\bar{1}0 >$ pole. The formation of a basal crystallographic texture is suggested.

- Post extrusion heat treatments in partly recrystallized microstructures revealed the importance of SRX process. The strong prismatic texture of the partly recrystallized microstructure is weakened with the applied heat treatment, but in essence, the grains maintain their orientation in the surroundings of the $< 10\bar{1}0 >$ as well as along the arc between the $< 11\bar{2}0 >$ and $< 10\bar{1}0 >$ pole.

- The crystallographic textures dominated by the $< 10\bar{1}1 >$ pole observed during the processing of ZX10 alloy resulted in the reduction of the tension-compression yield asymmetry. However, in those samples where the $< 11\bar{2}0 >$-$< 10\bar{1}0 >$ texture is observed, the yield asymmetry increased. In this Zx10 alloy, the obtained ductility is higher if compared with the results from the Z1 alloy.

- The VPSC simulation results and the slip trace analysis show the dominance of basal and prismatic slip during the deformation in tension. In addition, such results suggest that Ca enhances the activity of the pyramidal <a> slip system. On the other hand, although basal slip and extension twinning dominate the deformation in compression, there is a clear enhancement of the pyramidal slip systems. The slip trace analysis reveals a higher activity of pyramidal <a> slip among the pyramidal modes.

ZNd10 alloy

- A higher pressure reached during the extrusion processing due to a higher alloying content is confirmed, which in this case is owing to the addition of Nd into the Mg-Zn base alloy. On the other hand, there is no clear evidence of cracks on the bars surface of ZNd10 alloy.

- The addition of Nd into the Mg-Zn based alloy system delayed the recrystallization process, as some non-recrystallized grains are present at the extrusion of lowest

extrusion temperature combined with the lowest extrusion speed, i.e 250 °C and 2.0 mm/s. Some traces of un-recrystallized grains are also perceptible when is extruded at 300 °C and 2.0 mm/s.

- The presence of Nd into the Mg-Zn base alloy also delays the grain growth. The grain growth retardation during the DRX is more pronounced if compared with the addition of Ca. High extrusion speeds or temperatures are needed to attain completely recrystallized microstructures in this ZNd10 alloy. The resulted average grain size is the smallest in this Nd containing alloy. Therefore, from the two alloying elements, Nd is more effective in the grain refining compared with Ca.

- The strong prismatic $< 10\bar{1}0 >$ texture component results at the lowest extrusion speed combined with the lowest extrusion temperature. This texture component is associated with the presence of non-recrystallized grains in the microstructure. With the fully recrystallized microstructure, the texture intensity reduces and the non-basal component, $< 11\bar{2}1 >$ pole dominates the texture in this ZNd10 alloy.

- Regarding to annealing heat treatments to trigger SRX in partially recrystallized samples, the results showed that the texture intensity reduces and the development of the $< 11\bar{2}1 >$ component was inhibited. The orientation of the grains is mainly distributed in between the $< 11\bar{2}0 >$ and $< 10\bar{1}0 >$ poles.

- The ductility increases as well as the reduction of the yield asymmetry observed during the characterization of the mechanical properties is associated with the increase of recrystallized fraction of the microstructure and the non-basal texture.

- According to the plasticity simulations with the VPSC model, basal <a> and prismatic <a> slip dominate the deformation in tension. The activity of pyramidal <a> slip was also suggested with the implementation of the VPSC model. In this ZNd10 alloy, the activation of pyramidal <a> is slightly higher than its activation in the Ca containing alloy. On the other hand, in compression, the VPSC simulation suggests that basal <a> slip dominate the deformation with a high activation of extension twin and prismatic <a> slip. Additionally, until 0.12 strain, the activity of the three pyramidal slip is quite comparable.

- The slip trace analysis in tension confirms the dominance of basal <a> and prismatic <a> slip as well as the high activation of pyramidal <a> slip among all the pyramidal slips. During the deformation under compression, basal <a> and prismatic <a> slip are also confirmed. In addition, the activation of pyramidal <a>, pyramidal I <c+a> and pyramidal II <c+a> slip is quite similar.

In this dissertation, a systematic study of the effect of Ca or Nd, the extrusion processing parameters on the microstructure, texture, mechanical properties and the deformation behaviour of Mg-Zn based alloys was performed. It was shown that the microstructure and texture evolution of the Mg-Zn alloys are a result of Ca or Nd additions and is also affected by extrusion parameters. The addition of alloying elements modifies the recrystallization kinetics, which is different in each alloy. This work indicates that the preference of grain orientations undoubtedly changes with the extrusion condition and the concomitant grain growth of dynamically recrystallized grains.

This work suggests that during processing, the SRX plays a very important role in the texture modification. Via static recrystallization of partially recrystallized samples, it is possible to achieve grain structures that are very comparable to those obtained by dynamic recrystallization however with a different texture. During the SRX process, the development of the <11–21> component was inhibited in the ZX10 and ZNd10 alloys. Furthermore, both alloys inherit the prismatic character of the deformed microstructure. Due to a change in the balance of deformation mechanisms as well as the increased importance of grain growth of the recrystallized grains, the SRXed texture is very different compared to DRXed texture.
The ZX10 and ZNd10 alloys show significantly reduction of tension-compression yield asymmetry and enhanced room temperature ductility compared to Z1 alloy. Such enhancements are associated to the activation of additional non-basal slip systems due to not only to chemical composition, but also to the initial non-basal crystallographic texture. This dissertation indicates that adding Ca or Nd to the Mg-Zn system, there is a reduction of the ratio between the CRSS of non-basal deformation modes and the CRSS of basal mode. Furthermore, this work shows evidence of the activation of pyramidal <a> mode. Such a deformation mode is not normally reported. However, the pyramidal <a> mode in this work takes relevance in explaining both, the hardening behavior of the materials as well as the texture development.

7. Directions for future work

This thesis covered diverse aspects of the extrusion behavior of magnesium alloys, but still many research opportunities remain that could be explored. A possible study could be the variation in the profile shape, e.g., the extrusion of flat bars, which could have the possibility to study not only its microstructure-texture evolution but also its mechanical properties as for example formability in addition to the common measured tensile properties.

To gain a deeper understanding of the texture effect on the activity of deformation modes, future work can focus on TEM experiments to determine the type of dislocations that are activated. This will be useful to support the slip trace observations made in this study.

In the present work, applying the VPSC model an effort was made to estimate the CRSS of the different slip modes involved in the deformation. Therefore, it would be interesting the experimental and systematic determination of those CRSS. The experimental determination of the CRSS could facilitate the simulation of deformation modes applying the VPSC model, not only considering that the material is deformed at room temperature but also at high temperature. This can be particularly beneficial for the accurate estimation of the CRSS ratios for different deformation modes.

8. References

[1] A.G. Beer, 8 - Enhancing the extrudability of wrought magnesium alloys, in: C. Bettles, M. Barnett (Eds.), Advances in Wrought Magnesium Alloys, Woodhead Publishing2012, pp. 304-322.

[2] J. Bohlen, D. Letzig, K.U. Kainer, New perspectives for wrought magnesium alloys, Materials Science Forum, Trans Tech Publ, 2007, pp. 1-10.

[3] I. Polmear, D. StJohn, J.-F. Nie, M. Qian, 6 - Magnesium Alloys, in: I. Polmear, D. StJohn, J.-F. Nie, M. Qian (Eds.), Light Alloys (Fifth Edition), Butterworth-Heinemann, Boston, 2017, pp. 287-367.

[4] J. Bohlen, S. Yi, D. Letzig, K.U. Kainer, Effect of rare earth elements on the microstructure and texture development in magnesium–manganese alloys during extrusion, Materials Science and Engineering: A 527(26) (2010) 7092-7098.

[5] M.K. Kulekci, Magnesium and its alloys applications in automotive industry, The International Journal of Advanced Manufacturing Technology 39(9) (2008) 851-865.

[6] W.D. Callister, D.G. Rethwisch, Materials Science and Engineering: An Introduction, 8th Edition, Wiley2009.

[7] K.H. Matucha, Materials Science and Technology, Volume 8, Structure and Properties of Nonferrous Alloys, Masters Thesis 8 (1996) 837.

[8] H.E. Friedrich, B.L. Mordike, Technology of magnesium and magnesium alloys, Magnesium Technology: Metallurgy, Design Data, Applications (2006) 219-430.

[9] T.B. Abbott, Magnesium: Industrial and Research Developments Over the Last 15 Years, CORROSION 71(2) (2015) 120-127.

[10] K. Gusieva, C.H.J. Davies, J.R. Scully, N. Birbilis, Corrosion of magnesium alloys: the role of alloying, International Materials Reviews 60(3) (2015) 169-194.

[11] M. Bauser, G. Sauer, K. Siegert, Extrusion, ASM International, Materials Park, OH, 2006.

[12] Z. Zhuoran, N. Stanford, C. Davies, J.F. Nie, N. Birbilis, Magnesium extrusion alloys: a review of developments and prospects, International Materials Reviews (2018) 1-36.

[13] T. Nakata, T. Mezaki, R. Ajima, C. Xu, K. Oh-ishi, K. Shimizu, S. Hanaki, T.T. Sasaki, K. Hono, S. Kamado, High-speed extrusion of heat-treatable Mg–Al–Ca–Mn dilute alloy, Scripta Materialia 101 (2015) 28-31.

[14] S.W. Xu, K. Oh-ishi, S. Kamado, F. Uchida, T. Homma, K. Hono, High-strength extruded Mg–Al–Ca–Mn alloy, Scripta Materialia 65(3) (2011) 269-272.

[15] T. Homma, N. Kunito, S. Kamado, Fabrication of extraordinary high-strength magnesium alloy by hot extrusion, Scripta Materialia 61(6) (2009) 644-647.

[16] B. Zhang, Y. Wang, L. Geng, C. Lu, Effects of calcium on texture and mechanical properties of hot-extruded Mg–Zn–Ca alloys, Materials Science and Engineering: A 539 (2012) 56-60.

[17] A.A. Nayeb-Hashemi, J.B. Clark, A.S.M. International, Phase diagrams of binary magnesium alloys, ASM International, Metals Park, Ohio, 1988.

[18] A.S. Handbook, Magnesium and magnesium alloys, ASM international (1999) 106-118.

[19] D. Wu, R.S. Chen, W. Ke, Microstructure and mechanical properties of a sand-cast Mg–Nd–Zn alloy, Materials & Design 58 (2014) 324-331.

[20] J. Yang, J. Wang, L. Wang, Y. Wu, L. Wang, H. Zhang, Microstructure and mechanical properties of Mg–4.5Zn–xNd (x=0, 1 and 2, wt%) alloys, Materials Science and Engineering: A 479(1) (2008) 339-344.

[21] E.F. Emley, Principles of magnesium technology, Pergamon Press, Oxford; New York, 1966.

[22] A.K.D. Y.C. Lee, D.H. St.John, Grain refinement of magnesium in Magnesium Technology 2000, 211-218.

[23] A.H.B. C.H. Cáceres, The Strength of Concentrated Mg-Zn Solid Solutions, Physica Status Solidi Applied Research 194(1) (2002) 147-158.

[24] G. Mann, J.R. Griffiths, C.H. Cáceres, Hall-Petch parameters in tension and compression in cast Mg–2Zn alloys, Journal of Alloys and Compounds 378(1) (2004) 188-191.

[25] D. Persaud-Sharma, A. McGoron, Biodegradable magnesium alloys: a review of material development and applications, Journal of Biomimetics, Biomaterials and Tissue Engineering, Trans Tech Publ, 2011, pp. 25-39.

[26] Y. Chen, Z. Xu, C. Smith, J. Sankar, Recent advances on the development of magnesium alloys for biodegradable implants, Acta Biomaterialia 10(11) (2014) 4561-4573.

[27] M. Mezbahul-Islam, A. Mostafa, M. Medraj, Essential magnesium alloys binary phase diagrams and their thermochemical data, Journal of Materials 2014 (2014).

[28] J.D. Robson, D.T. Henry, B. Davis, Particle effects on recrystallization in magnesium–manganese alloys: Particle-stimulated nucleation, Acta Materialia 57(9) (2009) 2739-2747.

[29] S. Ganeshan, S.L. Shang, Y. Wang, Z.K. Liu, Effect of alloying elements on the elastic properties of Mg from first-principles calculations, Acta Materialia 57(13) (2009) 3876-3884.

[30] J. Zhang, Y. Dou, G. Liu, Z. Guo, First-principles study of stacking fault energies in Mg-based binary alloys, Computational Materials Science 79 (2013) 564-569.

[31] L.B. Tong, M.Y. Zheng, L.R. Cheng, D.P. Zhang, S. Kamado, J. Meng, H.J. Zhang, Influence of deformation rate on microstructure, texture and mechanical properties of indirect-extruded Mg–Zn–Ca alloy, Materials Characterization 104 (2015) 66-72.

[32] M. Nienaber, K.U. Kainer, D. Letzig, J. Bohlen, Processing Effects on the Formability of Extruded Flat Products of Magnesium Alloys, Frontiers in Materials 6(253) (2019).

[33] J.P. Hadorn, K. Hantzsche, S. Yi, J. Bohlen, D. Letzig, J.A. Wollmershauser, S.R. Agnew, Role of Solute in the Texture Modification During Hot Deformation of Mg-Rare Earth Alloys, Metallurgical and Materials Transactions A 43(4) (2012) 1347-1362.

[34] J.P. Hadorn, K. Hantzsche, S. Yi, J. Bohlen, D. Letzig, S.R. Agnew, Effects of Solute and Second-Phase Particles on the Texture of Nd-Containing Mg Alloys, Metallurgical and Materials Transactions A 43(4) (2012) 1363-1375.

[35] L.L. Rokhlin, Magnesium alloys containing rare earth metals: structure and properties, Crc Press2003.

[36] L. Ma, R.K. Mishra, L. Peng, A.A. Luo, W. Ding, A.K. Sachdev, Texture and mechanical behavior evolution of age-hardenable Mg–Nd–Zn extrusions during aging treatment, Materials Science and Engineering: A 529 (2011) 151-155.

[37] P. Hidalgo-Manrique, S.B. Yi, J. Bohlen, D. Letzig, M.T. Pérez-Prado, Effect of Nd Additions on Extrusion Texture Development and on Slip Activity in a Mg-Mn Alloy, Metallurgical and Materials Transactions A 44(10) (2013) 4819-4829.

[38] B. Lv, J. Peng, Y. Peng, A. Tang, The effect of addition of Nd and Ce on the microstructure and mechanical properties of ZM21 Mg alloy, Journal of Magnesium and Alloys 1(1) (2013) 94-100.

[39] A. Imandoust, C.D. Barrett, T. Al-Samman, K.A. Inal, H. El Kadiri, A review on the effect of rare-earth elements on texture evolution during processing of magnesium alloys, Journal of Materials Science 52(1) (2017) 1-29.

[40] N. Stanford, M.R. Barnett, The origin of "rare earth" texture development in extruded Mg-based alloys and its effect on tensile ductility, Materials Science and Engineering: A 496(1-2) (2008) 399-408.

[41] N. Stanford, Micro-alloying Mg with Y, Ce, Gd and La for texture modification—A comparative study, Materials Science and Engineering: A 527(10) (2010) 2669-2677.

[42] J.P. Hadorn, R.P. Mulay, K. Hantzsche, S. Yi, J. Bohlen, D. Letzig, S.R. Agnew, Texture Weakening Effects in Ce-Containing Mg Alloys, Metallurgical and Materials Transactions A 44(3) (2013) 1566-1576.

[43] G. Ben-Hamu, D. Eliezer, K.S. Shin, S. Cohen, The relation between microstructure and corrosion behavior of Mg–Y–RE–Zr alloys, Journal of Alloys and Compounds 431(1) (2007) 269-276.

[44] S. Graff, Micromechanical modeling of the deformation of HCP Metals, GKSS-Forschungszentrum Geesthacht, Bibliothek, 2007.

[45] D.R. Askeland, P.P. Fulay, W.J. Wright, The Science and Engineering of Materials, Cengage Learning2010.

[46] G.E. Dieter, D. Bacon, Mechanical metallurgy, McGraw-hill New York1986.

[47] Y.N. Berdovsky, Intermetallics research progress, Nova Publishers2008.

[48] J. Pelleg, Mechanical properties of materials, Springer Science & Business Media2012.

[49] K.U. Kainer, Magnesium: proceedings of the 7th International Conference on Magnesium Alloys and their Applications, John Wiley & Sons2007.

[50] M.H. Yoo, S.R. Agnew, J.R. Morris, K.M. Ho, Non-basal slip systems in HCP metals and alloys: source mechanisms, Materials Science and Engineering: A 319-321 (2001) 87-92.

[51] F. Czerwinski, Magnesium Injection Molding, Springer US2007.

[52] Z. Zheng, D.S. Balint, F.P.E. Dunne, Rate sensitivity in discrete dislocation plasticity in hexagonal close-packed crystals, Acta Materialia 107 (2016) 17-26.

[53] M.R. Barnett, A taylor model based description of the proof stress of magnesium AZ31 during hot working, Metallurgical and Materials Transactions A 34(9) (2003) 1799-1806.

[54] J.W. Christian, S. Mahajan, Deformation twinning, Progress in Materials Science 39(1) (1995) 1-157.

[55] M.H. Yoo, Slip, twinning, and fracture in hexagonal close-packed metals, Metallurgical Transactions A 12(3) (1981) 409-418.

[56] E. Tenckhoff, Deformation mechanisms, texture, and anisotropy in zirconium and zircaloy, ASTM International1988.

[57] M.R. Barnett, Twinning and the ductility of magnesium alloys: Part I: "Tension" twins, Materials Science and Engineering: A 464(1) (2007) 1-7.

[58] R. Abbaschian, R.E. Reed-Hill, Physical metallurgy principles, Cengage Learning2008.

[59] H.A. Padilla, C.D. Smith, J. Lambros, A.J. Beaudoin, I.M. Robertson, Effects of Deformation Twinning on Energy Dissipation in High Rate Deformed Zirconium, Metallurgical and Materials Transactions A 38(12) (2007) 2916-2927.

[60] P.K. Saha, Aluminum extrusion technology, Asm International2000.

[61] J. Swiostek, J. Göken, D. Letzig, K.U. Kainer, Hydrostatic extrusion of commercial magnesium alloys at 100°C and its influence on grain refinement and mechanical properties, Materials Science and Engineering: A 424(1) (2006) 223-229.

[62] D.L. Atwell, M.R. Barnett, Extrusion Limits of Magnesium Alloys, Metallurgical and Materials Transactions A 38(12) (2007) 3032-3041.

[63] W.H. Sillekens, M.H.F.M. Hout, F. Pravdic, Extrusion technology for magnesium: Avenues for improving performance, 2005.

[64] A.A. Luo, C. Zhang, A.K. Sachdev, Effect of eutectic temperature on the extrudability of magnesium–aluminum alloys, Scripta Materialia 66(7) (2012) 491-494.

[65] T. Murai, S.-i. Matsuoka, S. Miyamoto, Y. Oki, S. Nagao, H. Sano, Effects of zinc and manganese contents on extrudability of Mg–Al–Zn alloys, Journal of Japan Institute of Light Metals 53(1) (2003) 27-31.

[66] M.G. Jiang, C. Xu, T. Nakata, H. Yan, R.S. Chen, S. Kamado, High-speed extrusion of dilute Mg-Zn-Ca-Mn alloys and its effect on microstructure, texture and mechanical properties, Materials Science and Engineering: A 678 (2016) 329-338.

[67] F.J. Humphreys, M. Hatherly, Chapter 13 - Hot Deformation and Dynamic Restoration, in: F.J. Humphreys, M. Hatherly (Eds.), Recrystallization and Related Annealing Phenomena (Second Edition), Elsevier, Oxford, 2004, pp. 415-V.

[68] H.J.M. J.J. Jonas, Recovery and Recrystallisation during High Temperature Deformation, CNRS."Mise en forme des metaux et alliages", Villars-sur-Ollon, 1975.

[69] R. Kaibyshev, 5 - Dynamic recrystallization in magnesium alloys, in: C. Bettles, M. Barnett (Eds.), Advances in Wrought Magnesium Alloys, Woodhead Publishing2012, pp. 186-225.

[70] O. Sivakesavam, I.S. Rao, Y.V.R.K. Prasad, Processing map for hot working of as cast magnesium, Materials Science and Technology 9 (1993) 805-810.

[71] S. Ion, F. Humphreys, S. White, Dynamic recrystallisation and the development of microstructure during the high temperature deformation of magnesium, Acta Metallurgica 30(10) (1982) 1909-1919.

[72] O. Sitdikov, R. Kaibyshev, Dynamic Recrystallization in Pure Magnesium, MATERIALS TRANSACTIONS 42(9) (2001) 1928-1937.

[73] A.G. Beer, M.R. Barnett, Microstructural Development during Hot Working of Mg-3Al-1Zn, Metallurgical and Materials Transactions A 38(8) (2007) 1856-1867.

[74] C. Barrett, A. Imandoust, A. Oppedal, K. Inal, M. Tschopp, H. Kadiri, Effect of Grain Boundaries on Texture Formation during Dynamic Recrystallization of Magnesium Alloys, Acta Materialia 128 (2017).

[75] O. Muránsky, D.G. Carr, M.R. Barnett, E.C. Oliver, P. Šittner, Investigation of deformation mechanisms involved in the plasticity of AZ31 Mg alloy: In situ neutron diffraction and EPSC modelling, Materials Science and Engineering: A 496(1) (2008) 14-24.

[76] R. Kaibyshev, O. Sitdikov, On the role of twinning in dynamic recrystallization, The Physics of Metals and Metallography 89 (2000) 384-390.

[77] E.A. Ball, P.B. Prangnell, Tensile-compressive yield asymmetries in high strength wrought magnesium alloys, Scripta Metallurgica et Materialia 31(2) (1994) 111-116.

[78] K.D. Molodov, T. Al-Samman, D.A. Molodov, G. Gottstein, Mechanisms of exceptional ductility of magnesium single crystal during deformation at room temperature: Multiple twinning and dynamic recrystallization, Acta Materialia 76 (2014) 314-330.

[79] X. Li, P. Yang, L.N. Wang, L. Meng, F. Cui, Orientational analysis of static recrystallization at compression twins in a magnesium alloy AZ31, Materials Science and Engineering: A 517(1) (2009) 160-169.

[80] É. Martin, R.K. Mishra, J.J. Jonas, Effect of twinning on recrystallisation textures in deformed magnesium alloy AZ31, Philosophical Magazine 91(27) (2011) 3613-3626.

[81] C. Drouven, I. Basu, T. Al-Samman, S. Korte-Kerzel, Twinning effects in deformed and annealed magnesium–neodymium alloys, Materials Science and Engineering: A 647 (2015) 91-104.

[82] A.D. Murphy, J.E. Allison, The Recrystallization Behavior of Unalloyed Mg and a Mg-Al Alloy, Metallurgical and Materials Transactions A 49(5) (2018) 1492-1508.

[83] C.W. Su, L. Lu, M.O. Lai, Recrystallization and grain growth of deformed magnesium alloy, Philosophical Magazine 88(2) (2008) 181-200.

[84] D. Guan, W.M. Rainforth, L. Ma, B. Wynne, J. Gao, Twin recrystallization mechanisms and exceptional contribution to texture evolution during annealing in a magnesium alloy, Acta Materialia 126 (2017) 132-144.

[85] J. Victoria-Hernández, S. Yi, D. Klaumünzer, D. Letzig, Recrystallization behavior and its relationship with deformation mechanisms of a hot rolled Mg-Zn-Ca-Zr alloy, Materials Science and Engineering: A 761 (2019) 138054.

[86] J. Hirsch, T. Al-Samman, Superior light metals by texture engineering: Optimized aluminum and magnesium alloys for automotive applications, Acta Materialia 61(3) (2013) 818-843.

[87] T. Al-Samman, K.D. Molodov, D.A. Molodov, G. Gottstein, S. Suwas, Softening and dynamic recrystallization in magnesium single crystals during c-axis compression, Acta Materialia 60(2) (2012) 537-545.

[88] O. Engler, V. Randle, Introduction to texture analysis: macrotexture, microtexture, and orientation mapping, CRC press2009.

[89] E.W. Kelley, W.F. Hosford, Part I – January 1968 - Papers - Plane-Strain Compression of Magnesium and Magnesium Alloy Crystals, The American Institute of Mining, Metallurgical, and Petroleum Engineers, 1969.

[90] L. Nascimento Silva Ferri, High cycle fatigue behaviour of extruded magnesium alloys containing neodymium, (2014).

[91] B.D. Cullity, S.R. Stock, Elements of x-ray diffraction, Prentice Hall, Upper Saddle River, NJ, 2001.

[92] U.F. Kocks, C.N. Tomé, H.-R. Wenk, Texture and anisotropy: preferred orientations in polycrystals and their effect on materials properties, Cambridge university press1998.

[93] F. Kaiser, K. Kainer, Magnesium alloys and technology, John Wiley & Sons2003.

[94] J. Bohlen, S. Yi, J. Swiostek, D. Letzig, H. Brokmeier, K. Kainer, Microstructure and texture development during hydrostatic extrusion of magnesium alloy AZ31, Scripta Materialia 53(2) (2005) 259-264.

[95] G. Cano-Castillo, J. Victoria-Hernández, J. Bohlen, D. Letzig, K.U. Kainer, Effect of Ca and Nd on the microstructural development during dynamic and static recrystallization of indirectly extruded Mg–Zn based alloys, Materials Science and Engineering: A 793 (2020) 139527.

[96] M.R. Barnett, Twinning and the ductility of magnesium alloys: Part II. “Contraction” twins, Materials Science and Engineering: A 464(1) (2007) 8-16.

[97] M. Lugo, M. Tschopp, J. Jordon, M. Horstemeyer, Microstructure and damage evolution during tensile loading in a wrought magnesium alloy, Scripta Materialia 64(9) (2011) 912-915.

[98] S.S. Park, W.N. Tang, B.S. You, Microstructure and mechanical properties of an indirect-extruded Mg–8Sn–1Al–1Zn alloy, Materials Letters 64(1) (2010) 31-34.

[99] C. Tomé, R. Lebensohn, VISCO-PLASTIC SELF-CONSISTENT (VPSC).

[100] C. Tome, G.R. Canova, U.F. Kocks, N. Christodoulou, J.J. Jonas, The relation between macroscopic and microscopic strain hardening in F.C.C. polycrystals, Acta Metallurgica 32(10) (1984) 1637-1653.

[101] R. Lebensohn, C. Tome, Modelling twinning in texture development codes, Textures and Microstructures 14 (1991).

[102] F. Bachmann, R. Hielscher, H. Schaeben, Texture analysis with MTEX–free and open source software toolbox, Solid State Phenomena, Trans Tech Publ, 2010, pp. 63-68.

[103] A. Chakkedath, A study of the effects of rare-earth elements on the microstructural evolution and deformation behavior of magnesium alloys at temperatures up to 523K, 2016.

[104] J. Signorelli, S. Freschi, P.A. Turner, R.E. Bolmaro, SELF-CON: A Self Consistent Software Package for Micromechanical Simulations, Materials Science Forum 408-412 (2002) 341-346.

[105] T. Ebeling, C. Hartig, T. Laser, R. Bormann, Material law parameter determination of magnesium alloys, Materials Science and Engineering: A 527(1) (2009) 272-280.

[106] S.B. Yi, C.H.J. Davies, H.G. Brokmeier, R.E. Bolmaro, K.U. Kainer, J. Homeyer, Deformation and texture evolution in AZ31 magnesium alloy during uniaxial loading, Acta Materialia 54(2) (2006) 549-562.

[107] C. Tomé, S.R. Agnew, M.A. Bourke, W. Blumenthal, D.W. Brown, G.C. Kaschner, P. Rangaswamy, The relation between texture, twinning and mechanical properties in hexagonal aggregates, Materials Science Forum, Trans Tech Publ, 2002, pp. 263-268.

[108] S.R. Agnew, M.H. Yoo, C.N. Tomé, Application of texture simulation to understanding mechanical behavior of Mg and solid solution alloys containing Li or Y, Acta Materialia 49(20) (2001) 4277-4289.

[109] C. Davies, M. Barnett, Expanding the extrusion limits of wrought magnesium alloys, JOM 56(5) (2004) 22-24.

[110] C.-j. Li, H.-f. Sun, W.-b. Fang, Effect of Extrusion Temperatures on Microstructures and Mechanical Properties of Mg-3Zn-0.2Ca-0.5Y Alloy, Procedia Engineering 81 (2014) 610-615.

[111] N.G. Ross, M.R. Barnett, A.G. Beer, Effect of alloying and extrusion temperature on the microstructure and mechanical properties of Mg–Zn and Mg–Zn–RE alloys, Materials Science and Engineering: A 619 (2014) 238-246.

[112] M. Shahzad, L. Wagner, Influence of extrusion parameters on microstructure and texture developments, and their effects on mechanical properties of the magnesium alloy AZ80, Materials Science and Engineering: A 506(1) (2009) 141-147.

[113] G. Liu, J. Zhou, J. Duszczyk, Finite Element Simulation of Magnesium Extrusion to Manufacture a Cross-Shaped Profile, Journal of Manufacturing Science and Engineering 129(3) (2007) 607-614.

[114] S. Yi, H.-G. Brokmeier, D. Letzig, Microstructural evolution during the annealing of an extruded AZ31 magnesium alloy, Journal of Alloys and Compounds 506(1) (2010) 364-371.

[115] J. Victoria-Hernandez, S. Yi, J. Bohlen, G. Kurz, D. Letzig, The influence of the recrystallization mechanisms and grain growth on the texture of a hot rolled AZ31 sheet during subsequent isochronal annealing, Journal of Alloys and Compounds 616 (2014) 189-197.

[116] J. Victoria-Hernandez, S. Yi, D. Letzig, D. Hernandez-Silva, J. Bohlen, Microstructure and texture development in hydrostatically extruded Mg–Al–Zn alloys during tensile testing at intermediate temperatures, Acta Materialia 61(6) (2013) 2179-2193.

[117] I. Baker, Recovery, recrystallization and grain growth in ordered alloys, Intermetallics 8(9) (2000) 1183-1196.

[118] A. Imandoust, C.D. Barrett, T. Al-Samman, M.A. Tschopp, E. Essadiqi, N. Hort, H. El Kadiri, Unraveling Recrystallization Mechanisms Governing Texture Development from Rare-Earth Element Additions to Magnesium, Metallurgical and Materials Transactions A 49(5) (2018) 1809-1829.

[119] W. Yuan, S.K. Panigrahi, J.Q. Su, R.S. Mishra, Influence of grain size and texture on Hall–Petch relationship for a magnesium alloy, Scripta Materialia 65(11) (2011) 994-997.

[120] M.R. Barnett, 6 - Forming of magnesium and its alloys, in: M.O. Pekguleryuz, K.U. Kainer, A. Arslan Kaya (Eds.), Fundamentals of Magnesium Alloy Metallurgy, Woodhead Publishing2013, pp. 197-231.

[121] K. Illkova, P. Dobroň, F. Chmelík, K.U. Kainer, J. Balík, S. Yi, D. Letzig, J. Bohlen, Effect of aluminium and calcium on the microstructure, texture, plastic deformation and related acoustic emission of extruded magnesium–manganese alloys, Journal of Alloys and Compounds 617 (2014) 253-264.

[122] H. Yu, Y. Xin, M. Wang, Q. Liu, Hall-Petch relationship in Mg alloys: A review, Journal of Materials Science & Technology 34(2) (2018) 248-256.

[123] Q. Ma, H. El Kadiri, A.L. Oppedal, J.C. Baird, B. Li, M.F. Horstemeyer, S.C. Vogel, Twinning effects in a rod-textured AM30 Magnesium alloy, International Journal of Plasticity 29 (2012) 60-76.

[124] F. Mokdad, D.L. Chen, D.Y. Li, Single and double twin nucleation, growth, and interaction in an extruded magnesium alloy, Materials & Design 119 (2017) 376-396.

[125] I. Ulacia, N.V. Dudamell, F. Gálvez, S. Yi, M.T. Pérez-Prado, I. Hurtado, Mechanical behavior and microstructural evolution of a Mg AZ31 sheet at dynamic strain rates, Acta Materialia 58(8) (2010) 2988-2998.

[126] A.S. Khan, A. Pandey, T. Gnäupel-Herold, R.K. Mishra, Mechanical response and texture evolution of AZ31 alloy at large strains for different strain rates and temperatures, International Journal of Plasticity 27(5) (2011) 688-706.

[127] C. Ha, J. Bohlen, S. Yi, X. Zhou, H.-G. Brokmeier, N. Schell, D. Letzig, K.U. Kainer, Influence of Nd or Ca addition on the dislocation activity and texture changes of Mg–Zn alloy sheets under uniaxial tensile loading, Materials Science and Engineering: A 761 (2019) 138053.

[128] S.A. Habib, A.S. Khan, T. Gnäupel-Herold, J.T. Lloyd, S.E. Schoenfeld, Anisotropy, tension-compression asymmetry and texture evolution of a rare-earth-containing magnesium alloy sheet, ZEK100, at different strain rates and temperatures: Experiments and modeling, International Journal of Plasticity 95 (2017) 163-190.

[129] Zhou, C. Ha, Yi, J. Bohlen, Schell, Chi, X. Zheng, H.-G. Brokmeier, Texture and Lattice Strain Evolution during Tensile Loading of Mg–Zn Alloys Measured by Synchrotron Diffraction, Metals 10 (2020) 124.

[130] C. Ma, A. Chapuis, X. Guo, L. Zhao, P. Wu, Q. Liu, X. Mao, Modeling the deformation behavior of a rolled Mg alloy with the EVPSC-TDT model, Materials Science and Engineering: A 682 (2017) 332-340.

[131] A. Maldar, L. Wang, G. Zhu, X. Zeng, Investigation of the alloying effect on deformation behavior in Mg by Visco-Plastic Self-Consistent modeling, Journal of Magnesium and Alloys 8(1) (2020) 210-218.

[132] M. Lentz, M. Klaus, I.J. Beyerlein, M. Zecevic, W. Reimers, M. Knezevic, In situ X-ray diffraction and crystal plasticity modeling of the deformation behavior of extruded Mg–Li–(Al) alloys: An uncommon tension–compression asymmetry, Acta Materialia 86 (2015) 254-268.

[133] W.B. Hutchinson, M.R. Barnett, Effective values of critical resolved shear stress for slip in polycrystalline magnesium and other hcp metals, Scripta Materialia 63(7) (2010) 737-740.

[134] N. Stanford, M.R. Barnett, Solute strengthening of prismatic slip, basal slip and {10$\bar{1}$2} twinning in Mg and Mg–Zn binary alloys, International Journal of Plasticity 47 (2013) 165-181.

[135] R. Sánchez-Martín, M.T. Pérez-Prado, J. Segurado, J. Bohlen, I. Gutiérrez-Urrutia, J. Llorca, J.M. Molina-Aldareguia, Measuring the critical resolved shear stresses in Mg alloys by instrumented nanoindentation, Acta Materialia 71 (2014) 283-292.

[136] A. Chapuis, Q. Liu, Simulations of texture evolution for HCP metals: Influence of the main slip systems, Computational Materials Science 97 (2015) 121-126.

[137] M. Lentz, M. Klaus, R.S. Coelho, N. Schaefer, F. Schmack, W. Reimers, B. Clausen, Analysis of the Deformation Behavior of Magnesium-Rare Earth Alloys Mg-2 pct Mn-1 pct Rare Earth and Mg-5 pct Y-4 pct Rare Earth by In Situ Energy-Dispersive X-ray Synchrotron Diffraction and Elasto-Plastic Self-Consistent Modeling, Metallurgical and Materials Transactions A 45(12) (2014) 5721-5735.

[138] M. Lentz, M. Klaus, M. Wagner, C. Fahrenson, I.J. Beyerlein, M. Zecevic, W. Reimers, M. Knezevic, Effect of age hardening on the deformation behavior of an Mg–Y–Nd alloy: In-situ X-ray diffraction and crystal plasticity modeling, Materials Science and Engineering: A 628 (2015) 396-409.

[139] A. Chakkedath, J. Bohlen, S. Yi, D. Letzig, Z. Chen, C.J. Boehlert, The Effect of Nd on the Tension and Compression Deformation Behavior of Extruded Mg-1Mn (wt pct) at Temperatures Between 298 K and 523 K (25 °C and 250 °C), Metallurgical and Materials Transactions A 45(8) (2014) 3254-3274.

[140] C.M. Cepeda-Jiménez, J.M. Molina-Aldareguia, M.T. Pérez-Prado, EBSD-Assisted Slip Trace Analysis During In Situ SEM Mechanical Testing: Application to Unravel Grain Size Effects on Plasticity of Pure Mg Polycrystals, JOM 68(1) (2016) 116-126.

[141] C.J. Boehlert, Z. Chen, A. Chakkedath, I. Gutiérrez-Urrutia, J. Llorca, J. Bohlen, S. Yi, D. Letzig, M.T. Pérez-Prado, In situ analysis of the tensile deformation mechanisms in extruded Mg–1Mn–1Nd (wt%), Philosophical Magazine 93(6) (2013) 598-617.

[142] C.J. Boehlert, Z. Chen, I. Gutiérrez-Urrutia, J. Llorca, M.T. Pérez-Prado, In situ analysis of the tensile and tensile-creep deformation mechanisms in rolled AZ31, Acta Materialia 60(4) (2012) 1889-1904.

[143] D.D. Yin, Q.D. Wang, C.J. Boehlert, Z. Chen, H.M. Li, R.K. Mishra, A. Chakkedath, In-Situ Study of the Tensile Deformation and Fracture Modes in Peak-Aged Cast Mg-11Y-5Gd-2Zn-0.5Zr (Weight Percent), Metallurgical and Materials Transactions A 47(12) (2016) 6438-6452.

[144] A. Chakkedath, C.J. Boehlert, In Situ Scanning Electron Microscopy Observations of Contraction Twinning and Double Twinning in Extruded Mg-1Mn (wt.%), JOM 67(8) (2015) 1748-1760.

[145] G. Zhu, L. Wang, H. Zhou, J. Wang, Y. Shen, P. Tu, H. Zhu, W. Liu, P. Jin, X. Zeng, Improving ductility of a Mg alloy via non-basal <a> slip induced by Ca addition, International Journal of Plasticity 120 (2019) 164-179.

Appendix

a) Z1 Alloy

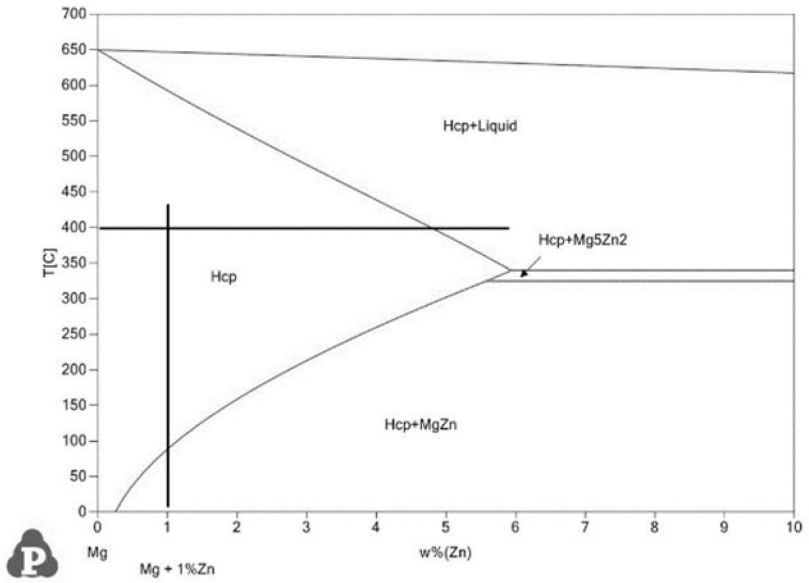

b) ZX10 Alloy

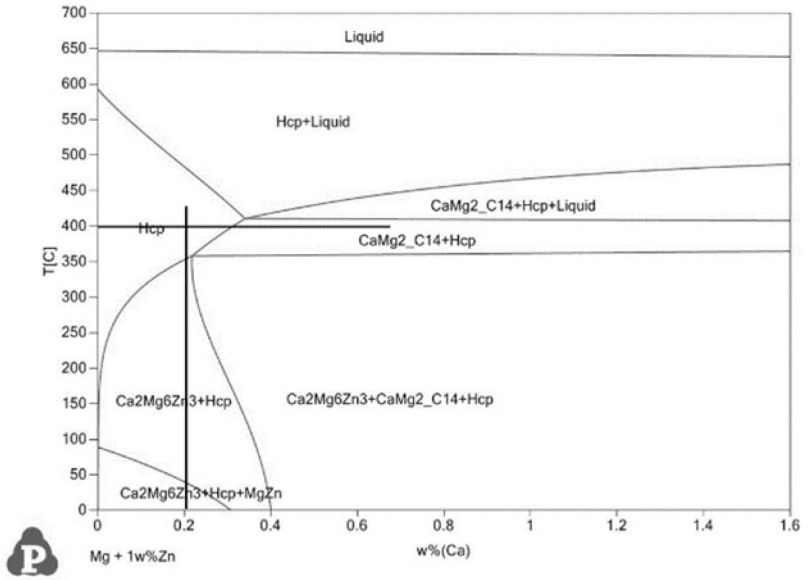

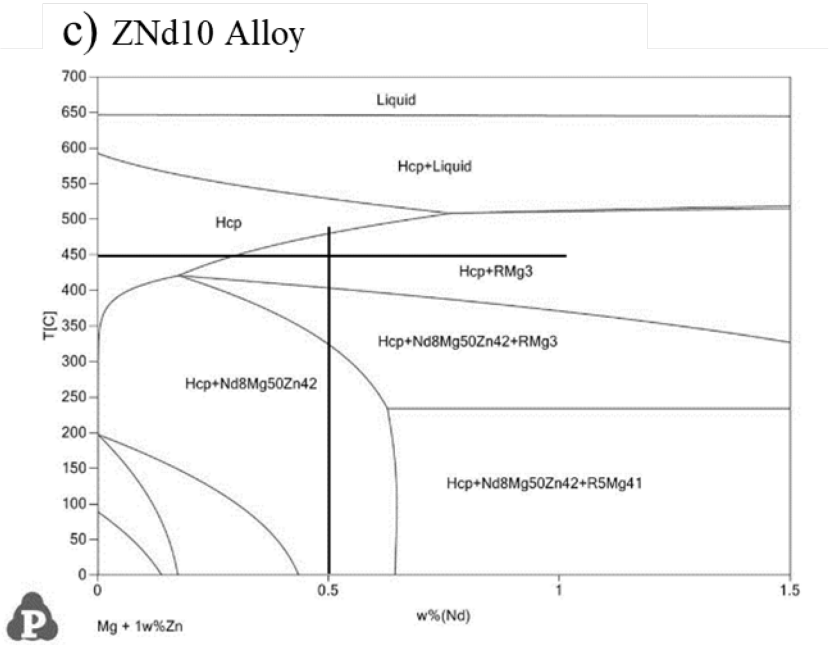

Figure A.1. Phase diagrams showing where the solubilization heat treatments were done; a) Z1 alloy, b) ZX10 alloy and c) ZNd10 alloy.

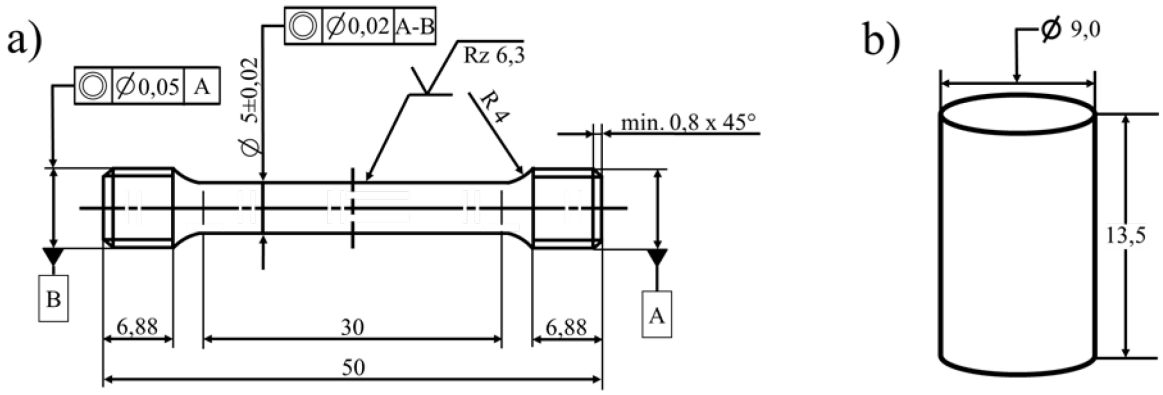

Figure A.2. Schematic representation of the samples for mechanical characterization, a) tension tests from round bars, b) compression tests from round bars.

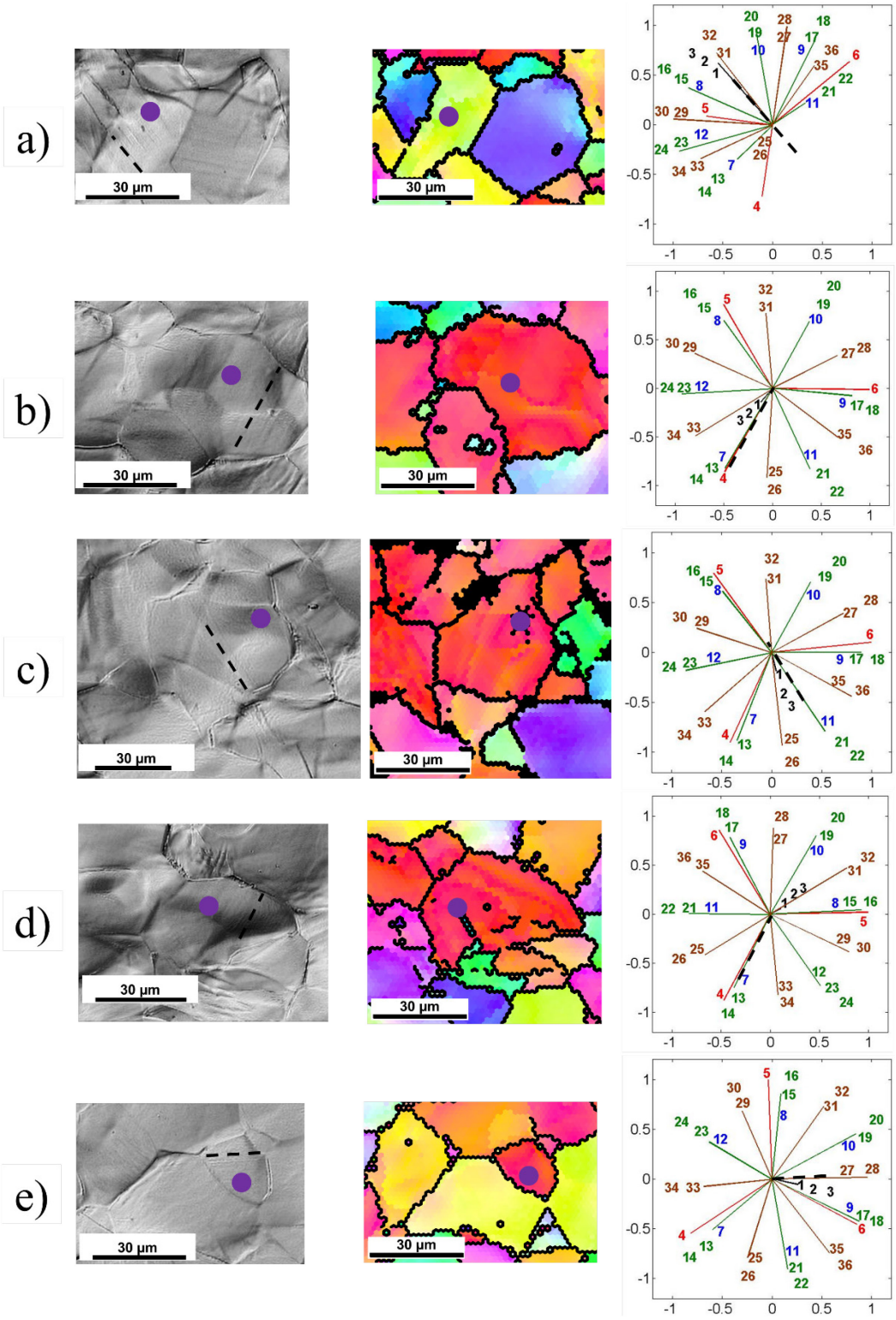

Figure A3. Grains where slip lines are developed: a) basal <a> slip, b) prismatic <a> slip, c) pyramidal <a>, d) pyramidal I <c+a> and e) pyramidal II <c+a>. Alloy Z1 tested in tension. The black dashed line points out the corresponding slip trace. The violet dot indicates the grain showing the slip trace.

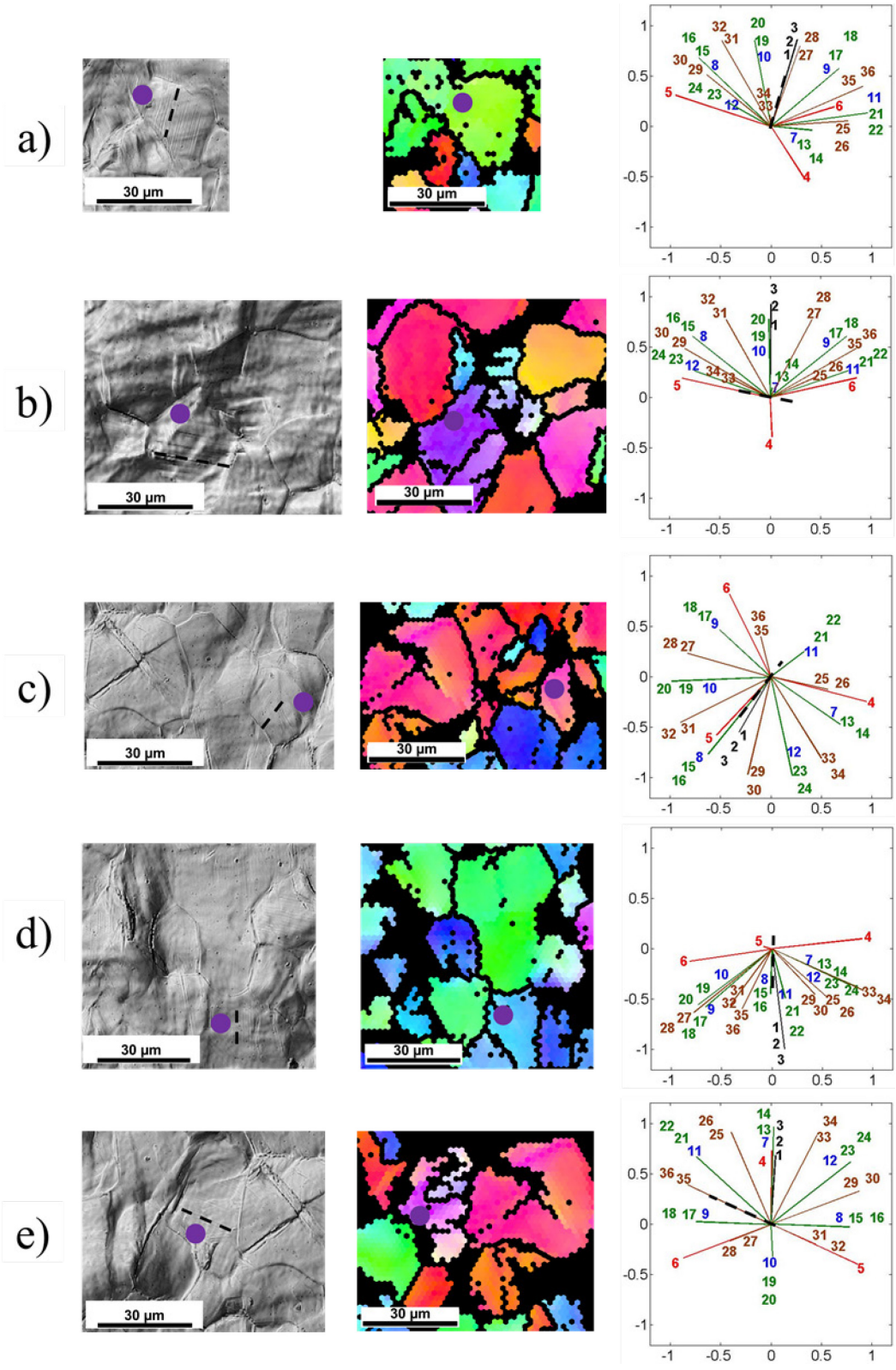

Figure A4. Grains where slip lines are developed: a) basal <a> slip, b) prismatic <a> slip, c) pyramidal <a>, d) pyramidal I <c+a> and e) pyramidal II <c+a>. Alloy Z1 tested in compression. The black dashed line points out the corresponding slip trace. The violet dot indicates the grain showing the slip trace.

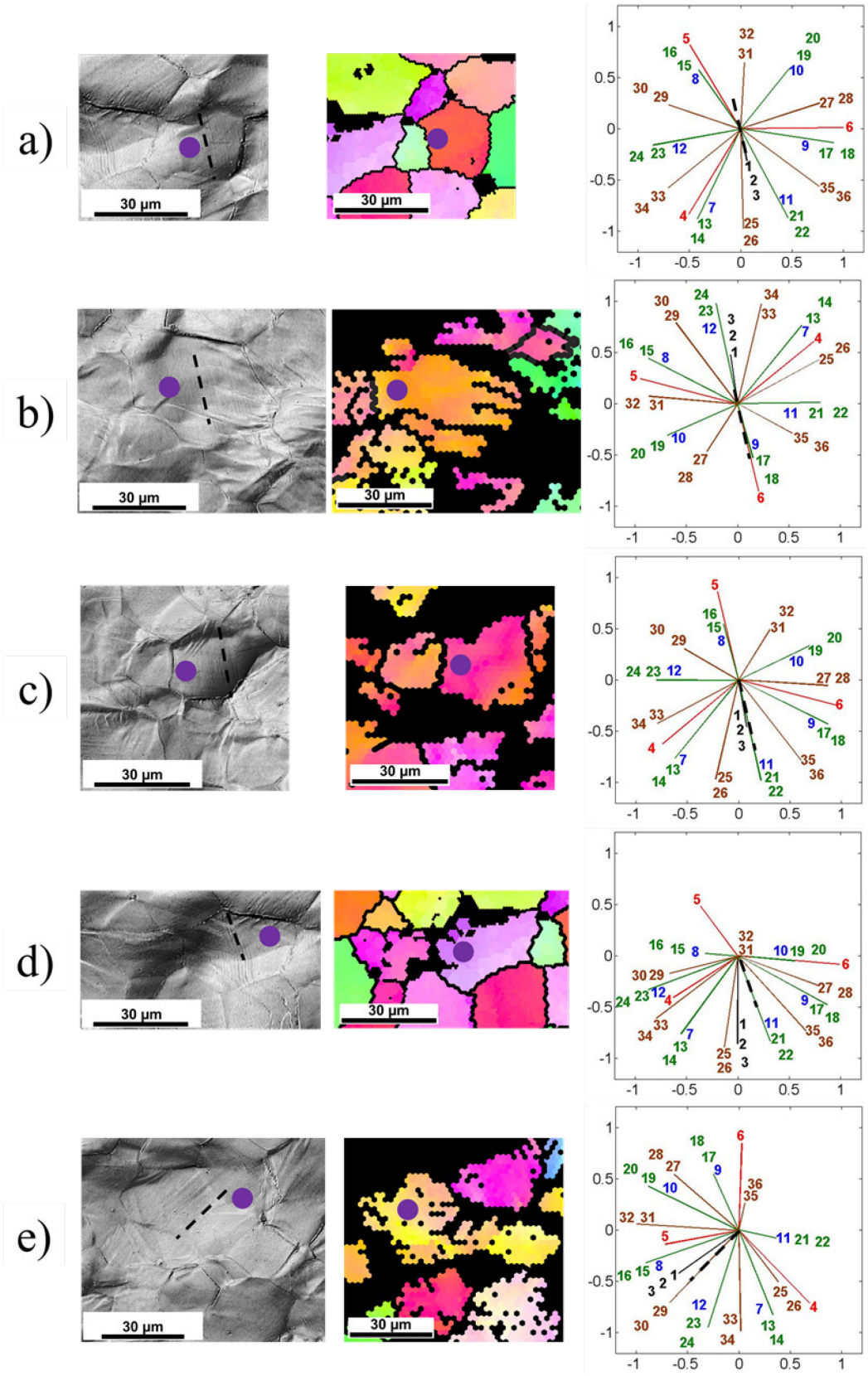

Figure A5. Grains where slip lines are developed: a) basal <a> slip, b) prismatic <a> slip, c) pyramidal <a>, d) pyramidal I <c+a> and e) pyramidal II <c+a>. Alloy ZX10 tested in tension. The black dashed line points out the corresponding slip trace. The violet dot indicates the grain showing the slip trace.

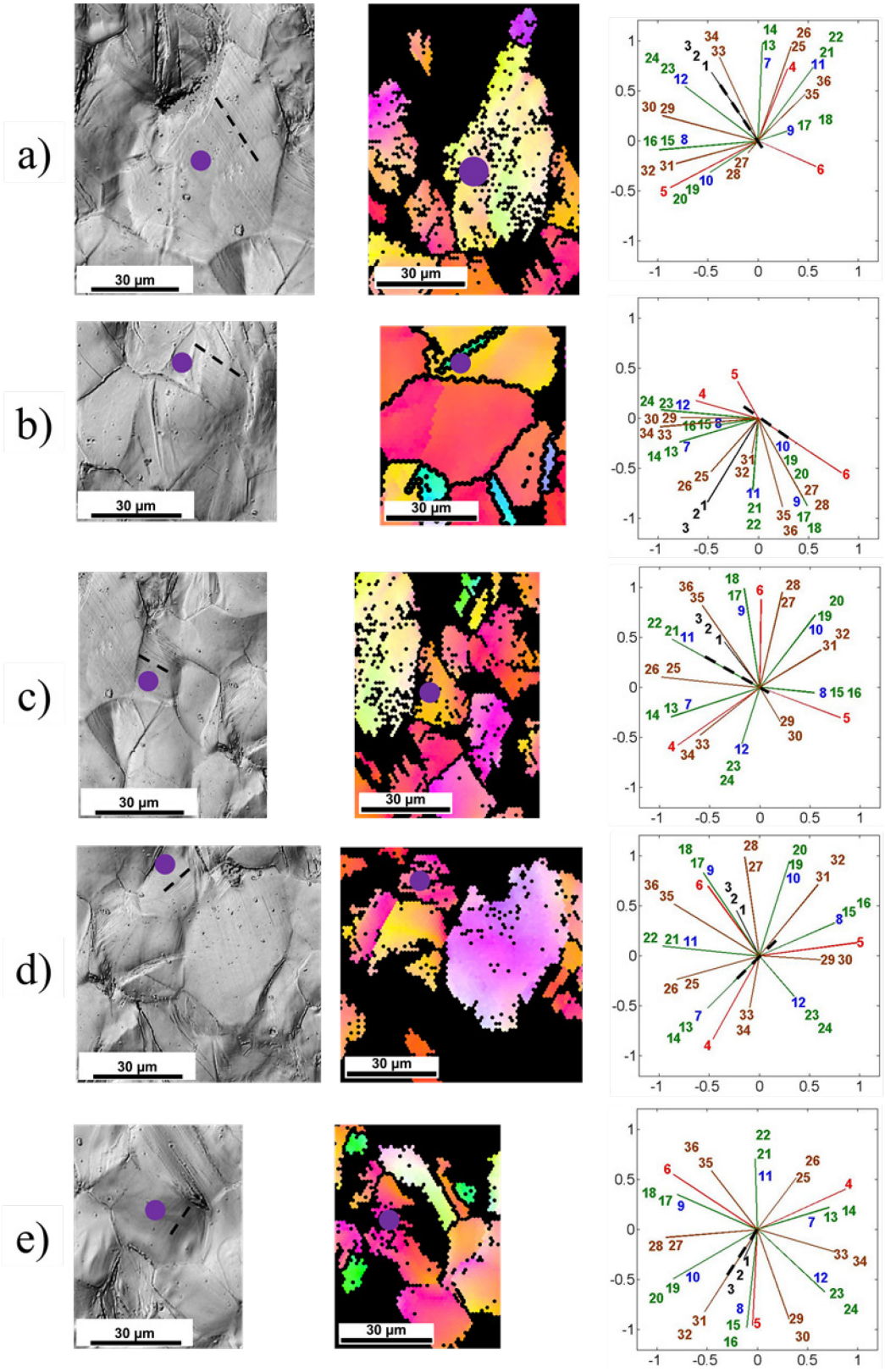

Figure A6. Grains where slip lines are developed: a) basal <a> slip, b) prismatic <a> slip, c) pyramidal <a>, d) pyramidal I <c+a> and e) pyramidal II <c+a>. Alloy ZX10 tested in compression. The black dashed line points out the corresponding slip trace. The violet dot indicates the grain showing the slip trace.

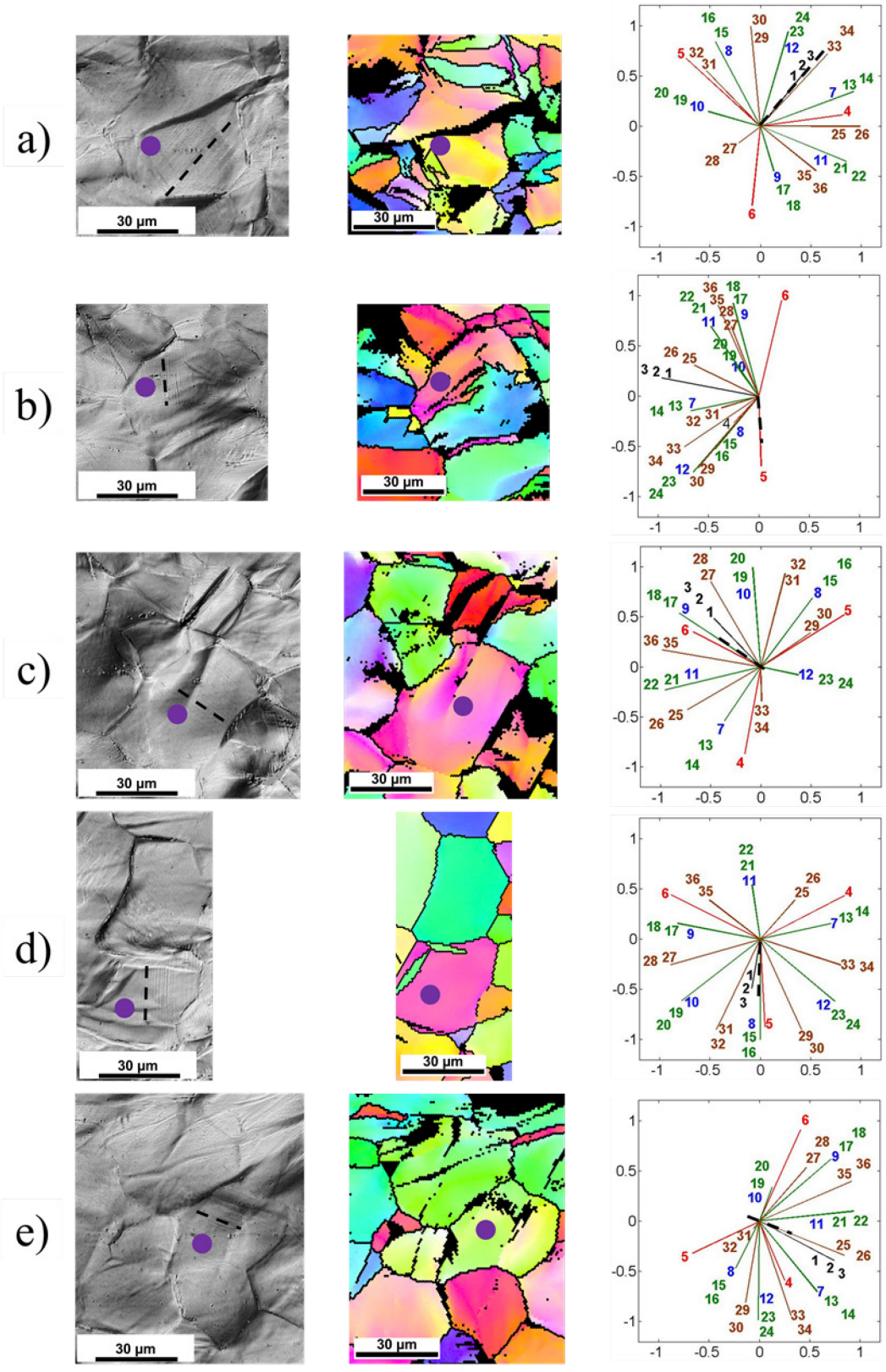

Figure A7. Grains where slip lines are developed: a) basal <a> slip, b) prismatic <a> slip, c) pyramidal <a>, d) pyramidal I <c+a> and e) pyramidal II <c+a>. Alloy ZNd10 tested in tension. The black dashed line points out the corresponding slip trace. The violet dot indicates the grain showing the slip trace.

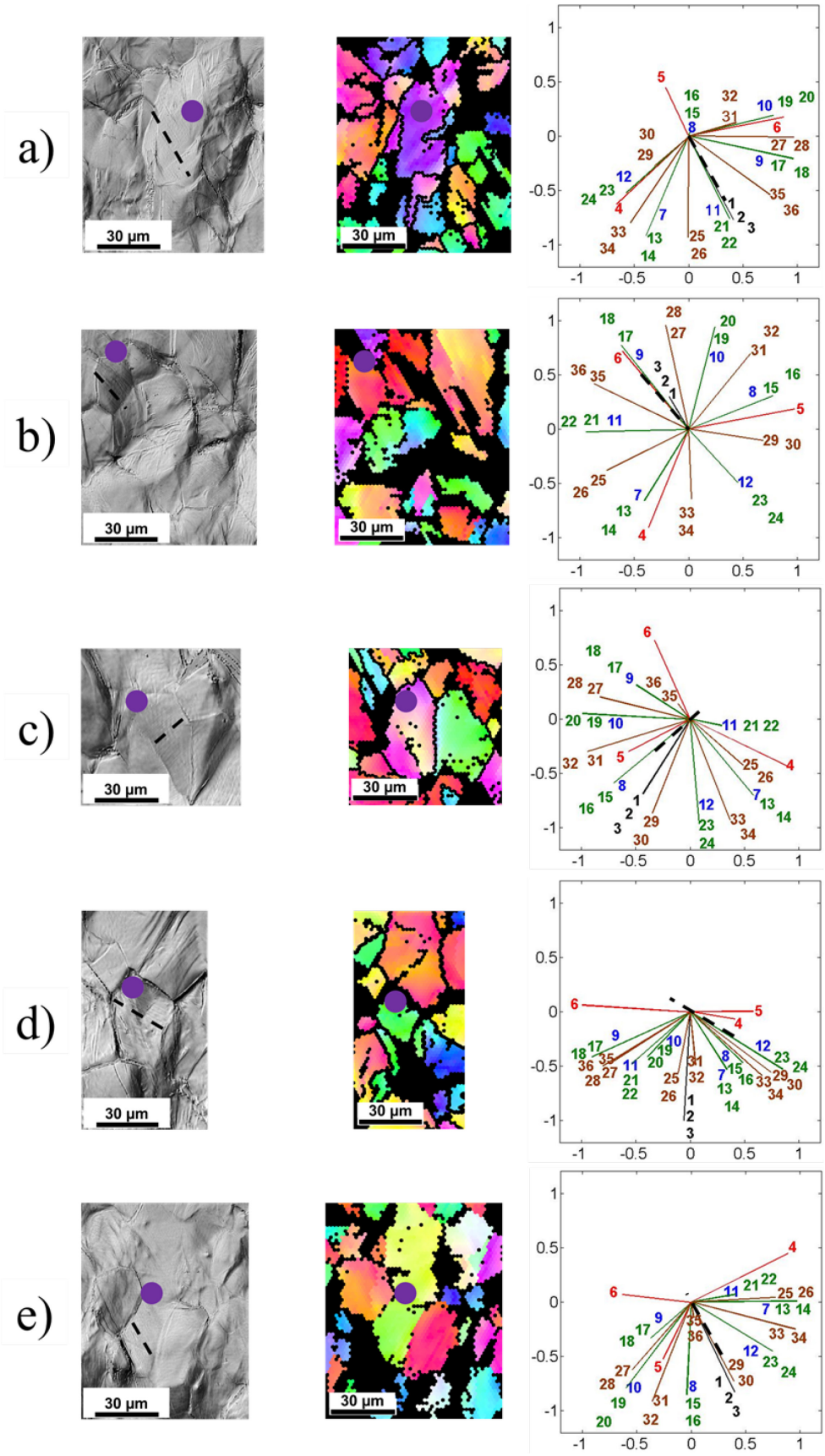

Figure A8. Grains where slip lines are developed: a) basal <a> slip, b) prismatic <a> slip, c) pyramidal <a>, d) pyramidal I <c+a> and e) pyramidal II <c+a>. Alloy ZNd10 tested in compression. The black dashed line points out the corresponding slip trace. The violet dot indicates the grain showing the slip trace.